Atomistic Modelling of Charge Trapping Defects in Silicon Dioxide

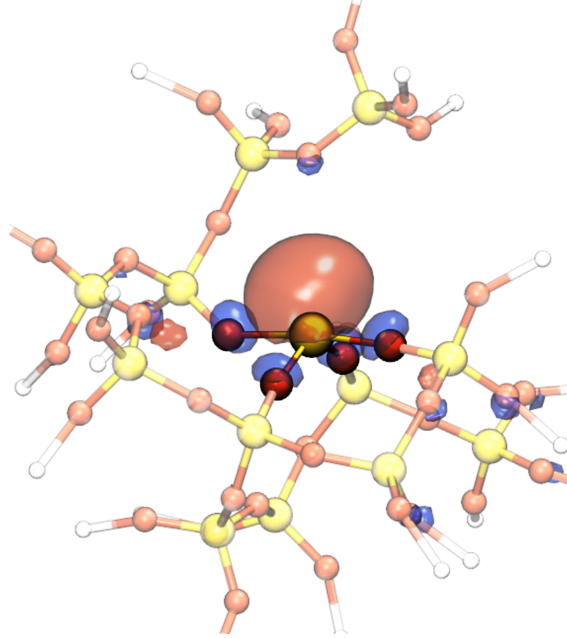

Al-Moatasem Bellah El-Sayed

Department of Physics and Astronomy

University Collge London

2015

A thesis submitted in partial fulfilment of the requirements for the degree of Doctor of Philosophy (Ph.D.) of the University College London

Supervisor: Prof. Alexander L. Shluger

I, Al-Moatasem Bellah El-Sayed, confirm that the work presented in this thesis is my own. Where information has been derived from other sources, I confirm that this has been indicated in the thesis.

Al-Moatasem El-Sayed

June 2015

Abstract

This thesis focuses on the atomistic modelling of electron trapping sites in silicon dioxide (SiO_2) and interactions of hydrogen with the SiO_2 network and the resulting defects they produce. They are discussed in the context of electronic device reliability issues.

The results presented here were calculated in both crystalline (c-) and amorphous (a-) SiO_2. Due to its disordered nature, modelling a-SiO_2 is challenging and required the use of a melt-and-quench technique using a classical interatomic potential. All models were evaluated against experimental data to ensure that they are indeed representative of a-SiO_2.

Using density functional theory (DFT) and the models described above, extra electrons were shown to trap in pure c- and a- SiO_2 in deep band gap states for the first time. They can trap spontaneously on pre-existing structural precursors in a-SiO_2. The optical absorption spectrum of the intrinsic electron traps was calculated using time-dependent DFT and shows a peak at 3.7 eV, which is in good agreement with a previously unidentified experimental absorption peak measured at low temperatures.

Electronic device fabrication processes widely employ hydrogen due to its perceived ability to improve their reliability. The results in this thesis show that both atomic and molecular hydrogen are involved in defect generation processes. Atomic hydrogen was found to interact strongly with strained Si-O bonds to form a stable defect. The barriers to create and annihilate this defect as well as the distribution of its properties were calculated. Hydrogen molecules were found to generate Si-H bonds which can trap holes to form a similar defect and release a proton which can modulate the defect's properties.

These results provide insight into the atomistic nature of defects that can be involved in electronic device reliability issues and help guide the design of reliable fabrication processes.

Contents

1 Introduction **1**

1.1 Background & Motivation 1

1.2 Electronic Device Reliability Issues 3

1.3 Atomistic Nature of Defects Implicated in Reliability Issues 6

1.4 Scope of this Work 8

2 Theoretical Background and Methods **11**

2.1 Introduction 11

2.2 Molecular Dynamics 12

2.3 Density Functional Theory 14

2.3.1 Gaussian Plane Waves Method 18

2.3.2 Hybrid Functionals and the Auxiliary Density Matrix Method 21

2.4 Classical potentials 23

2.4.1 Charge variable potentials 24

2.4.2 Charge-optimized many-body potential (COMB) 26

2.4.3 ReaxFF 28

2.5 Embedded Cluster Method 30

2.6 Nudged Elastic Band Method 33

3 Modelling Amorphous Silicon Dioxide and the Si/SiO_2 interface **37**

3.1 Introduction 37

3.2 Choosing the Classical Potential 39
3.2.1 Small Silicon and Silica Test Clusters 40
3.2.2 NVE Molecular Dynamics using ReaxFF and COMB 44
3.2.3 Summary 47
3.3 Making Amorphous Silica Models 47
3.3.1 Modelling a-SiO_2 using the ReaxFF potential and the Melt-and-Quench Method 48
3.3.2 DFT Optimisation of ReaxFF Structures 53
3.3.3 Summary 58
3.4 Constructing the Si/SiO_2 Interface 58
3.4.1 Melt and Quench *in situ* 59
3.4.2 a-SiO_2 Layer Strained to Silicon Lateral Dimensions 61
3.4.3 Summary 64
3.5 Conclusions 65

4 Defects in Bulk SiO_2 66
4.1 Introduction 66
4.2 Quartz 67
4.2.1 Neutral Oxygen Vacancy 67
4.2.2 Positive Oxygen Vacancy 71
4.2.3 Negative Oxygen Vacancy 78
4.2.4 Summary 79
4.3 Amorphous Silicon Dioxide 80
4.3.1 Neutral Oxygen Vacancy 80
4.3.2 Positive Oxygen Vacancy 82
4.3.3 Singly Negative Oxygen Vacancy 83
4.3.4 Summary 85
4.4 Discussion 85

5 Electron Trapping at Impurities in Silicon Dioxide **88**

5.1 Introduction 88

5.2 Calculation Details 90

5.3 Results of calculations 92

5.3.1 Ge-doped α-quartz 92

5.3.2 Li-doped α-quartz 96

5.4 Discussion and Conclusions 100

6 Intrinsic Electron Trapping Sites in Silicon Dioxide **102**

6.1 Introduction 102

6.2 Calculation Details 104

6.2.1 Classical Calculations 104

6.2.2 Density Functional Theory Calculations 106

6.3 Results of Calculations 107

6.3.1 Electron Trapping in Bulk α-Quartz 107

6.3.2 Electron trapping in amorphous SiO_2 108

6.3.3 Concentration of electron trapping sites in a-SiO_2 112

6.4 Discussion and Conclusions 114

7 Optical Absorption Spectra of Trapped Electrons in SiO_2 **117**

7.1 Introduction 117

7.1.1 Experimental Observations 118

7.2 Calculation Details 122

7.3 Results of Calculations 123

7.3.1 Optical Absorption of the Ge Electron Trapping Centre 123

7.3.2 Optical Absorption of the Electron Trapping Centre 125

7.4 Discussion and Conclusions 127

8 Hydrogen's Interactions with Silicon Dioxide **129**

8.1 Introduction 129

8.2 Calculation Details 132

8.3 Results of calculations 133

8.3.1 Atomic Hydrogen in a-SiO_2 133

8.3.2 Molecular hydrogen in a-SiO_2 141

8.4 Discussion and Conclusions 148

9 Concluding Remarks 151

9.1 Summary 151

9.2 Future Work 153

A BKS Parameterisation for Si and O 155

B Formation Energy Calculation 156

B.1 Charge Correction 157

List of Figures

1.1 A transmission electron micrograph (TEM) image of a silicon MOSFET. 3

1.2 Typical structure of a MOSFET. 4

1.3 Defect assisted tunnelling in electronic devices. 5

1.4 Atomistic structure of the hydrogen bridge. 7

2.1 Silicon-silicon bond-order dependence on interatomic distance. 29

2.2 Schematic of embedded cluster method. 32

3.1 Two interlinked SiO_4 units illustrating the flexible Si-O-Si angle. . . . 38

3.2 Atomic structures of Si_3O_y clusters 40

3.3 Atomic structures of Si_3O_6 optimized using COMB. 42

3.4 Atomic structures of Si_nO_n clusters 42

3.5 Atomic structures of Si_n clusters, where n=2-6. 43

3.6 Plots of total energy from MD simulations using ReaxFF and COMB 46

3.7 Histograms of the short-range geometrical properties of a-SiO_2 from 320 a-SiO_2 models generated using the ReaxFF potential. 49

3.8 Real space representation and spatial frequencies of crystalline and amorphous solids. 51

3.9 Total neutron structure factors from a-SiO_2 models and from neutron scattering experiments. 53

3.10 Histograms of the short-range geometrical properties of 320 DFT optimised models of a-SiO_2 . . . 54
3.11 Histogram of the atomic displacements of the ReaxFF a-SiO_2 models before and after DFT optimisation. . . . 55
3.12 Electronic densities of state from 320 models of a-SiO_2. . . . 56
3.13 Silicon supercell with oxygen atoms inserted to form silica layer. . . . 60
3.14 Si/SiO_2 stack after *in situ* melt and quench of the SiO_2 layer. . . . 61
3.15 Si/SiO_2 interface made with a-SiO_2 layer placed on top of silicon. . . 62
3.16 Geometrical properties of Si/SiO_2 interface made with a-SiO_2 layer placed on top of silicon. . . . 64

4.1 Crystal structure of α-quartz . . . 68
4.2 Atomic and electronic structure of neutral oxygen vacancy in α-quartz 70
4.3 Displacement field of neutral oxygen vacancy in quartz. . . . 71
4.4 The dimer configuration of the positive oxygen vacancy in α-quartz. . 73
4.5 Displacement field of the positive oxygen vacancy. . . . 74
4.6 The puckered configuration of the positively charged oxygen vacancy in α-quartz. . . . 76
4.7 The negatively charged oxygen vacancy in α-quartz. . . . 79
4.8 The neutral oxygen vacancy in a-SiO_2. . . . 81
4.9 One-electron level of the positive oxygen vacancy in a-SiO_2 . . . 83
4.10 One-electron level of the negative oxygen vacancy in a-SiO_2 . . . 84
4.11 Thermodynamics of the oxygen vacancy in α-quartz and a-SiO_2. . . . 86

5.1 Ge impurity in α-quartz . . . 93
5.2 Spin density of the Ge electron trap in α-quartz . . . 94
5.3 Energies of the six different electron trapping configurations in Ge-doped α-quartz. . . . 96
5.4 Interstitial Li atom in α-quartz . . . 97
5.5 $[SiO_4/Li]^0$ centre in α-quartz. . . . 99

6.1 A schematic of one-dimensional diabatic potential energy surfaces . . 106

6.2 Intrinsic electron trap in α-quartz. 109

6.3 Bottom of the a-SiO_2 conduction band. 111

6.4 Spin density of the intrinsic electron trap in a-SiO_2. 114

7.1 Experimental optical absorption spectra of electron-irradiated a-SiO_2. 119

7.2 Growth kinetics of the optical absorption bands of electron irradiated a-SiO_2 120

7.3 Calculated optical absorption spectrum of the GEC in α-quartz. . . . 124

7.4 Calculated optical absorption spectrum of the intrinsic electron trap in a-SiO_2 127

8.1 A model of a-SiO_2 containing an Si–H bond and an Si–O–H bond. . . 133

8.2 Atomic configuration and spin density of the hydroxyl E′ centre and its precursor. 134

8.3 Histograms of the bond length distributions around the hydroxyl E′ center. 135

8.4 Histogram of the one-electron level of 116 configurations of the hydroxyl E′ centre. 136

8.5 Correlations between the one-electron levels and relative stabilities of the hydroxyl E′ center with the non-bonding Si– –O interaction. . . . 137

8.6 Formation energy of the hydroxyl E′ centre in a-SiO_2. 139

8.7 Histogram of the thermodynamic switching levels of the hydroxyl E′ centre. 140

8.8 Atomic structure and spin density of the neutral E′ centre. 142

8.9 The neutral E′ centre formed by trapping a hole at an Si–H bond. . . 144

8.10 A graph showing how the energetic position of the Si–H state against the nearest non-bonded O distance. 145

8.11 The effect of a nearby proton on the defect levels of the neutral E′ centre. 146

List of Tables

3.1 Bond lengths of the Si_3O_y clusters 41
3.2 Bond lengths and angles of Si_nO_n clusters optimised using COMB and ReaxFF. 42
3.3 Bond lengths of Si_n clusters optimised using COMB and ReaxFF. . . 44

4.1 Comparison of neutral oxygen vacancy geometries in different models 69
4.2 Comparison of positive oxygen vacancy dimer configuration geometries in different models 75
4.3 Geometry of the puckered configuration of the positive oxygen vacancy in different studies. 77
4.4 Principal values of the hyperfine tensor for the E′ centre 78

5.1 Hyperfine splittings of the Li electron trap in α-quartz. 99

6.1 Principal values of the hyperfine tensor of the electron trap in a-SiO_2 113

8.1 Hydrogen's reactions with a-SiO_2. 148

A.1 BKS Parameterisation for Si and O atoms used in this work. 155

List of Publications

The following publications are derived from work presented in this thesis:

1. A. -M. El-Sayed, Y. Wimmer, W. Goes, T. Grasser, A. L. Shluger, "Theoretical Models of Hydrogen-Induced Defects in Amorphous Silicon Dioxide", *Phys. Rev. B,* **92**, 014107 (2015)

2. A. -M. El-Sayed, K. Tanimura, A. L. Shluger "Electron Localization in Amorphous SiO_2: Optical Signatures of Deep Traps", *J. Phys.: Condens. Matter* **27**, 265501 (2015)

3. A. -M. El-Sayed, M. B. Watkins, T. Grasser, V. V. Afanasev, A. L. Shluger, "Hole Trapping at Hydrogenic Defects in Amorphous Silicon Dioxide", *Microelectron. Eng.* **147**, 141–144 (2015)

4. A. -M. El-Sayed, T. Grasser, V. V. Afanas'ev, A. L. Shluger, "Hydrogen Induced Rupture of Si–O Bonds in Amorphous Silicon Dioxide", *Phys. Rev. Lett.* **114**, 115503 (2015)

5. A. -M. El-Sayed, M. B. Watkings, A. L. Shluger, V. V. Afanas'ev, "Nature of Intrinsic and Extrinsic Electron Traps in Silicon Dioxide", *Phys. Rev. B* **89**, 125201 (2014)

6. A. -M. El-Sayed, M. B. Watkins, A. L. Shluger, V. V. Afanas'ev, "Identification of Intrinsic Electron Trapping Sites in Bulk Amorphous Silica from *Ab Initio*

Calculations", *Microelectron. Eng.* **109**, 68–71 (2013)

7. S. Ling, A. -M. El-Sayed, M. B. Watkins, V. V. Afanas'ev, A. L. Shluger, "A Computational Study of Si-H Bonds as Precursors for Neutral E′ centers in amorphous silica and at the Si/SiO_2 interface", *Microelectron. Eng.* **109**, 310–313 (2013)

8. A. -M. El-Sayed, A. L. Shluger, "Atomistic Modelling of Defects Implicated in the Bias Temperature Instability *in* Bias Temperature Instability for Devices and Circuits, Chapter 12, Springer (2014)

Acknowledgements

I would like to take this opportunity to offer my heartfelt appreciation to a number of people whose help and companionship was indispensable during four years over which this work was accomplished. Firstly, I am hugely indebted to Alex Shluger whose supervision provided unwavering support and guidance throughout my studies. I am similarly indebted to Matthew Watkins, whose ready willingness to answer any and all of my questions saved me from losing my mind. I would also like to thank the rest of the Shluger group who were always there for a scientific or computational discussion.

For providing me with the opportunity to work collaboratively with them, I thank Valery Afans'ev and Katsumi Tanimura. I also owe a huge amount of thanks to Tibor Grasser for our fruitful collaboration and for subsequently welcoming me into his group as a postdoctoral researcher.

Additionally, I extend my gratitude to the London Centre for Nanotechnology and the Thomas Young Centre for creating an environment that encouraged and nurtured my scientific curiosity with their regular seminars and paper discussions.

I thank the UK Doctoral Training Centre in Energy Demand Reduction and the Built Environment as well as the EPSRC for funding this work. I also thank the Materials Chemistry Consortium and the London Centre for Nanotechnology for providing me with the immense computational resources I needed to accomplish this work.

Finally, I thank my family and friends for their staunch support, understanding and inspiration.

To my parents, family and friends ...

1

Introduction

1.1 Background & Motivation

This thesis is focussed on the atomistic modelling of defective sites in amorphous silicon dioxide (a-SiO_2) and their ability to trap charge carriers. Although SiO_2 is known as a common constituent of sands around the world, it is widely used in technological applications. In particular, its amorphous form is used in electronic devices as an insulating layer in metal-oxide-semiconductor field effect transistors (MOSFET), an integral component of integrated circuits (IC). The effective performance of ICs has been improved over the decades by a process known as scaling, whereby the constituent MOSFETs' dimensions are scaled down in order to fit more of them within an IC of a given area. This process has been largely successful, allowing for the light-

ning fast improvements in performance we have seen in electronic devices since the first realization of the transistor in the late 1950s. Nowadays, the insulating layer of a-SiO_2 in a typical MOSFET in a commercially available electronic device can have a thickness as small as 1 nm. Due to this extreme scaling, a number of issues which adversely affect the performance of the device have come to the fore. Collectively, these are termed electronic device reliability issues and include phenomena such as leakage current, $\frac{1}{f}$ noise, stress-induced leakage current, and bias temperature instabilities. Many of these reliability issues implicate defective sites in a-SiO_2. Due to the very small dimensions of modern electronic devices and the complexity of their fabrication processes, identifying defects experimentally in these devices is highly challenging. Computational modelling of materials can offer a comprehensive insight into the atomistic and electronic structure of defects which can complement and enlighten experimental results. This thesis uses a number of computational modelling techniques to characterize defects in a-SiO_2 which can be involved in electronic device reliability issues.

In 2009, the UK doctoral training centre in energy demand reduction and the built environment, from whom I received my funding, was established. The aim of this centre is to perform research that will result in the reduction of energy demands in modern society throughout the lifetime of the researcher, fitting in with the Engineering and Physical Sciences Research Council's strategic plan of reducing carbon emissions and securing energy supplies. The production of electronic devices is an enormous global industry. For example, according to the consumer electronics association (CEA), the average household in the United States had 24 electronic devices in 2012.[1] Improving the reliability of the MOSFET, which is an integral component to all of these 24 devices, reduces the amount of energy wasted while trying to power the consumer electronics which are so ubiquitous in modern society and helps to accomplish the goal of energy demand reduction.

In addition, the Modelling of the Reliability and Degradation of Next Generation Nanoelectronic Devices (MORDRED) project funded by the European Union began

in 2011 and was aimed at using modelling techniques to develop our understanding of the reliability of electronic devices from an atomistic level and integrate these results into simulations of large-scale electrical circuits. Due to my funding arrangement and the chance to work with world-class researchers as part of the MORDRED project, I was drawn into the exciting world of atomistic modelling of defects in order to improve the reliability of electronic devices.

1.2 Electronic Device Reliability Issues

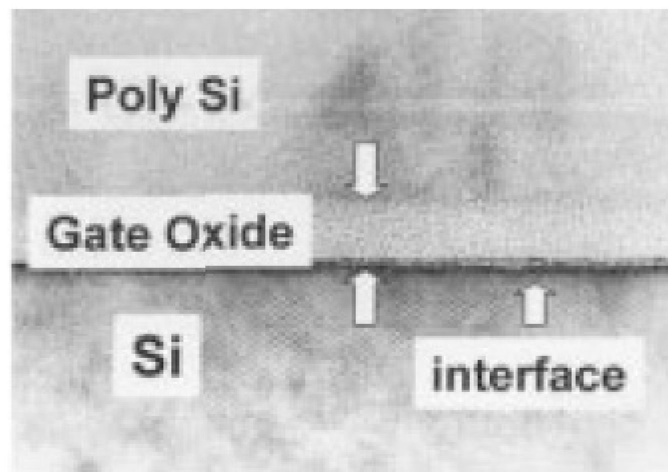

Figure 1.1: A transmission electron micrograph (TEM) image of a silicon MOSFET.[2]

Silicon based transistors are ubiquitous in modern electronic devices, being deployed as voltage-controlled switches. These switches are used to build up highly integrated logic circuits. Silicon transistors available today are usually of the MOSFET variety. They are built upon a crystalline silicon substrate with a thin layer of amorphous silicon dioxide sandwiched between the Si substrate and a metal. A transmission electron micrograph (TEM) of a silicon MOSFET is shown in Fig. 1.1. In addition, the silicon substrate has two terminals, the source and drain, separated by a channel. The thin oxide layer acts as an insulating layer while the metal acts as an electrode and is known as the gate. A schematic diagram of a MOSFET is shown in Fig. 1.2. Depending on the magnitude of the voltage applied between the gate electrode and the Si substrate, charge can be induced in the channel between

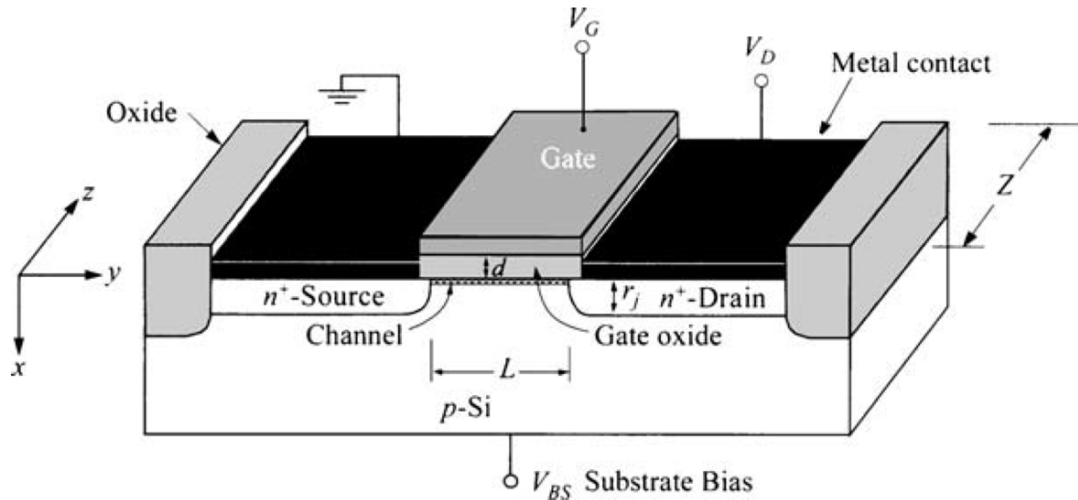

Figure 1.2: Typical structure of a MOSFET.[4] The oxide is sandwiched between the Si substrate and the gate electrode. There are two terminals in the Si substrate: the source and drain.

the source and drain and the potential difference between them allows a current to flow. The current flowing between the source and drain is effectively controlled by the voltage applied across the gate and the Si substrate.[3] Hence the MOSFET can be used as an amplifier, or more simply as a digital switch. This latter use has resulted in MOSFETs being used to construct logic circuits which work in conjunction with each other to form a typical IC.

The dominance of the Si/SiO_2 system is due in large part to the extremely high electrical quality of the interface and the ease with which silica can be grown on silicon. In this context, high quality means that very few defects exist at the Si/SiO_2 interface. Technologies today can produce Si/SiO_2 systems with as few as 10^{10}cm^{-2} defects at the interface.[5] Other material systems have in the past been considered, including systems with higher channel carrier mobility, but few systems so far can match the high electrical quality of the Si/SiO_2 interface. In many other systems, the high concentration of electrically active defects at the interface between two otherwise very suitable materials renders their use as a transistor ineffective.[6] This was in fact the case with Ge, a material with a higher carrier mobility and the first material studied for use as a transistor. In addition, SiO_2 has a wide band gap ($\approx$ 9 eV) providing a barrier which prevents charge carriers from leaving the channel.

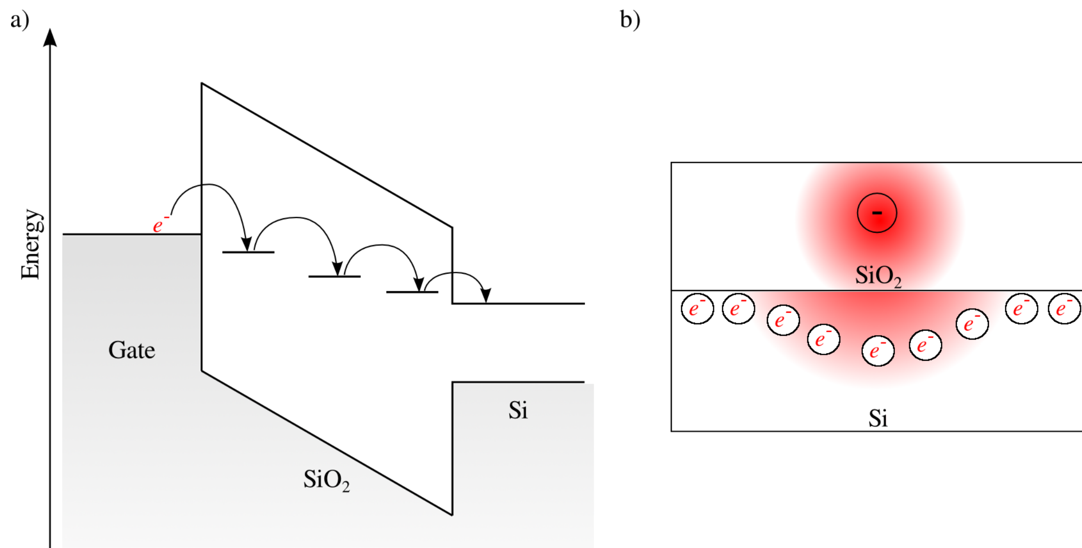

Figure 1.3: a) Schematic band diagram of tunnelling of electrons through defects in SiO_2 from a metal electrode to a Si substrate. The vertical axis represents the energy of the electrons. The shaded in region represents the electrons in the system. The horizontal levels represent defect in the oxide. A single electron highlighted in red is shown to tunnel from the metal electrode, known as the gate, into the SiO_2 defects and then into the Si substrate. b) Schematic of a defect in SiO_2 and how it affects the charge carriers in the Si substrate. The diagram shows SiO_2 deposited on Si. A negatively charged defect sits in the centre of the SiO_2 layer. It has an electrostatic effect whereby it repels the electrons in the channel of the Si substrate.

Tunnelling charge carriers interact with the oxide layer and the presence of defects is correlated with the tunnelling of the charge carriers.[7] A simplified band diagram shown in Fig. 1.3a shows a schematic diagram of charge carriers tunnelling from the gate to the Si substrate through defects in the oxide. A model, known as percolation theory, developed by Degrave *et al.*, implicates electrically active defects in the breakdown of the gate oxide.[8] In this model defects are randomly generated in the oxide when a voltage is applied across it for some period of time. The defects have energy levels in the oxide band gap and carriers can tunnel through these defects. Breakdown is achieved when enough of these defects exist and are close enough that they eventually provide a conduction path for the carriers from the channel to the gate electrode. This model correctly predicts the dependence of oxide thickness on breakdown but does not specify which defects are responsible for forming the conduction path.

Defects are also implicated in a number of other MOSFET reliability issues. In particular, charge trapping at point defects in the oxide have been implicated as the

cause of the negative bias temperature instability (NBTI).[9] NBTI is characterised by a shift in an intrinsic property of a MOSFET known as the threshold voltage after the application of a negative voltage across a MOSFET at elevated temperatures and for extended periods of time. It has been known since 1966[10] but has recently come to the fore as it became more pronounced with the smaller devices that resulted from scaling. It is almost universally attributed to charge trapping oxide defects and the creation of interface traps. It is thought that defects in the oxide can trap charge carriers from the channel. This trapped charge has an electrostatic effect on the channel which changes the properties of the MOSFET in a detrimental manner. A schematic of how the defect in an oxide can affect the charge carriers in the semiconductor substrate is shown in Fig. 1.3b. However, an understanding of its atomistic origins are still not clear.

1.3 Atomistic Nature of Defects Implicated in Reliability Issues

To aid in the understanding of reliability issues, computational methods are used to construct atomistic models of defects and assess what role they may play in these issues. Here, we briefly discuss two studies in the literature that attempted to identify defects which cause reliability issues in electronic devices using atomistic simulations.

Blöchl modelled a number of point defects in a-SiO_2 to assess their role in leakage currents. As mentioned in the previous section, leakage currents are a major concern for the reliable design of MOSFET devices.[11] Experimental results show that atomic hydrogen can induce a high concentration of defects in a-SiO_2[12–14] suggesting that H can be somehow involved in these leakage currents. Blöchle modelled hydrogen related defects using density functional theory (DFT) in a periodic cell of α-quartz cell containing 24 SiO_2 units. They included interstitial hydrogen, oxygen vacancies and their complexes. To assess their role in leakage currents, he evaluated experimental data and showed that the defects involved should have a small relaxation energy upon

trapping charge and that they should have a defect level where the Si band gap is located relative to SiO_2. Atomic hydrogen interstitials were found to be unstable in the neutral charge state, instead being thermodynamically favourable in either the positive or negative charge states. Its defect levels were found to be too close to the SiO_2 valence band for it to have a significant role in leakage currents. Oxygen vacancies were also found to have defect levels which render it useless for carrying leakage currents. However, the hydrogen bridge was found to satisfy both the criteria for leakage current: it displays small relaxations upon trapping and it has a switching level in the middle of the Si band gap. His model of the hydrogen bridge is shown in Fig. 1.4.

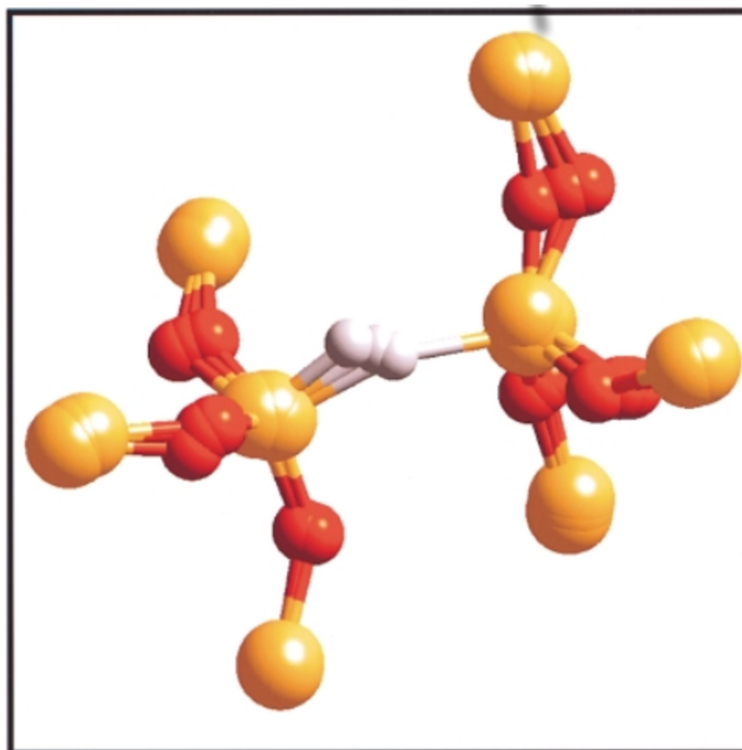

Figure 1.4: Atomistic structure of the hydrogen bridge in the neutral, negative and positive charge states. The relaxations are relatively small compared to relaxations of the oxygen vacancy defect in SiO_2.[11]

Schanovsky *et al.* investigated the atomistic nature of the defects that could be involved in NBTI.[15] Using *ab initio* calculations, they modelled the oxygen vacancy and hydrogen bridge defects in periodic cells of α-quartz containing 72 atoms. DFT was used along with the Perdew, Burke and Ernzerhof (PBE) functional and the wave

functions were expanded in a plane wave basis set. The total energies calculated for these defects were then used as parameters to calculate the capture and emission time constants from a semiconuctor substrate into the defects and compared to experimental results for NBTI. They showed that neither the oxygen vacancy nor the hydrogen bridge defects in α-quartz could be responsible for NBTI as their defect levels would result in much slower capture times. However, it is important to note that the reported results were made in crystalline SiO_2 samples, while the measurements were made on devices containing a-SiO_2.

1.4 Scope of this Work

This thesis presents atomistic calculations of a number of defects in silicon dioxide which can capture charge. Each defect is extensively characterized and their formation processes are also discussed. Analysis of these defects shows that they may be involved in electronic device reliability issues.

We begin by discussing the methods used to perform these calculations. A brief overview of molecular dynamics is presented. This is followed by an overview of density functional theory (DFT) and a number of advanced techniques associated with solving the DFT equations. Classical charge-variable potentials are then discussed. They are a recent development in the field of computational materials science which allow the charge of each particle in a system to vary dynamically with the charges being dependent on the instantaneous geometry of the system. This should allow one, in principle, to be able to study an element in varying charge states, such as the transition of silicon from its elemental to fully oxidised form. The embedded cluster method is then presented, and the methods chapter concludes with a discussion of climbing-image nudged elastic band (CI-NEB), used to calculate the energetic barriers of atomistic processes.

The following chapter discusses the process of modelling a-SiO_2 and the Si/SiO_2 interface. Making amorphous models is challenging as they have no long-range order

and therefore its structure has not been atomistically resolved by experiment. In order to construct a-SiO_2 and the Si/SiO_2 interface, a charge-variable potential was chosen based on its stability in a molecular dynamics simulation and its ability to describe a number of SiO_x clusters with Si in varying charge states. Then, a melt-and-quench method is used to generate 320 models of a-SiO_2. The models' geometrical and electronic properties were characterized extensively and compared to experiment where appropriate. This comparison to experiment is the strongest justification available at present that these models are indeed representative of a-SiO_2, describing both the short- and long-range order of the material. The same charge-variable potential was then used to construct a model of the Si/SiO_2 interface. This model was compared to experiment and shown to agree with a number of experimental observations.

The oxygen vacancy was then calculated in both crystalline and amorphous SiO_2 using DFT and the amorphous models made in the preceding chapter. The vacancy is a well-known defect that has been characterized both experimentally and theoretically in the literature. The results in this chapter are compared to previous studies and show excellent agreement, indicating that the methods used can reliably predict defect structures in SiO_2.

The next chapter discusses electron trapping at impurities in α-quartz. Models for both Ge- and Li-doped quartz were characterized extensively showing that the electron trapping at these centres is qualitatively very similar. Electron trapping at Ge in quartz has been discussed in the literature.[16] However, this is the first characterization of the atomistic structure of the electron trap in Li-doped quartz.

Electron trapping at intrinsic sites is discussed in the following chapter. Due to the disorder of a-SiO_2, the bottom of the conduction band is actually partially localized. It was found that when an extra electron is added to the bottom of the conduction band, it relaxes into a trapped state deep in the a-SiO_2 band gap. The key to this relaxation was found to be a wide O–Si–O angle, which naturally exists in a-SiO_2. Electron trapping at intrinsic sites was also studied in α-quartz. However, due to all the O–Si–O angles being the same, the trapping process requires overcoming

an energetic barrier. The character of localization at intrinsic sites was shown to be similar to that at the extrinsic sites. The concentration of electron traps was calculated in a model of a-SiO_2 containing almost 500,000 atoms and was shown to agree well with experimental estimates of electron traps involved in electronic device degradation processes.

The optical absorption spectrum of the intrinsic electron trap was calculated using the embedded cluster method and time-dependent density functional theory (TD-DFT) for the first time. Characterization of the electronic structure of the electron trap in the embedded cluster model agree very well with the previous chapter's results calculated in a periodic model. The calculated optical absorption spectrum shows a strong excitation at 3.7 eV from the electron trapping state into the bottom of the a-SiO_2 conduction band. In addition, there is also a strong excitation from the top of the a-SiO_2 valence band into the electron trap. These excitations correlate strongly with experimental optical absorption spectra measured at low temperature.

Interactions of hydrogen with a-SiO_2 are presented in the final chapter. Both atomic and molecular hydrogen were shown to interact with a-SiO_2 to produce similar defect states. For the first time, calculations show that atomic hydrogen interacts with strained Si–O bonds, breaking them and resulting in a 3-coordinated Si facing a hydroxyl group. A model of the formation and annihilation of this defect is presented in this chapter. Molecular hydrogen was shown to create Si–H bonds when introduced into an SiO_2 melt. The states of these bonds sit near the top of the valence band and were shown to trap a hole. This process releases a proton and leaves behind a 3-coordinated Si whose state in the band gap is highly affected by how far it is from the nascent proton. The role of the hydrogen related defects in electronic device reliability issues is discussed.

2

Theoretical Background and Methods

2.1 Introduction

The aim of this chapter is to give a detailed overview of the theoretical methods that were used to obtain the results presented in this thesis. Modelling point defects in crystalline and amorphous materials is a complicated affair due to their deviation from an ideal model, ths requiring the use of advanced modelling techniques. The chapter begins by covering the theory of molecular dynamics, which is used to evolve the positions of particles in a many-body system. It then goes on to explain the basics of density functional theory (DFT) and further approximations which were employed in the calculations presented in this thesis. This is followed by an introduction to classical potentials and the recently developed charge-variable potentials COMB and

ReaxFF. The embedded cluster method is briefly described and the chapter concludes with the nudged elastic band method (NEB) for calculating reaction pathways.

2.2 Molecular Dynamics

Molecular dynamics is a computer simulation method in which the force on each particle in a system is calculated and integrated to allow each particle to evolve its position and velocity, generating a trajectory for the system. Using some form for the potential energy, which can be described classically (see section 2.4) or quantum mechanically (see section 2.3), the force on each particle is calculated as the differential of the vector sum of its interactions with all other particles in the system:

$$F(\boldsymbol{r}) = \sum_{i=1}^{N} -\frac{dU}{d\boldsymbol{r}_i}, \tag{2.1}$$

where $F(\boldsymbol{r})$ is the total force on the atom, U is the potential energy, N is the total number of particles, and $\boldsymbol{r}_i$ are the coordinates of atom i. The acceleration can be determined from the force according to Newton's second law of motion, generating the trajectory of motion of the system:

$$F = ma = m\frac{d^2\boldsymbol{r}}{dt^2}. \tag{2.2}$$

Using this method with a potential energy surface which depends on each particle's position relative to all other particles constitutes a complex many-body problem. The coupling of the particles' motions makes it extremely difficult to calculate the trajectory analytically, so one must use a numerical method to calculate the trajectory.

One of the most popular and widely used methods of integrating the equations of motion when using pairwise continuous potential energy surfaces is the *Verlet* algorithm.[17] The integration is broken down into small steps separated by a fixed time which we call the time step. Writing out the position at the next and previous time step as Taylor expansions of position up to third order, we obtain for the next time

step:

$$\boldsymbol{r}(t+\delta t)=\boldsymbol{r}(t)+\delta t\boldsymbol{v}(t)+\frac{1}{2}\delta t^2\boldsymbol{a}(t)+\frac{1}{6}\delta t^3\boldsymbol{b}(t)+\ldots, \tag{2.3}$$

where $r(t)$ are the positions; δt is the time step; $\boldsymbol{v}(t)$, $\boldsymbol{a}(t)$, and $\boldsymbol{b}(t)$ are the first (also known as velocity), second (known as acceleration), and third order differentials of position, respectively. The position at the previous time step is:

$$\boldsymbol{r}(t-\delta t)=\boldsymbol{r}(t)-\delta t\boldsymbol{v}(t)+\frac{1}{2}\delta t^2\boldsymbol{a}(t)-\frac{1}{6}\delta t^3\boldsymbol{b}(t)+\ldots. \tag{2.4}$$

Adding equations (2.3) and (2.4) gives:

$$\boldsymbol{r}(t+\delta t)=2\boldsymbol{r}(t)-\boldsymbol{r}(t-\delta t)+\delta t^2\boldsymbol{a}(t). \tag{2.5}$$

Using this equation, the new positions can be calculated from the acceleration and each particle's previous positions. It can be seen in equation 2.5 that the 3rd order terms in equations 2.3 and 2.4 cancel out. This in fact makes the use of equation 2.5 an order more accurate than the use of equation 2.3 alone. The velocities are not explicitly defined in the Verlet integration scheme but can be calculated by dividing the difference between the positions at t+δt and t by 2δt:

$$\boldsymbol{v}(t)=\frac{\boldsymbol{r}(t+\delta t)-\boldsymbol{r}(t)}{2\delta t}. \tag{2.6}$$

Using the information laid out in this section one can set up an algorithm to evolve each particle's position and obtain a trajectory from the particles' forces. To obtain the forces one can use a variety of methods; for example, a classical (see section 2.4) or a first principles quantum mechanics approach (see section 2.3).

2.3 Density Functional Theory

DFT is a theory providing information on the electronic properties and chemical bonding of materials. It is, in principle, an *ab initio* method, meaning that it requires no parameters except for the fundamental properties of the material being studied, e.g. atomic mass, mass of an electron, etc. DFT follows from the Hohenberg-Kohn theorems,[18] the first of which states that there is a one-to-one mapping of the density, $\rho(\boldsymbol{r})$, of a system to its external potential, v_{ext}; in other words, the density of a system uniquely determines its external potential. This means that all the properties of a system can be determined from its density, and the total energy of a system can be written as a functional of its density as:

$$E[\rho(\boldsymbol{r})] = E^T[\rho(\boldsymbol{r})] + E^V[\rho(\boldsymbol{r})] + E^H[\rho(\boldsymbol{r})] + E_{XC}[\rho(\boldsymbol{r})], \tag{2.7}$$

where $E^T[\rho(\boldsymbol{r})]$ is the kinetic energy, $E^V[\rho(\boldsymbol{r})]$ is the potential energy, $E^H[\rho(\boldsymbol{r})]$ is the Hartree energy, and $E^{XC}[\rho(\boldsymbol{r})]$ is the exchange-correlation energy of the system. Writing the energy of a system as a functional of its density reduces a many-body problem into an equation which depends on the three spatial variables of the density. The final term, $E^{XC}[\rho(\boldsymbol{r})]$, is the exchange-correlation energy functional and contains all the complicated many-body effects that have not been described within all the other energy terms. The second Hohenberg-Kohn theorem states that the true ground-state density of the system is the density which minimises the energy of the system, i.e.:

$$\begin{aligned} E[\rho(\boldsymbol{r})] &\geq E_0 \text{ for } \rho(\boldsymbol{r}) \neq \rho_{gs}(\boldsymbol{r}), \\ E[\rho(\boldsymbol{r})] &= E_0 \text{ for } \rho(\boldsymbol{r}) = \rho_{gs}(\boldsymbol{r}), \end{aligned} \tag{2.8}$$

where $\rho_{gs}(\boldsymbol{r})$ is the ground-state density and E_0 is the ground state energy. Thus, by minimising equation 2.7, the ground-state density and energy can be obtained.

Equation 2.7 means that the total energy of the system can be calculated from the 3 dimensional density. However, due to a lack of approximations for $E^T[\rho(\boldsymbol{r})]$, these calculations are, as yet, impractical for the accurate description of materials. In

a landmark paper, Kohn and Sham introduced an auxiliary system of non-interacting electrons which have the same ground-state density as the interacting system which we can call the Kohn-Sham system (KS).[19] As the KS particles are non-interacting, the wave function can be written as a Slater determinant:

$$\Psi(\boldsymbol{r_1}, \ldots, \boldsymbol{r_N}) = \frac{1}{\sqrt{N!}} \begin{vmatrix} \psi_1(\boldsymbol{r_1}) & \psi_2(\boldsymbol{r_1}) & \ldots & \psi_N(\boldsymbol{r_1}) \\ \psi_1(\boldsymbol{r_2}) & \psi_2(\boldsymbol{r_2}) & \ldots & \psi_N(\boldsymbol{r_2}) \\ \vdots & \vdots & \vdots & \vdots \\ \psi_1(\boldsymbol{r_N}) & \psi_2(\boldsymbol{r_N}) & \ldots & \psi_N(\boldsymbol{r_N}) \end{vmatrix}, \tag{2.9}$$

where $\psi_i(\boldsymbol{r_j})$ are single particle orbitals. The electron density can then be obtained from these orbitals using the Born interpretation of the wave function:

$$\rho(\boldsymbol{r}) = \sum_{i=1}^{N} |\psi_i(\boldsymbol{r})|^2 = |\Psi|^2. \tag{2.10}$$

The total energy of the system can be evaluated as the expectation value of the Hamiltonian of this wave function. An external potential, v_{eff} is chosen so that the true ground-state density of the system is reproduced from the KS system. The total energy of the system of non-interacting electrons is thus:

$$E_{gs} = \langle \Psi_{gs}[\rho] | \hat{H} | \Psi_{gs}[\rho] \rangle, \tag{2.11}$$

where:

$$\hat{H} = -\frac{\hbar \nabla^2}{2m} + v_{eff}, \tag{2.12}$$

and:

$$v_{eff}(\boldsymbol{r}) = v_{ext}(\boldsymbol{r}) + v_{Hartree}(\boldsymbol{r}) + v_{xc}(\boldsymbol{r}) = v_{ext}(\boldsymbol{r}) + \int d\boldsymbol{r}' \frac{\rho(\boldsymbol{r})}{|\boldsymbol{r} - \boldsymbol{r}'|} + \frac{\delta E_{xc}[\rho]}{\delta \rho(\boldsymbol{r})}, \tag{2.13}$$

where v_{ext} is the interaction of the electrons with the ions in the system, $v_{Hartree}$ is the electron-electron repulsion and v_{xc} is the exchange-correlation potential. Using the Kohn-Sham formulation of the Schrödinger equation one can calculate the single-

particle orbitals:[19]

$$\left(-\frac{\hbar\nabla^2}{2m}+v_{\text{eff}}(\boldsymbol{r})\right)\psi_i(\boldsymbol{r})=\varepsilon_i\psi_i(\boldsymbol{r}), \tag{2.14}$$

where $v_{\text{eff}}(\boldsymbol{r})$ is the effective potential, $\psi_i(\boldsymbol{r}_i)$ is the Kohn-Sham orbital and ε_i is the eigenvalue of the Kohn-Sham orbital. Equation 2.14 is calculated self consistently starting with an initial guess for the electron density which can be inserted into the effective potential. Once the new density converges with the density from the previous step, the Kohn-Sham equations have converged and the ground-state density has been obtained.

Although DFT has had considerable success describing ground-state properties, it is largely unsuitable for the calculation of excited state properties. However, the time-dependent extension to DFT (TDDFT) has been used to calculate excited state properties rather successfully.[20–22] The theory behind TDDFT is, unsurprisingly, rather similar to DFT. A one-to-one mapping between the time-dependent ground state and a time-dependent external potential up to a time-dependent but spatially independent function is established in the time-dependent extension to the Hohenberg-Kohn theorem: the Runge-Gross theorem.[23] Total energy is not a conserved quantity in TDDFT, thus there is no analogue of the variational principle, and instead the energies are defined as the stationary points on the quantum mechanical action integral:

$$A[\Psi]=\int_{t_0}^{t_1}\mathrm{d}t\langle\Psi(t)|i\frac{\delta}{\delta t}-\hat{\mathrm{H}}(t)|\Psi(t)\rangle, \tag{2.15}$$

where $\Psi(t)$ is the time-dependent wave function (which can be uniquely obtained from the time-dependent density) and $\hat{\mathrm{H}}(t)$ is the Hamiltonian of the system. The time-dependent density of the system is then obtained by finding the stationary points on the action potential, i.e. the points where $A[\Psi]=0$. To obtain the time-dependent density, a Kohn-Sham system of non-interacting particles in a time-dependent potential is constructed, analogous to the Kohn-Sham system in DFT:

$$i\frac{\delta}{\delta t}\psi_i(t)=\left(-\frac{1}{2}\nabla^2+v_{eff}(t)\right)\psi_i(t), \tag{2.16}$$

where $\psi_i(t)$ are the time-dependent single particle orbitals and $v_{eff}(t)$ is the time-dependent effective potential:

$$v_{eff} = v_{ext}(t) + v_{Hartree}(t) + v_{xc}(t), \tag{2.17}$$

where $v_{ext}(t)$ now includes a time-dependent external potential perturbing the system (e.g. a laser) as well as the static potential generated by the ions, $v_{Hartree}(t)$ is the time-dependent Hartree potential, and $v_{xc}(t)$ is the time-dependent exchange-correlation potential. The time-dependent density can then be constructed from the time-dependent single particle orbitals, once again analogous to DFT:

$$\rho(t) = \sum_{i=1}^{N} |\psi_i(t)|^2, \tag{2.18}$$

where $\rho(t)$ is the time-dependent density. By self-consistently calculating a stationary point on the action integral, one obtains the time-dependent density of the system. To calculate the excitation energies and their respective oscillation strengths, the linear response of the time-dependent density has to be examined. After a number of algebraic manipulations and application of the Tamm-Dancoff approximation, this leads to the eigenvalue equation:[21]

$$\mathbf{AX} = \omega \mathbf{X}, \tag{2.19}$$

where ω are the excitation energies, and the eigenvectors $\mathbf{X}$ can be used to calculate the oscillator strengths. The elements of matrix $\mathbf{A}$ are given as:

$$A_{ia,jb} = \delta_{ij}(\epsilon_a - \epsilon_b) + (ij|jb) + (ia|f_{xc}|jb), \tag{2.20}$$

where $(ab|bc)$ are two electron integrals represented in Mulliken notation, and f_{xc} is the time-dependent exchange-correlation kernel. Solving this eigenvalue problem is equivalent to finding the excitation energies which are at the poles of the density

response equations.[24]

2.3.1 Gaussian Plane Waves Method

In a typical DFT calculation, the Kohn-Sham orbitals are described within a chosen basis set of functions. Two popular functions typically used for solving the Kohn-Sham equations are Gaussian and plane wave functions. Each type has its advantages and disadvantages. Gaussian basis sets are atomically centred functions. They allow for a compact description of the wave function and efficient algorithms exist to analytically calculate matrix integrals. However, Gaussian basis sets do not describe orbitals properly near the nucleus and can suffer due to the incomplete nature of the basis set. Plane waves are used as basis sets due to their indifference to the atomic coordinates and species. Their periodic nature means they are a natural choice of basis set when describing periodic systems, and plane waves, in principle, form a complete basis. Fast Fourier transform techniques allow for a faster calculation of the Hartree energy and checking the convergence of a calculation using a plane wave basis set is a straightforward matter. However, describing the density properly in a plane wave basis usually requires a larger number of functions relative to a Gaussian basis set and plane waves represent regions of empty space with the same accuracy as a region which contains an atom, leading to unnecessary computational expense. Although in principle plane waves form a complete basis, it is necessary to truncate the basis set in order to make a calculation feasible.

The Gaussian and plane waves method[25] (GPW) is designed so that the density of the system is represented in both bases in order to use the more time-advantageous basis set for the various elements of the calculation while maintaining accuracy. The following describes both Gaussian and plane wave basis sets, followed by their combination to make the GPW method.

Gaussian Basis Sets

The density represented in a Gaussian basis set is written as:

$$\rho(\boldsymbol{r}) = \sum_{i=1}^{N} |\psi_i(\boldsymbol{r})|^2, \tag{2.21}$$

where $\rho(\boldsymbol{r})$ is the density, N is the number of electrons, and $\psi_i(\boldsymbol{r})$ is the i'th molecular orbital. The molecular orbitals can be approximated using the linear combination of atomic orbitals (LCAO) method, where each molecular orbital is described as:

$$\psi = \sum_{j} C_{mi}\psi_j, \tag{2.22}$$

where C_{mi} is the mixing coefficient of the atomic orbital and ψ_i is the atomic orbital which is a contracted Gaussian, made of:

$$\psi = \sum_{\mu} C_{\mu n} g_{\mu}, \tag{2.23}$$

where $C_{\mu i}$ is the mixing coefficient and g_μ is a primitive Gaussian function ($g_\mu = \ldots e^{-\alpha r^2}$). In a typical calculation, the coefficients of the molecular orbitals, C_{mi}, are varied until the ground-state density is obtained while the mixing coefficients of the contracted Gaussian, $C_{\mu n}$ remain fixed.

Plane Wave Basis Sets

The density represented in a plane wave basis set is:

$$\tilde{\rho}(\boldsymbol{r}) = \frac{1}{\Omega} \sum_{\mathbf{G}} \tilde{\rho}(\mathbf{G}) e^{i\mathbf{G}\cdot\mathbf{r}}, \tag{2.24}$$

where $\tilde{\rho}(\boldsymbol{r})$ is the density, Ω is the volume of the cell, $\mathbf{G}$ are the reciprocal lattice vectors and $\tilde{\rho}(\mathbf{G})$ are the expansion coefficients. The density, $\tilde{\rho}(\boldsymbol{r})$ is determined from $\rho(\boldsymbol{r})$ using Fourier transforms on a real-space grid.

Combining Gaussians and Plane Waves to Make the Gaussian Plane Waves Method

The electrons in the system can be split into those near the nucleus whose form does not change much during a calculation, known as core electrons, and those which sit away from the nucleus which are involved in chemical reactions, known as the valence electrons. Replacing the core electrons with what is known as a pseudopotential[26] provides a smoothly varying density which can be easily mapped from the Gaussian basis set to a plane wave basis set. Fewer Gaussian functions are required to produce the characteristic cusp behaviour at the nucleus, and due to the smoothly varying nature of pseudopotentials, less plane waves are required. This allows for easier mapping of the density from a Gaussian to a plane wave basis set. The Kohn-Sham equation (see equation 2.7) within these two basis sets is calculated as:

$$E[\rho] = \sum_{\mu v} P^{\mu v} \langle \psi_\mu(\boldsymbol{r})| - \frac{1}{2}\nabla^2 |\psi_v(\boldsymbol{r})\rangle + \langle \psi_\mu(\boldsymbol{r})|V_{loc}^{PP}|\psi_v(\boldsymbol{r})\rangle + \langle \psi_\mu(\boldsymbol{r})|V_{nl}^{PP}|\psi_v(\boldsymbol{r})\rangle + 2\pi\Omega \sum_{\mathbf{G}} \frac{\tilde{\rho} * (\mathbf{G})\rho(\mathbf{G})}{G} + \int \varepsilon_{xc}(\boldsymbol{r}) d\boldsymbol{r}, \quad (2.25)$$

where $P^{\mu v}\langle \psi_\mu(\boldsymbol{r})| - \frac{1}{2}\nabla^2|\psi_v(\boldsymbol{r})\rangle$ is the kinetic energy, $\langle \psi_\mu(\boldsymbol{r})|V_{loc}^{PP}|\psi_v(\boldsymbol{r})\rangle + \langle \psi_\mu(\boldsymbol{r})|V_{nl}^{PP}|\psi_v(\boldsymbol{r})\rangle$ are the local and non-local parts of the pseudopotential, $2\pi\Omega \sum_{\mathbf{G}} \frac{\tilde{\rho}*(\mathbf{G})\rho(\mathbf{G})}{G}$ is the Hartree energy and $\int \varepsilon_{xc}(\boldsymbol{r})dr$ is the exchange correlation energy. The density within a Gaussian basis set is used to calculate the kinetic and potential energy analytically. Use of the Gaussian product theorem makes this a relatively trivial endeavour. Mapping the density onto the plane wave basis allows one to use fast Fourier techniques to calculate the Hartree energy. This method significantly reduces the computational cost of DFT calculations allowing one to study much larger systems than if one were to use either basis set on its own. The GPW method is implemented in the Quickstep[27] module within the CP2K code.[28]

2.3.2 Hybrid Functionals and the Auxiliary Density Matrix Method

A huge number of approximations exist in the literature and a judicious choice of functional is necessary for the accurate calculation of a material's properties. Exchange-correlation functionals were initially based on local measurements of the homogeneous electron gas[29] and gradient-corrected modifications.[30] These functionals, however, suffer from two prominent shortcomings which are particularly relevant to the study of defects in solid state systems. They tend to give wrong descriptions of the band gap, with both LDA and GGA underestimating it by up to 40%.[31] In addition, these functionals have trouble describing the localized defect states which are known to exist experimentally.[32,33] Recent developments have resulted in more advanced approximations, such as the set of functionals known as hybrid functionals which use a portion of Hartree-Fock (HF) exchange which is explicitly calculated for all electrons in the system. The band gaps and localized defect states calculated using these hybrid functionals show significant improve compared to the local and gradient-corrected approximations. The main results of this thesis have made use of hybrid functionals, including the B3LYP and PBE0_TC_LRC hybrid functionals[34] which both contain a portion of HF exchange energy. It is calculated from the density matrix, $P =< \psi_\mu|\rho|\psi_\lambda >$ and the two electron integrals as:

$$E_x^{HF}[P] = -\frac{1}{2}\sum_{\lambda\sigma\mu v} P^{\mu\sigma}P^{\lambda v}\langle\mu v|\lambda\sigma\rangle, \tag{2.26}$$

where P is the density matrix and $\langle\mu v|\lambda\sigma\rangle$ are the exchange integrals, described as:

$$\langle\mu v|\lambda\sigma\rangle = \int\int \psi_\mu^*(\boldsymbol{r}_1)\psi_v^*(\boldsymbol{r}_1)\frac{1}{\boldsymbol{r}_{12}}\psi_\lambda(\boldsymbol{r}_2)\psi_\sigma(\boldsymbol{r}_2), \tag{2.27}$$

where ψ are the single-particle orbitals. The HF exchange energy is computationally expensive, scaling to the fourth power of the number of basis functions used in a calculation as can be seen above. The form of the exchange-correlation energy in the

PBE0_TC_LRC functional is:

$$E_{xc}^{PBE0_TC_LRC} = \alpha E_x^{HF,TC} + \alpha E_x^{PBE,LRC} + (1-\alpha)E_x^{PBE} + E_c^{PBE}, \tag{2.28}$$

where α is a parameter that controls the amount of HF exchange, typically defined as 0.2 in the literature and is the value used in this thesis unless otherwise stated.[34] TC is a truncated exchange operator where the $\frac{1}{r_{12}}$ term becomes zero if r_{12} exceeds a pre-defined r_c cut off value. The exchange-correlation energy in the B3LYP functional is:[35]

$$E_{xc}^{B3LYP} = E_x^{LDA} + a_0(E_x^{HF} - E_x^{LDA}) + a_x(E_x^{GGA} - E_x^{LDA}) + E_c^{LDA} + a_c(E_c^{GGA} - E_c^{LDA}), \tag{2.29}$$

where $a_0 = 0.20$, $a_c = 0.72$, and $a_c = 0.81$. LDA represents exchange-correlation in the local density approximation,[29] while GGA represents gradient-corrected exchange-correlation.[30]

To reduce the computational cost of calculating HF exchange integrals, the auxiliary density matrix method (ADMM) was employed in many of the calculations presented in this thesis. It constructs a much smaller density matrix using an auxiliary basis set. The calculation of HF exchange can be performed using this basis set and the smaller density matrix, thus reducing the number of calculations needed. The auxiliary basis set is described as:

$$\tilde{\psi} = \sum_{\mu} \tilde{C}_{\mu i} \tilde{\psi}_i(r), \tag{2.30}$$

where $\tilde{\psi}$ is the wave function in the smaller auxiliary basis set, $\tilde{C}_{\mu i}$ is the Gaussian orbital coefficient and $\tilde{g}_i(r)$ is the Gaussian orbital. The density matrix is constructed from the orbital coefficients as:

$$\tilde{P}^{\mu v} = \sum_{i} \tilde{C}_{\mu i} \tilde{C}_{vi}. \tag{2.31}$$

The orbital coefficients for the auxiliary basis set and auxiliary density matrix can be obtained by minimising the square difference between the wave functions in the original basis set and the auxiliary basis set. The HF exchange energy can then be calculated in this basis set as:

$$\begin{aligned} E_x^{HF}[P] &= E_x^{HF}[\tilde{P}] + (E_x^{HF}[P] - E_x^{HF}[\tilde{P}]), \\ &\approx E_x^{HF}[\tilde{P}] + (E_x^{DFT}[P] - E_x^{DFT}[\tilde{P}]), \end{aligned} \tag{2.32}$$

where $E_x^{HF}[\tilde{P}]$ is the HF exchange energy while $E_x^{DFT}[P]$ is the exchange energy calculated using GGA. It is assumed that the difference in the exchange calculated using different basis sets using GGA and HF is approximately the same. Using this auxiliary density matrix and the bottom half of equation 2.32 can greatly reduce the cost of a DFT calculation using a hybrid functional.

2.4 Classical potentials

The problem with *ab initio* calculations, like DFT discussed in section 2.3, is that they are computationally expensive. The advantage of using a classical potential is that one can model systems containing up to billions of atoms and simulations can be run for up to a microsecond.[36,37] To calculate equilibrium energies and structures one can use a classical interatomic potential along with some simulation method, e.g. Molecular dynamics or minimisation algorithms. The disadvantages of using classical potentials is that you don't calculate the electronic structure of the system, which is essential when modelling defects as their electronic structure can deviate strongly from that of the ideal material. Interatomic potentials have to be parametrised, usually to a particular quantity of interest. For instance, the BKS potential,[38] used to model silica, can reproduce the structure and density of crystalline silica polymorphs quite well but has trouble describing its phononic properties and certain crystalline transitions.[39] Potentials are designed to be as transferable as possible but this is

difficult to do as it is hard to capture the physics of a species through all possible chemical environments using a simple potential. Parameterizing a potential is one of the less glamorous aspects of modelling but is needed to obtain results that can reliably explain physical phenomena.

Often times it is more convenient to start off with a well parameterized potential and fine tune it to accurately describe the desired quantity. An interatomic potential proposed by Watanabe[40] was developed as an extension to the Stilinger-Weber potential, which accurately models crystalline silicon, to model systems containing both silicon and silica and has been used to study the structure of Si/SiO_2 interface. Many potentials exist which describe bulk silica and silicon but few exist which are transferable enough to describe the transition of silicon from its elemental to its fully oxidised silica form.

2.4.1 Charge variable potentials

A problem which can prevent a potential from being truly transferable is the varying charge state of a species when it is in different materials, e.g. Si in bulk silicon and SiO_2. Conventional potentials contain the charge of a species as a fixed parameter, thus a particle can not be simulated undergoing a change in charge state. To overcome this problem, Rappé and Goddard developed a scheme which allows a particle's charge to be calculated from the instantaneous geometries of the particles in a system.[41] The scheme is based on the electronegativity equalisation principle which states that the electronegativities of species coming together becomes constant.

$$\chi_A = \chi_B = \ldots = \chi_N. \tag{2.33}$$

The effective electronegativity of a system of particles is the geometric mean of the electronegativities of the species.[42] One can define an energy for each atom with

respect to its charge as a Taylor expansion about the neutral atom:

$$E_i(q) = E_{i0} + q_i \left(\frac{\delta E}{\delta q}\right)_{i0} + \frac{1}{2}\, q_{i0}^2 \left(\frac{\delta E}{\delta q}\right)_{i0}. \tag{2.34}$$

The energy required to make an ion of charge +1 is assigned to the ionisation potential while a charge of -1 is termed the electron affinity. They can be calculated as:

$$E_i(0) = E_{i0}, \tag{2.35}$$

$$E_i(+1) = E_{i0} + \left(\frac{\delta E}{\delta q}\right)_{i0} + \frac{1}{2}\left(\frac{\delta E}{\delta q}\right)_{i0} = E_{i0} + IP, \tag{2.36}$$

$$E_i(-1) = E_{i0} - \left(\frac{\delta E}{\delta q}\right)_{i0} + \frac{1}{2}\left(\frac{\delta E}{\delta q}\right)_{i0} = E_{i0} + EA. \tag{2.37}$$

Mulliken defined electronegativity as the average of the electron affinity and ionisation potential. Using this definition and the results above we can say:

$$\frac{1}{2}\left(\frac{\delta^2 E}{\delta q^2}\right) = \left(\frac{\delta E}{\delta q}\right)_{i0} - EA = IP - \left(\frac{\delta E}{\delta q}\right)_{i0} \rightarrow 2\left(\frac{\delta E}{\delta q}\right)_{i0} = IP + EA \rightarrow,$$

$$\left(\frac{\delta E}{\delta q}\right)_{i0} = \frac{1}{2}(IP + EA) = \chi_i^o, \tag{2.38}$$

and:

$$\left(\frac{\delta E}{\delta q}\right)_{i0} = IP - \frac{1}{2}\left(\frac{\delta^2 E}{\delta q^2}\right) = EA + \frac{1}{2}\left(\frac{\delta^2 E}{\delta q^2}\right) \rightarrow,$$

$$\frac{1}{2}\left(\frac{\delta^2 E}{\delta q^2}\right) = IP - EA = J_{ii}^o, \tag{2.39}$$

where χ_i^0 and J_{ii}^0 are the Mulliken electronegativity and the self-Coulomb interaction (also sometimes referred to as the idempotential). Both these quantities can be obtained from experimental data. To determine the equilibrium charge of the species in a system, we now write the total electrostatic energy of a system as:

$$E(q_1, ..., q_N) = \sum_i^N \left(E_{i0} + \chi_i^o q_i + \frac{1}{2} J_{ii}^o q_i^2\right) + \sum_{i<j}^N q_i q_j J_{ij}. \tag{2.40}$$

We can now minimize this energy with respect to charge and invoking the electronegativity equalisation principle and a charge totality condition (usually set to zero). We can solve for N simultaneous equations:

$$\chi_i = \frac{\delta E_i}{\delta q_i} = \chi_i^o + J_{ii}^o q_i + \sum_{i<j}^{N} q_j J_{ij}, \tag{2.41}$$

$$C = \sum_{i}^{N} q_i. \tag{2.42}$$

We now have a system whereby the charge of a particle in a system can be calculated from its geometry using only three parameters: electronegativity, self-Coulomb term and the covalent radius. This method can be applied to an interatomic potential so that charge can be calculated at each step of a simulation, allowing each particle's charge to evolve dynamically. This method has been applied to a wide range of materials, including lipid molecules,[43] proteins,[44] solid-state materials[45–47] and hydrocarbons.[48] Using this method, one can parameterize an atomic species so that it can be studied across a range of charge states.

2.4.2 Charge-optimized many-body potential (COMB)

The COMB potential[45] was developed to be able to study Si/SiO_2 systems on a large length and time scale. Many interesting processes occur on a time- and/or length scale that would be far too computationally expensive to calculate using *ab initio* methods and, as discussed above, typical interatomic potentials can not describe an atomic species in its various charge states. The COMB potential allows the charge of the species to vary in order to overcome this problem. COMB is based on the Yasukawa modification to the Tersoff extended potential for Si/SiO_2. The problem with the Tersoff potential is that it assigns static charges, so Yasukawa coupled it with Rappé and Goddard's charge equilibration method to allow each particle's charge to vary over the course of a simulation.[41] Yasukawa's potential[49] was used to study silicon, silica and Si/SiO_2 systems and these studies revealed challenges which the COMB potential aims to overcome:

- The lowest energy state of bulk silicon in the diamond lattice using the Yasukawa potential results in charged Si atoms, i.e. the lowest energy state is not charge neutral. The Si atoms are charged ±3.3 depending on the sublattice they sit in. The charge neutral Si system is actually an energy maximum using this potential.

- The relative stabilities of silica polymorphs do not match experimental data. In particular, α-quartz is not predicted to be the lowest energy polymorph, in contrast to what is known experimentally.[50]

- The Yasukawa potential overestimates the O–Si–O units in the polymorphs α- and β-cristobalite.

Functional Form

The interatomic potential energy in the Yasukawa and COMB potential is calculated as:

$$V_{ij}(\boldsymbol{r}_{ij}, q_i, q_j) = U^R_{ij}(\boldsymbol{r}_{ij}) + U^A_{ij}(\boldsymbol{r}_{ij}, q_i, q_j) + U^I_{ij}(\boldsymbol{r}_{ij}, q_i, q_j) + U^V_{ij}(\boldsymbol{r}_{ij}), \tag{2.43}$$

$$U^R_{ij}(R_{ij}) = f_{s_{ij}} A_{ij} e^{(-\lambda_{ij}\boldsymbol{r}_{ik})}, \tag{2.44}$$

$$U^A_{ij}(\boldsymbol{r}_{ij}, q_i, q_j) = -f_{s_{ij}} b_{ij} B_{ij} e^{(-\alpha_{ij}\boldsymbol{r}_{ij})}, \tag{2.45}$$

$$U^I_{ij}(\boldsymbol{r}_{ij}, q_i, q_j) = \frac{f_{L_{ij}} \eta_i \eta_j q_i q_j}{4\pi\varepsilon_0 \boldsymbol{r}_{ij}}, \tag{2.46}$$

$$U^{VDW}_{ij}(\boldsymbol{r}_{ij}) = \frac{f_{L_{ij}} \left(C_{VDW_i} C_{VDW_j}\right)^{\frac{1}{2}}}{\boldsymbol{r}^6_{ij}}, \tag{2.47}$$

where U^R_{ij} is the repulsive energy, U^A_{ij} is the attractive energy, U^I_{ij} is the ionic bond energy and U^{VDW}_{ij} is the van der Waals energy. The charges used to calculate the attractive and ionic energy are obtained using the charge equilibration scheme. Three-body effects are incorporated into bond-order, b_{ij}, which is used as a weighting factor

when calculating U^A_{ij}:

$$b_{ij} = \left[1 + \left(\beta_i \sum_{k \neq i,j} \zeta_{ijk} g(\theta_{jik})\right)^{n_i}\right]^{-1/2n_i}. \tag{2.48}$$

The parameters used in the COMB potential are derived from experimental data and *ab initio* calculations of α-quartz. The lowest energy silicon structure is charge neutral using these parameters and the relative stabilities of the silica polymorphs match experiment. Lattice constants of α-quartz match experiment but can still be improved for other SiO_2 polymorphs. The COMB potential was designed to be extremely transferable with the ability to study Si/SiO_2 interfaces and has also been parametrised for other elements.[46]

2.4.3 ReaxFF

ReaxFF is another potential that has been developed to study silicon in varying oxidation environments.[51,52] It is an empirical potential whose parameters were determined from B3LYP calculations with a 6-31G** basis set on SiO_x clusters with silicon in varying oxidation states. DFT calculations on crystalline Si and SiO_2 polymorphs were also included in the parameterisation training set. The parameters were optimized using a successive one-parameter search technique.[53] Parameterising to clusters which contain Si in varying oxidation states is meant to include structures which could exist at the interface of an Si/SiO_2 system and which is not represented by either bulk crystalline silicon or silica. ReaxFF describes covalent interactions in terms of a dynamically changing bond order with the charges of each particle determined using the Rappé-Goddard method, allowing the use of classical MD to study the Si/SiO_2 interface.

No connectivities are defined with this potential but instead a bond-order term is calculated which depends on the atoms' geometries. The energy terms depend on the

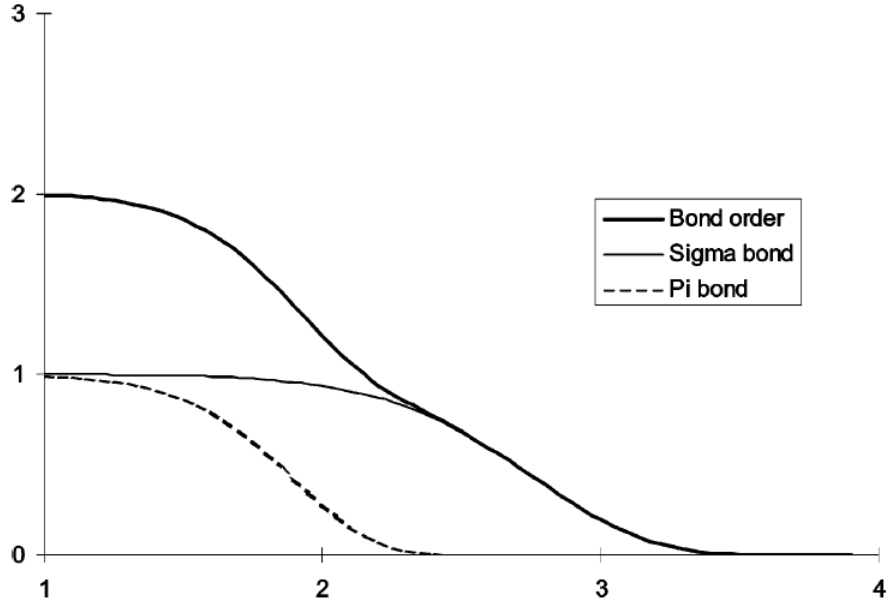

Figure 2.1: Silicon-silicon bond-order dependence on interatomic distance.[51]

bond order which is calculated as:

$$BO'_{ij} = BO'^{\sigma}_{ij} + BO'^{\pi}_{ij} + BO'^{\pi\pi}_{ij},$$

$$= \exp\left[p_{bo,1}\left(\frac{\boldsymbol{r}_{ij}}{\boldsymbol{r}_0^{\sigma}}\right)^{p_{bo,2}}\right] + \exp\left[p_{bo,3}\left(\frac{\boldsymbol{r}_{ij}}{\boldsymbol{r}_0^{\pi}}\right)^{p_{bo,4}}\right] + \exp\left[p_{bo,5}\left(\frac{\boldsymbol{r}_{ij}}{\boldsymbol{r}_0^{\pi\pi}}\right)^{p_{bo,6}}\right], \quad (2.49)$$

where BO'_{ij} is the total bond order, BO'^{σ}_{ij} is the bond order contribution from the σ bonding, BO'^{π}_{ij} is the bond order contribution from π bonding, $BO'^{\pi\pi}_{ij}$ is the bond order contribution from $\pi\pi$ bonding and $p_{bo,x}$ are fitting parameters. Fig. 2.1 shows how the total bond order is affected by the contributions from different bondings, and how the bond order for different bondings varies with interatomic distance.

The energy of the system is split into the following components:

$$E_{System} = E_{Bond} + E_{Over} + E_{Under} + E_{LP} + E_{Val} + E_{Pen} + E_{Tors} + E_{Conj} + E_{VDW} + E_{Coulomb}. \quad (2.50)$$

The interactions ascribed to covalency (e.g. bond-stretching, angles, torsion) contain contributions from σ, π and $\pi - \pi$ bonds. For example, the bond stretching interaction

is described as:

$$E_{bond} = -D_e^{\sigma} BO_{ij}^{\sigma} \exp\left[p_{be,1}\left(1 - (BO_{ij})^{p_{be,2}}\right)\right] - D_e^{\pi} BO_{ij}^{\pi} - D_e^{\pi\pi} BO_{ij}^{\pi\pi}, \tag{2.51}$$

where D_e and p_{be} are fitting parameters. Each bond order has a different dependence on interatomic distance. Describing covalent bond interactions in terms of a bond order (dependent on instantaneous geometry) allows for the dynamic formation and annihilation of bonds. The non-bonding interactions (Coulomb and van der Waals interactions) do not use the bond-order but use the charge calculated using the method developed by Rappé and Goddard.

2.5 Embedded Cluster Method

Both classical potentials and *ab initio* methods were used to model materials throughout this thesis. As mentioned in section 2.4, classical potentials can be used to model a system containing up to a billion atoms. Well parametrised classical potentials are sufficient to provide a good description of the atomistic structure and thermodynamic properties of many materials. On the contrary, DFT can typically model systems containing up to a few thousand atoms. However, it can provide information regarding the electronic structure of the system which is inaccessible with classical potentials. In addition, a charged point defect in a crystalline material is much more difficult to describe using classical potentials due to the distortion they may introduce relative to the ideal lattice to which the potential is usually parameterized.

To study the long range interactions of a point defect in an ideal lattice, it would be useful to be able to use both classical and *ab initio* theories in the same calculation. A system can be divided into two regions, with one described by a quantum mechanical (QM) and the other by a classical description. Methods of this type are generally referred to as quantum mechanical molecular mechanics (QM/MM) methods. The embedded cluster method is a QM/MM method which is particularly suitable for point defects in solid state systems due to approximations which provide correct Madelung

potential variations in the QM region.

The starting point of the embedded cluster method is the creation of a finite nano-sized cluster which describes the material. This nanocluster is divided into two regions - Regions I and II. Region I is located at the centre of the nanocluster and is the region of interest. It may, for example, contain a point defect and its local surroundings. Region I is further subdivided into three regions:

1. A QM region which contains the point of interest and as much of its surroundings as computationally permissible.
2. A region in which all the atoms are described using classical interatomic potentials.
3. An interface region which is sandwiched between the QM and classical region and interacts with them both.

Region II surrounds Region I and is made up of atoms whose position remains fixed and which are described using a classical interatomic potential. Fig. 2.2 shows an example of Region I in the embedded cluster model and highlights the different regions within it. All atoms in Region I are allowed to move in an embedded cluster calculation while atoms in Region II (which are not shown in Fig. 2.2) are static. The function of the atoms in Region II is to ensure that all sites in the region of interest in the QM cluster experience correct Madelung potential variations. This essentially allows for Region I to experience forces as though it were embedded in an infinite crystal, despite the entire system being finite.

To allow the QM region to interact with the classically polarizable region, an interface region is defined between them as a set of pseudoatoms which bind both regions. In the case of a mixed ionic-covalent material (such as SiO_2: the main focus of this thesis), the pseudoatom is described by a single electron and a short-range repulsive potential which are both parameterized to provide a good approximation for the interatomic interactions in an ideal lattice. The pseudoatom also interacts with the classically polarizable region. This interaction is described as a sum of Coulomb

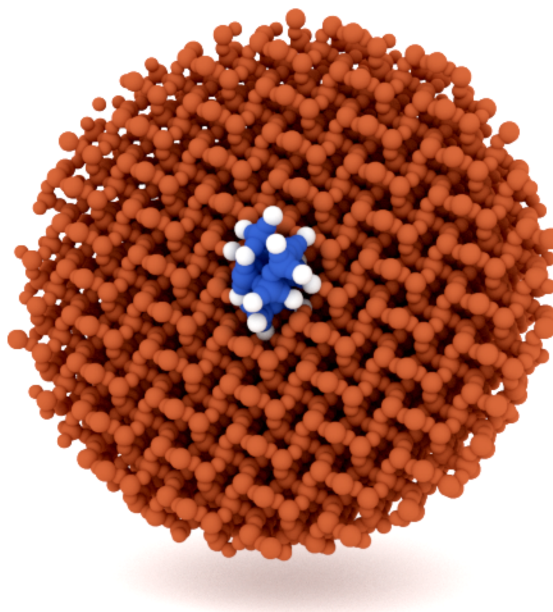

Figure 2.2: A cross-section through an example of Region I in an embedded cluster model containing both QM and classical atoms. The quantum cluster atoms are highlighted in blue, the pseudoatom interface atoms are highlighted in white while the classical atoms are highlighted in red. The quantum cluster is embedded into the classical region and all atoms in Region I are allowed to relax.

and short-range classical Morse interactions. The interactions between atoms in the classical region and atoms in the QM region are included as Coulomb terms in the Hamiltonian of the QM region. The total energy of the system is given as:

$$E_{Total} = E_{QM} + E_{Cl}, \tag{2.52}$$

where E_{QM} and E_{Cl} are the energies of the QM and classical region respectively. E_{QM} is given as:

$$E_{QM} = \langle\psi|\hat{H}_0 + V_{env}^{Coul}|\psi\rangle + V_{env}^{Short}, \tag{2.53}$$

where $\hat{H}_0$ is the Hamiltonian of the QM cluster only, V_{env}^{Short} is the short range interaction between the classical and QM atoms, and V_{env}^{Coul} is the external potential which

includes interactions between the classical cores and shells with the QM atoms:

$$V_{env}^{Coul} = \sum_{i}^{N_{core}} \left(\sum_{j}^{n} \frac{q_i^{core}}{|r_i^{core} - r_j|} + \sum_{j}^{N_{QM}} \frac{q_i^{core} Z_j^{QM}}{|r_i^{core} - r_j^{QM}|} \right) + \sum_{i}^{N_{shell}} \left(\sum_{j}^{n} \frac{q_i^{shell}}{|r_i^{shell} - r_j|} + \sum_{j}^{N_{QM}} \frac{q_i^{shell} Z_j^{QM}}{|r_i^{shell} - r_j^{QM}|} \right),$$

where n and N_{QM} are the numbers of electrons and QM atoms in the QM region; N_{core} and N_{shell} are the numbers of cores and shells in the classically polarizable region; Z, q^{core} and q^{shell} are the charges of the QM nuclei, the classically polarizable cores and the classically polarizable shells, respectively. This total energy can be minimised to obtain the ground state structure of the system in the embedded cluster method.

2.6 Nudged Elastic Band Method

The activation energy of a reaction is an extremely important parameter in the context of chemical dynamics, allowing accurate predictions of the rate of a reaction. The concept of an activation energy stems from the Arrhenius equation and is essentially the energy required in order for a reaction to proceed. The Arrhenius equation can be written as:

$$k_{ab} = Ae^{-\frac{E_A}{K_B T}}, \tag{2.54}$$

where k_{ab} is the rate of the reaction, E_A is the activation energy, and $K_B T$ is the Boltzmann constant scaled by temperature. Further research led to the development of harmonic transition state theory, in which the activation energy also plays a central role.[54] For these reasons, there has been a large research effort into methods that can provide minimum energy pathways (MEP) of a reaction from which the activation energy can be extracted. A MEP is the trajectory between reactants and products that follows the lowest energy along the potential energy surface between them. The activation energy(ies) can be determined from the MEP as the first order saddle points (there may be more than one activation energy) along the MEP.

A method that has been used to successfully calculate MEPs for many reactions in various materials is the climbing image nudged elastic band method (CI-NEB). Although a number of methods are available in the literature for the calculation of MEPs, such as the linear synchrous transit method[55] and eigenvector following methods,[56] the use of CI-NEB is advantageous as it is a highly transferable method applicable to many reactions in a wide range of materials. Compared to other methods, it is known to provide a good prediction for the MEP as well as the saddle point which other methods struggle with. However, CI-NEB requires that the initial and final states are known *a priori*, which can be troublesome when researching new and complex multi-step reactions. One also has to be aware that CI-NEB finds the 'local' MEP; there may be a lower energy pathway that is inaccessible due to the choice of initial pathway. The following is a brief overview of CI-NEB which has been used throughout this thesis to extract reaction pathways and their activation energies.

The starting point for CI-NEB is the plain elastic band method (PEB), where several images between an initial and a final state are connected by springs forming a band whose energy can be optimised to provide the MEP. The images can be tentatively constructed using a linear interpolation between the initial and final states. However, one has to be careful that the linear interpolation could create a path that is far from the MEP, e.g. the substitution of two lattice sites where atoms would overlap in some of the image configurations causing unphysically high energies. A set of springs is then connected between the images, and the force felt by each image is thus:

$$F_i^{PEB} = F_i + F_{spring,i}, \tag{2.55}$$

where F_i is the force due to the potential energies of each configuration, and $F_{spring,i}$ is the force due to the springs:

$$F_{spring,i} = k_{i+1}(\mathbf{r}_{i+1} - \mathbf{r}_i)^2 + k_i(\mathbf{r}_i - \mathbf{r}_{i-1})^2. \tag{2.56}$$

After creating the images and connecting them with springs, an objective function

can then be defined as:

$$S(\mathbf{r}_1, \mathbf{r}_2, \dots) = \sum_{i=0}^{P} V(\mathbf{r}_i) + \sum_{i=1}^{P} \frac{k}{2}(\mathbf{r}_i - \mathbf{r}_{i-1})^2, \tag{2.57}$$

where the first term is a sum of the potential energies of each of the images and the second term is a sum of the potential energies caused by the springs connecting the images. One can then use a suitable algorithm to minimize the objective function in equation 2.57 with respect to the atomic coordinates of the images, thus minimising the energy of the band and leading to an optimised path between the initial and final configurations.

The PEB method suffers from two salient shortcomings: 1) the optimised band can cut corners and; 2) the images can slide down the band leading to an uneven spacing between them. These shortcomings are due to the image spring forces that are not aligned along the direction of the band and the potential forces that do not act perpendicular to the direction of the band.

The nudged elastic band method (NEB) attempts to fix the shortcomings in the PEB method by only using the spring force components parallel to the band and potential force components perpendicular to the band. These corrections 'nudge' the band onto the true MEP. The force felt by each image on a NEB pathway is:

$$F_i^{NEB} = F_i^{\perp} + F_{spring,i}^{\|}, \tag{2.58}$$

where the first term is the potential force component perpendicular to the direction of the band and the second term is the spring force component parallel to the direction of the band. They can be obtained trivially during the calculation as:

$$F_i^{\perp} = -V(\mathbf{r}_i) + V(\mathbf{r}_i) \cdot \hat{\tau}_i \hat{\tau}_i, \tag{2.59}$$

$$F_{spring,i}^{\|} = (k_{i+1}(|\mathbf{r}_{i+1} - \mathbf{r}_i|) + k_i(|\mathbf{r}_i - \mathbf{r}_{i-1}|)) \cdot \hat{\tau}_i, \tag{2.60}$$

where τ_i is the direction of the band at image i and k is the force constant of the

spring. Instead of using the objective function introduced for the PEB method, the NEB method finds the MEP by minimising F^{NEB} directly.

However, the activation energy obtained from the NEB MEP may be smaller than the true value, as the springs will pull the highest energy images down toward a lower energy. This issue can be fixed by removing the springs connecting the highest energy image, and inverting the force felt by the atoms in this image to push the image onto the saddle point:

$$F^{CI}_{highest} = F_{highest} - 2f_{highest} \cdot \hat{\tau}_{highest}\hat{\tau}_{highest}. \tag{2.61}$$

This manipulation allows the highest energy image to be pushed up the potential energy surface to find the true first order saddle point, providing a more accurate estimation of the activation energy. This correction combined with NEB is known as climbing image nudged elastic band (CI-NEB). This method has been used throughout this thesis to obtain accurate estimates of the activation energies of various reactions.

3

Modelling Amorphous Silicon Dioxide and the Si/SiO_2 interface

3.1 Introduction

The ubiquity and technological importance of a-SiO_2 has led to a huge experimental and theoretical research effort to understand its atomic structure over the decades. It is all too easy to forget that almost nothing was known about the atomistic nature of amorphous solids until just under a century ago, with competing theories proposing that amorphous solids were either supercooled liquids or composed of solid crystallites. (Ultimately, amorphous materials were shown to not flow, definitively determining that they are solids.[57]) Initial X-ray diffraction (XRD) studies showed

that amorphous solids do not exhibit the sharp, intense spots which are characteristic of a crystal, instead displaying a diffuse signal over the entire pattern, leading researchers to propose that the underlying solid is made up of crystallites; in particular, cristoballite crystallites in the case of a-SiO_2. A revolutionary advance in our understanding of the atomic nature of amorphous solids came with the introduction of the continuous random network model (CRN) by Zachariasen in 1932.[58] He ruled out crystallite theory by comparing the mechanical strengths of a-SiO_2 and its crystalline analogues, arguing that their similarities indicate that the interatomic forces holding a-SiO_2 should be similar to those holding together crystalline SiO_2 (c-SiO_2). He then defined a-SiO_2 as a 3D structure with a lack of symmetry and containing similar bonding to c-SiO_2. XRD studies of the atomic structures of the c-SiO_2 variants reveal that they are made up of SiO_4 tetrahedra. It then follows that one expects a-SiO_2 to be made up of SiO_4 tetrahedra. Thus, Zachariasen proposed that the structure of a-SiO_2 is made up of corner-sharing SiO_4 tetrahedra with a varying intertetrahedral angle, as shown in Fig. 3.1.

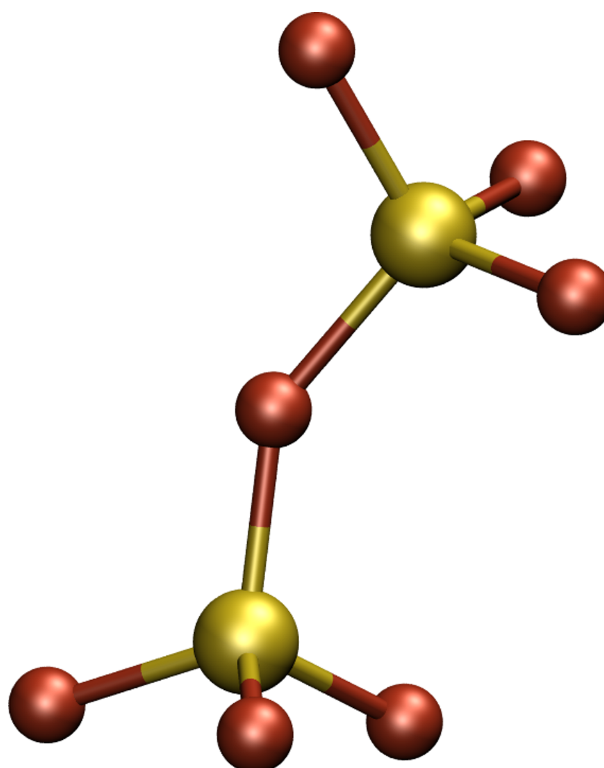

Figure 3.1: Two interlinked SiO_4 units illustrating the flexible Si-O-Si angle. Si atoms are coloured in yellow while O atoms are coloured red.

The main focus of this thesis concerns the properties of charge trapping defects in amorphous SiO_2. In order to be confident that the results of the calculations will be truly representative of the properties of defects in a-SiO_2, the initial a-SiO_2 model must be consistent with our experimental perceptions of the atomic structure of a-SiO_2 discussed above. This chapter discusses the techniques used to model and characterise the atomic structures of a-SiO_2 studied in this thesis. Models of a-SiO_2 were created using classical potentials and a melt-quench technique, similar to what has been reported in the literature.[38,59] However, the choice of potential was constrained to charge variable potentials in order to be able to model Si in varying oxidation states. This would, in principle, allow for the modelling of an Si/SiO_2 system and the creation of point defects. The first part of this chapter discusses the choice of interatomic potential to be used in the modelling of a-SiO_2 structures. This is followed by a technical discussion of the melt-quench method used to generate a-SiO_2 and the methods used to characterise the a-SiO_2 models generated. Finally, this chapter concludes by modifying and extending the melt-quench method to model Si/SiO_2 systems and characterise their structures in a similar manner to the a-SiO_2 structures generated using the melt-quench method.

3.2 Choosing the Classical Potential

To create models of a-SiO_2, we will be using molecular dynamics simulations. This requires a choice of potential which can accurately describe its structure. The classical potentials considered for modelling bulk a-SiO_2 and the Si/SiO_2 interface are ReaxFF[51] and COMB.[45] To model both these systems accurately, the potential must be able to reproduce the structures of Si, SiO_2, and the intermediate states which can exist at the interface. In order to choose the potential, a library of test clusters containing Si in varying oxidation states was chosen whose structures have been studied experimentally or at higher levels of theory than classical potentials. Both ReaxFF and COMB were then used to optimize the structures of these small silica-

like clusters so that they can be evaluated against the literature. The clusters test both ReaxFF and COMB's ability to reproduce the structure of a cluster containing Si in an intermediate oxidation state.

3.2.1 Small Silicon and Silica Test Clusters

Wang *et al.* studied molecules of Si_3O_y (y=1-6) as structures representative of those which may exist during the oxidation of silicon,[60] representing the sequential oxidation of Si_3. The clusters were studied using photoelectron spectroscopy and *ab initio* calculations. Geometry optimizations were performed at the Hartree-Fock level using a 6-31G* basis set. The resulting geometries were further optimised using second order Møller-Plesset perturbation theory and a 6-311G* basis set. For y=1-3, each additional oxygen atom bridge bonds between a Si–Si bond, producing cyclic structures (see Fig. 3.2). For y=4-6 the cluster begins to adopt a tetrahedral structure with a central Si atom bonded to four oxygen atoms.

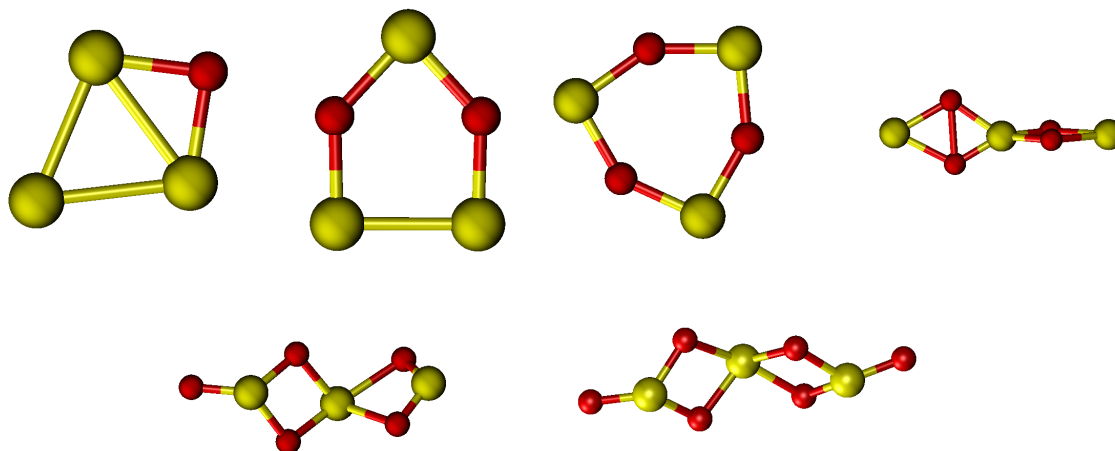

Figure 3.2: Atomic structures of Si_3O_y clusters as reported by Wang *et al.*[60] From left to right and top to bottom, y=1-6.

To test the abilities of ReaxFF and COMB to model intermediate oxidation states of Si, these clusters were optimized using each potential as implemented in the LAMMPS code[61] and compared to Wang's results.[60] Starting from their ideal structures according to the study by Wang, the Si_3O_y clusters were optimized using the ReaxFF and COMB potentials with a conjugate gradient optimiser. The bond

lengths obtained with both potentials are in very good agreement with the results obtained by Wang, as can be seen in table 3.1. Both potentials have a minimum associated with these clusters apart from Si_3O_6, for which the COMB potential was not able to find one. Instead, the central Si is bonded to three oxygens instead of four and the terminal Si is bonded to two oxygens as seen in Fig. 3.3 . This clearly does not match the structure in Fig. 3.2. These results give an early indication that the COMB potential does not provide the right potential energy surface for a Si/SiO_2 interface model.

	Wang paper[60]	ReaxFF	COMB
Si_3O			
Si-Si	2.30	2.32	2.46
Si-O	1.75	1.69	1.72
Si_3O_2			
Si-Si	2.41	2.16	2.15
Si-O (1)	1.67	1.66	1.81
Si-O (2)	1.67	1.67	1.65
Si_3O_3			
Si-O	1.69	1.66	1.73
Si_3O_4			
Si-O (1)	1.72	1.76	1.63
Si-O (2)	1.67	1.62	1.70
Si_3O_5			
Si-O (1)	1.52	1.45	1.47
Si-O (2)	1.67	1.60	1.66
Si-O (3)	1.68	1.68	1.60
Si-O (4)	1.66	1.77	1.73
Si-O (5)	1.73	1.60	1.50
Si_3O_6			
Si-O (1)	1.53	1.46	N/A
Si-O (2)	1.69	1.56	N/A
Si-O (3)	1.68	1.76	N/A
All bond lengths are in Å			

Table 3.1: Bond lengths of the Si_3O_y clusters optimised using COMB and ReaxFF and compared to the results by Wang *et al.*[60]

The electronic and structural properties of neutral and charged Si_nO_n clusters with n=3-5 were calculated using DFT within the local density approximation by Chelikowsky *et al.*[62] These small silica-like clusters were investigated to extract bond stretching and angle bending forces. The pseudopotential was tested against previous

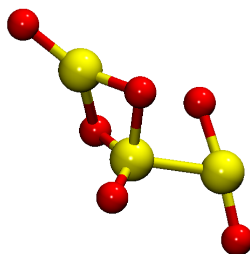

Figure 3.3: Atomic structures of Si_3O_6 optimized using COMB.

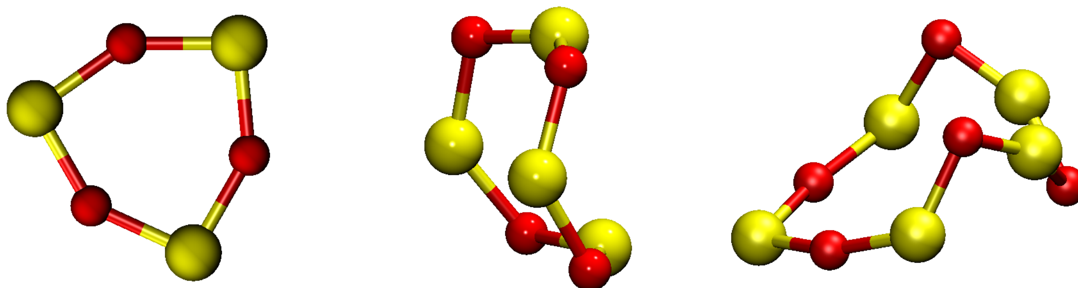

Figure 3.4: Atomic structures of Si_nO_n clusters studied by Chelikowsky *et al.*[62]

theoretical work, agreeing closely with previous results in the literature despite a systematic underestimation of the Si–O bond length. The geometry of the Si_3O_3 cluster agrees with the planar ring structure calculated by Wang,[60] but the geometries of the Si_4O_4 and Si_5O_5 resemble a buckled ring, seen in Fig. 3.4.

	Chelikowsky paper[62]	ReaxFF	COMB
Si_4O_4			
Si–O	1.65	1.63	1.65
Si–O–Si	127	158.2	111.5
O–Si–O	104	109.7	131.63
Si_5O_5			
Si–O (1)	1.65	1.54	1.65
Si–O (2)	1.65	1.62	1.73
Si–O–Si	122	149.9	123.5
O–Si–O	104	93.9	119.9
All bond lengths given in Å; Bond angles in °.			

Table 3.2: Si_nO_n clusters optimised using COMB and ReaxFF.

Table 3.2 shows that the Si–O bond lengths of the Si_4O_4 cluster calculated with both ReaxFF and COMB are in reasonable agreement with Chelikowsky's results. However, the bond angles are not reproduced correctly using these potentials. The same conclusion can be drawn from the results of the Si_5O_5 cluster; the bond lengths

seem to be reproduced satisfactorily whereas the bond angles are not reproduced as accurately. This leads one to believe that should one of these potentials be used to model the interface, the structures which may exist at the interface may not be reproduced with the correct bond angle. However, it is clear that these structures are qualitatively reproducible with both potentials and that potential energy minimas exist for these structures.

Chelikowsky *et al.* also studied the structure of small Si clusters (Si_n: n=2-6) using the same DFT method.[63] They were obtained from a random atomic configuration at an initial temperature of 3000 K, followed by an anneal down to 300 K. The final structure is obtained from a steepest-descent optimization of the geometry obtained at 300 K. The ReaxFF and COMB clusters both optimize to the same qualitative

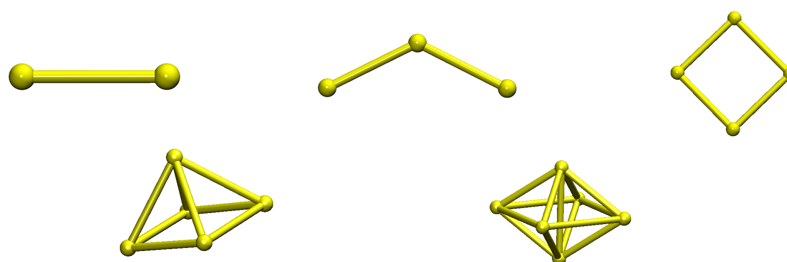

Figure 3.5: Atomic structures of Si_n clusters, where n=2-6.

structure. As can be seen in table 3.3, both potentials generally overestimate the Si–Si bond lengths and seem to have trouble describing the bond angle in Si_3, but other than that they both have a similar description of small Si clusters.

Summary

This library of small Si and SiO_x clusters show that both ReaxFF and COMB can describe Si in intermediate oxidation states reasonably well. Potential energy minima exist for almost all the clusters studied with Si in varying oxidation states. From these calculations, it is proposed that adopting a scheme where these structures may be obtained using a charge variable force-field followed by a further optimization performed at a higher level of theory would lead to quantitatively accurate geometries for structures which exist at the interface. As both potentials have performed similarly

in describing these small clusters, further investigation is needed so as to choose the force-field to model the Si/SiO_2 interface.

	Chelikowsky paper[63]	ReaxFF	COMB
Si_2			
Si-Si	2.23	2.14	2.30
Si_3			
Si-Si	2.16	2.20	2.28
Si-Si-Si	80	60	128
Si_4			
Si-Si (1)	2.31	2.23	2.37
Si-Si (2)	2.40	2.42	3.36
Si_5			
Si-Si (1)	2.28	2.40	2.55
Si-Si (2)	3.04	3.40	3.59
Si_6			
Si-Si (1)	2.35	2.44	2.43
Si-Si (2)	2.71	2.44	2.80
All bond lengths are given in Å			

Table 3.3: Si_n clusters optimised using COMB and ReaxFF.

3.2.2 NVE Molecular Dynamics using ReaxFF and COMB

The chosen potential will be used in molecular dynamics simulations. Thus, the implementation of the potential in the LAMMPS code was investigated by running NVE molecular dynamics. An NVE simulation fixes the number of atoms, the volume and the total energy of the system. These preliminary simulations were also used to adjust the time step to be used in further simulations.

Using the LAMMPS code, both potentials are used to run an NVE molecular dynamics simulation on a 2x2x2 periodic supercell of β-cristobalite. The simulation is run for 5 ps and the charge on each particle is calculated at every time-step. Total energies calculated in an NVE simulation fluctuate, which is to be expected from using numerical integration techniques for the evolution of the atoms' motions. However, on closer inspection of the COMB total energy graph, there appear to be discontinuities at certain time-steps, as illustrated in Fig. 3.6a. These discontinuities do not exist in the ReaxFF total energy curve. Upon further analysis it was found that these

discontinuities stem entirely from the potential energy component of the total energy, appearing at the same time step and with the same energy difference. The kinetic energy does not suffer from this discontinuity. The charges calculated by COMB were analysed and were shown to suffer a similar discontinuity at the same time step as the energy discontinuities, shown in Fig. 3.6b. Analysis of the trajectory at the time steps associated with these discontinuities shows a movement of oxygen atoms across a boundary into the adjacent image. The implementation of the COMB potential in the LAMMPS code has trouble dealing with periodic boundary conditions, leading to discontinuities in charge which are the cause of the discontinuity in the total and potential energy discontinuities. The ReaxFF implementation in LAMMPS does not suffer from this problem. Due to ReaxFF's ability to describe the silica and silicon clusters and its proper implementation in LAMMPS, it was decided that the ReaxFF potential would be used as the potential to construct models of a-SiO$_2$ and the Si/SiO$_2$ interface.

Due to the use of the Verlet algorithm in molecular dynamics, the total energy in an NVE simulation fluctuates, as mentioned earlier. This is a well known issue associated with the truncation of the Taylor expansion of the positions which introduces an error in their calculation.[64] This truncation manifests itself as fluctuations in the total energy and is dependent on the time step used in the simulation: the larger the time step chosen, the greater the fluctuation. Choosing the time step is a trade-off between minimising the total energy fluctuation and being able to achieve the desired time of simulation. The root mean square fluctuation (RMSF) is a measure of the deviation of the total energy against the average total energy and is calculated according to equation 3.1. A generally accepted value for the RMSF limit is one part in ten thousand.[65] The RMSF was calculated as:

$$RMSF = \frac{1}{T}\sum_{t=1}^{T}(E(t) - \bar{E})^2, \tag{3.1}$$

where T is the time of the simulation, $E(t)$ is the total energy at time t and $\bar{E}$ is the average total energy. Two MD simulations were performed under NVE conditions

Figure 3.6: a) Total energy and b) Average charges of the Si (black crosses, left hand side axis) and O atoms (red crosses, right hand side axis), all plotted against time step and extracted from the same NVE molecular dynamics simulation using the COMB potential. Both the total energy and the average charges show discontinuities at the same time step.

for a 2x2x2 periodic supercell of β-cristobalite using the ReaxFF force field for 50 ps each. The only difference between the two simulations was the time step chosen; one simulation was run using a time step of 0.5 fs, the other was run using a time step of 0.1 fs. The RMSF for the 0.5 fs time step was 10.77×10^{-3} while it was 3.05×10^{-4} for the 0.1 fs time step. The RMSF value for the 0.5 fs time step is an order of magnitude larger than the generally accepted limit while it is a little larger for the 0.1 fs. A time step smaller than 0.1 fs would greatly increase simulation times making it infeasible to choose a smaller time step. A trade off has to be made between accuracy and computational cost, therefore the time step that will be used in the molecular dynamics simulations in this thesis is 0.1 fs.

3.2.3 Summary

Short molecular dynamics simulations were run to assess the computational stability of the charge equilibrating potentials ReaxFF and COMB. The COMB potential was found to show discontinuities in the species' calculated charges which causes discontinuities in the potential energy surface. In contrast, the ReaxFF potential showed no discontinuities and was found to be stable for use in MD simulations. In addition, a time step for the MD simulations was chosen for the remainder of this thesis based on convergence of the root mean squared fluctuation below 0.0001. Thus the potential that is used to model a-SiO_2 throughout this thesis is the ReaxFF potential.

3.3 Making Amorphous Silica Models

Amorphous silica is a metastable state of SiO_2 which is defined by its disorder and lack of well defined long-range geometrical properties. It is made up of SiO_4 interlinked tetrahedra with a flexible Si-O-Si angle. The same interatomic forces that act on crystalline polymorphs of silica act on a-SiO_2, leading to a material with a fairly well defined short-range but lack of long-range order.

The short range order of a-SiO_2 results in a number of geometrical properties being described by a statistical distribution, as opposed to the discrete values found in its crystalline analogues. As the SiO_4 unit maintains its tetrahedral shape, the O-Si-O angle has a sharp peak around 109.5°. The Si-O bond length also forms a sharp peak at around 1.6 Å. The Si-O-Si angle is quite flexible, leading to a rather broad distribution, between 120° and 180°, with the most frequent value occurring at 148°.[66,67]

Amorphous silica is made experimentally by melting a crystalline polymorph of silica followed by a rapid cooling known as a quench. Molecular dynamics can simulate this process, albeit with much faster quenching rates, and has previously been used to investigate a-SiO_2 using various interatomic potentials as discussed in the introduction of this chapter.[59,68,69] In this section, the ReaxFF potential was used to model amorphous silica within this general scheme which shall be referred to as the melt-and-quench method. Starting from β-cristobalite, a crystalline polymorph of SiO_2, a thermostat will be applied to raise the temperature of the system to form a liquid melt which will then be rapidly cooled down to form an amorphous silica model. The resulting structures are then characterised and compared to experiment. All the structures are then further optimised at the DFT level using the CP2K code. The electronic structures of the models are extracted and analysed to understand the electronic properties of a-SiO_2.

3.3.1 Modelling a-SiO_2 using the ReaxFF potential and the Melt-and-Quench Method

The silica polymorph chosen to melt and quench was β-cristobalite. It was chosen for its density (2.33 g cm^{-3}), which is the closest of the silica polymorphs to the average amorphous silica density of 2.2 g cm^{-3} and due to its cubic cell shape. A Berendsen thermostat and barostat was applied to a periodic supercell of β-cristobalite containing 216 atoms. A time constant has to be chosen for the thermostat and barostat. Initially, a number of NVT (constant number of atoms, volume and temperature)

simulations were run on β-cristobalite at 300 K for 50 ps to adjust the time constants of the Berendsen thermostat so that the temperature oscillated within 3% of its desired value and so that the system was able to equilibrate within a few hundred time steps. The time constant for the Berendsen barostat was adjusted in a similar manner, by fixing the pressure at 1.0 bar and running a number of simulations using different time constants. The time constant chosen for the Berendsen barostat was the smallest value which did not cause large fluctuations in volume. These criteria led to a time constant of 5 fs^{-1} for the thermostat and 1000.0 fs^{-1} for the barostat.

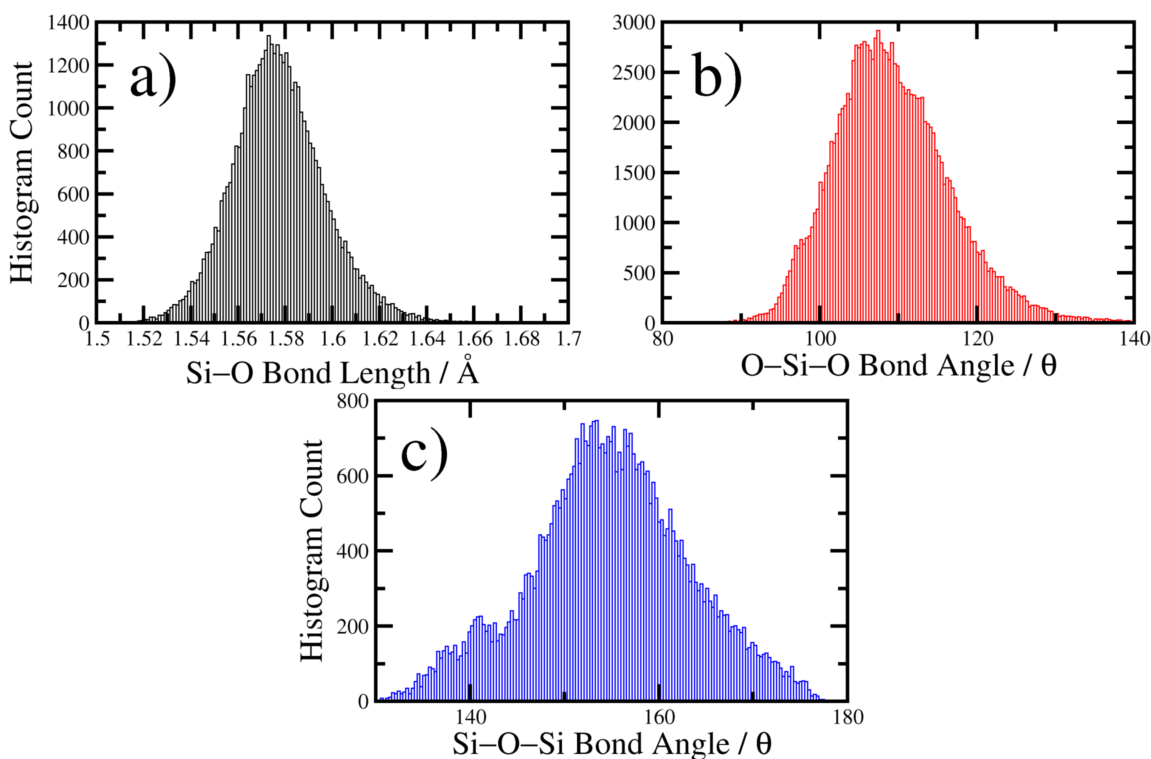

Figure 3.7: Histograms of the short-range geometrical properties of a-SiO$_2$ from 320 a-SiO$_2$ models generated using the ReaxFF potential and the melt and quench method. a) Si–O bond lengths. b) O–Si–O bond angles. c) Si–O–Si bond angles.

With the time step and the thermo- and baro-stat's time constants chosen, simulations were then performed to heat the system up. Initially, each particle in the 216 atom system of β-cristobalite was assigned a random velocity from a Gaussian distribution centred around 300 K and with a constraint that the sum of all velocities result in the system's temperature being 300 K. With the temperature maintained at 300 K and the pressure at 1 bar, a simulation was run for 20 ps to equilibrate the

system. The temperature of the system was then linearly increased to 5000 K over 200 ps. By analysing the gradient of the potential energy curve as the temperature increased and finding the point where the gradient changes, the melting point can be identified. This is because bonds are broken as the material melts point which increases the rate of potential energy change. The melting temperature was found at 4500 K and by 5000 K the system was found to be a liquid. The system was maintained at 5000 K for 1 ns, then cooled down at a rate of 6 K ps^{-1} to 0 K. The cooling rate was chosen as the studies by Vollmayr *et al.* suggest that the positions of the peaks in the short-range geometrical properties of the amorphous structure converge at a cooling rate of 8 K ps^{-1}.[68] To study the geometrical statistics of a-SiO_2 generated using this procedure, 320 models were generated and the resulting structures were then optimised and analysed.

The average density of the a-SiO_2 samples obtained were 2.16 g cm^{-3} and ranges from 1.99 to 2.27 g cm^{-3}, which is in excellent agreement with experiment (2.2 g cm^{-3}).[70] The mean Si–O bond length is 1.58 Å, slightly shorter than the experimental value of 1.61 Å.[67] The average Si-O-Si angle obtained was 154.75° which is slightly larger than the experimental value of 148.3°. The O-Si-O angle obtained is 109.30°, which is in excellent agreement with the experimental value of 109.47°. The graphs shown in Fig. 3.7 demonstrate the lack of order in the systems and shows the distribution of bond lengths and angles, as opposed to the sharp peaks which are characteristic of ordered crystalline systems. Interestingly, the extracted distributions display a normal distribution.

Although it is useful and intuitive to characterise amorphous structures in terms of their short-range geometrical properties, there are no experimental data available against which one could directly compare. Unlike crystalline materials, the bond lengths cannot be directly extracted by means of X-ray or neutron diffraction experiments. This is due to the crystalline structure being interpreted using Bragg's law, which is entirely inappropriate for amorphous solids. Instead of the characteristic bright spots, shown in Fig. 3.8a, and halos seen in X-ray and powder X-ray diffrac-

(a)

(b)

Figure 3.8: Real space representation and spatial frequencies of crystalline and amorphous solids. a) The left image shows the atomic structure and electron density of α-quartz and the right image shows the electron density's Fourier transform. The periodicity is obvious in real space and is reflected as ordered, discrete spatial frequencies in the right image. b) The left image shows the atomic structure and electron density of an a-SiO_2 model, while the right image is the electron density's spatial Fourier transform. The real space structure is disordered, although it is ordered at short-range. As a result, its Fourier transform shows no obvious order.

tion experiments on crystalline materials, the diffraction pattern of an amorphous solid consists of a bunch of diffuse halos, similar to extracting a plane from Fig. 3.8b. Information on the structure of an amorphous solid can still be extracted from X-ray and neutron diffraction experiments by measuring what is known as the structure factor, which is defined as:[71]

$$S(Q) = \frac{1}{N}\sum_{j,k} b_j b_k \langle e^{iQ[\mathbf{r}_j - \mathbf{r}_k]}\rangle, \tag{3.2}$$

where S is the structure factor, Q is the scattering vector, b_j and b_k are the scattering lengths (X-ray of neutron) while $\mathbf{r}_j$ and $\mathbf{r}_k$ are the atomic coordinates of atoms j and k. Assuming that the material is isotropic, which is normally valid for amorphous materials, the vector $[\mathbf{r}_j - \mathbf{r}_k]$ can take on any orientation with respect to the scattering vector. Therefore it is necessary to sum over all orientations in order to obtain the orientational average:

$$\langle e^{iQ[\mathbf{r}_j - \mathbf{r}_k]}\rangle = \frac{1}{4\pi[\mathbf{r}_j - \mathbf{r}_k]^2}\int_{\phi=0}^{\pi} e^{(iQ[\mathbf{r}_j - \mathbf{r}_k]\cos\phi)2\pi[\mathbf{r}_j - \mathbf{r}_k]^2 sin\phi d\phi} = \frac{\sin Q[\mathbf{r}_j - \mathbf{r}_k]}{Q[\mathbf{r}_j - \mathbf{r}_k]}, \tag{3.3}$$

so that:

$$S(Q) = \frac{1}{N}\sum_{j,k} b_j b_k \frac{\sin Q[\mathbf{r}_j - \mathbf{r}_k]}{Q[\mathbf{r}_j - \mathbf{r}_k]}. \tag{3.4}$$

Thus, the structure factor can be efficiently extracted from the atomic coordinates of a calculation. It can also be obtained from X-ray and neutron diffraction experiments, as it is related to diffraction as:

$$S(Q) = \frac{I(Q)}{Nf^2}, \tag{3.5}$$

where I is the intensity of diffraction, N is the number of atoms and f is the total atomic scattering factor. The structure factor is a 1-dimensional representation of the 3-dimensional amorphous structure, providing information on the short-, medium- and long-range order. Fig. 3.9 shows the average total neutron structure factor calculated from 320 a-SiO$_2$ models which were made using the ReaxFF potential as well as an experimentally measured signal.[72] The structure factor of the ReaxFF models agrees very well with the experimental data, showing the same number of peaks despite a few of the peaks being shifted slightly. The peaks agree well even at large Q values, indicating that the medium- and long-range order of the models matches that of experiment. These results indicate that the melt-and-quench method

using the ReaxFF potential provides a-SiO_2 models which are representative of the experimental samples.

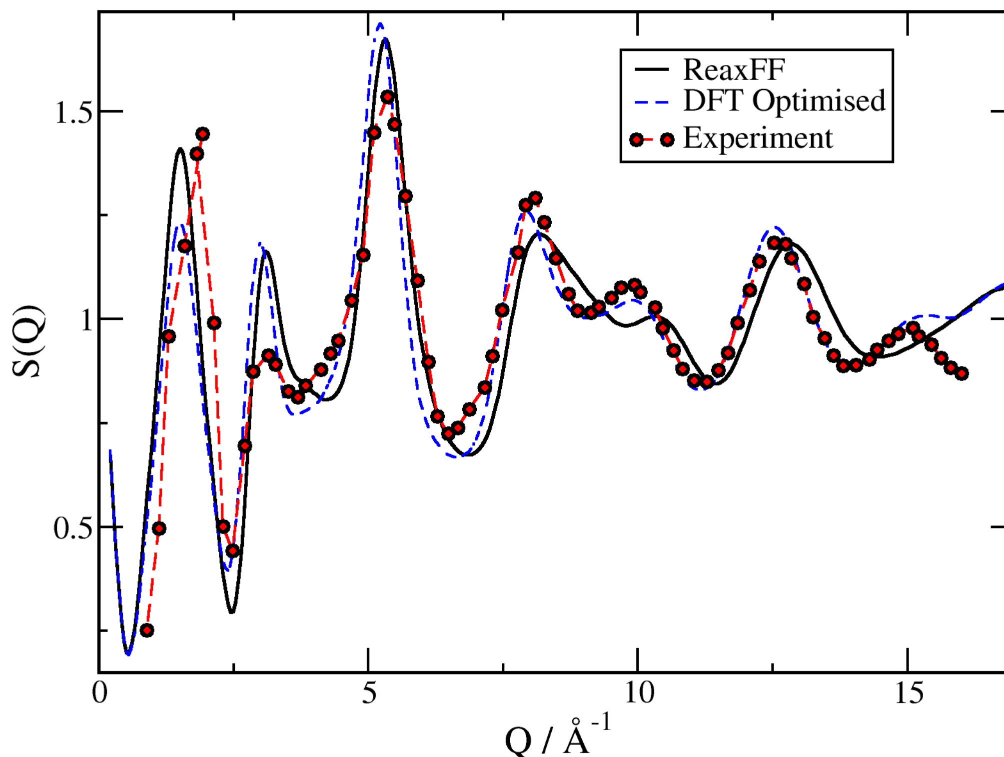

Figure 3.9: Total neutron structure factors from ReaxFF a-SiO_2 models, before and after DFT optimisation, and from neutron scattering experiments. The solid black line shows the average total structure factor of a-SiO_2 from 320 models made using ReaxFF and the melt and quench method. The dashed blue line is the average total structure factor of these ReaxFF models after they have been optimised using DFT. The red circles are experimentally measured data.[72]

3.3.2 DFT Optimisation of ReaxFF Structures

After obtaining the a-SiO_2 structures using ReaxFF, they were optimised further and their electronic structures were extracted using DFT as described in chapter 2.3. To describe exchange and correlation, the non-local PBE0_TC_LRC functional[34] was used along with the auxiliary density matrix method.[73] This functional uses a truncated Coulomb operator to calculate the Hartree energy for which a truncation radius of 2.0 Å was used. This functional was used as it contains a portion of Hartree-Fock exchange which improves the description of the band gap as well as describing localised states better than traditional local and gradient-corrected density approximations. Using

the Gaussian Plane waves method, the Gaussian basis set used was a double-ζ basis set with polarisation functions for both the Si and O atoms, while the plane wave basis set was truncated at 5440 eV (400 Ry). All of the systems were optimised individually using the Broyden-Fletcher-Goldfarb-Shanno (BFGS) algorithm. The structures were considered optimised when the forces on the atoms were converged to within 37×10^{-12} N (2.3×10^{-2} eV Å^{-1}).

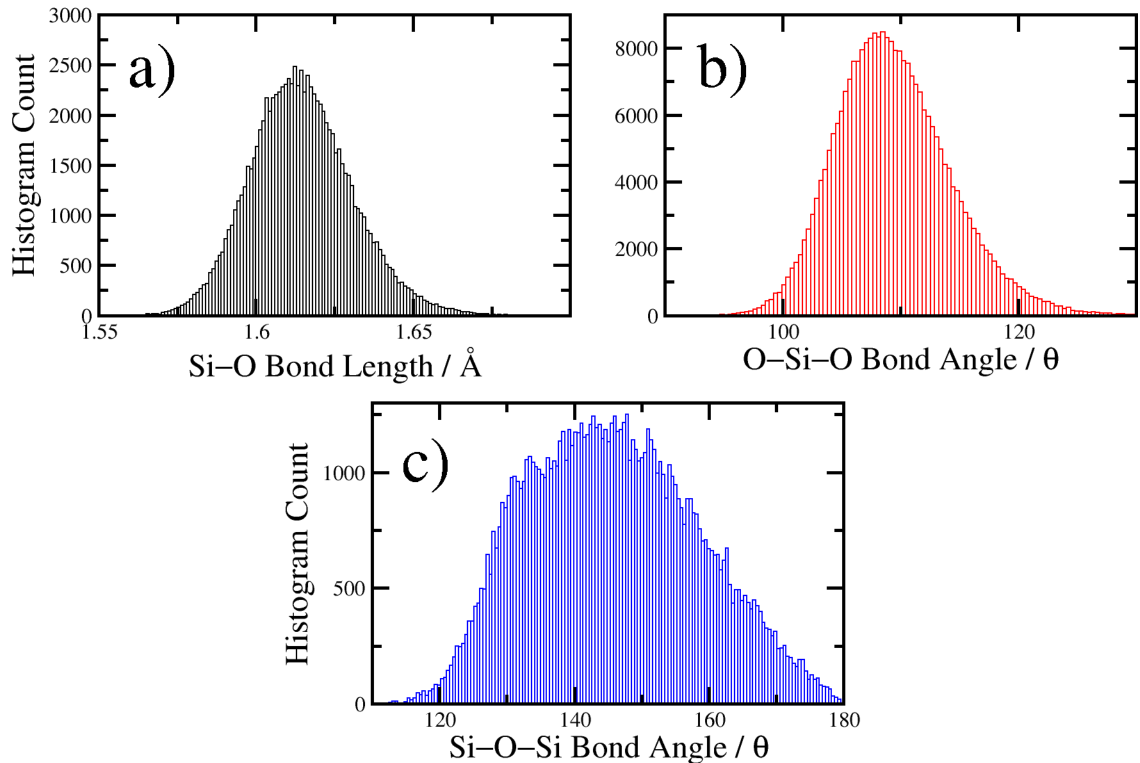

Figure 3.10: Histograms of the short-range geometrical properties of 320 DFT optimised models of a-SiO_2. a) Si–O bond lengths. b) O–Si–O bond angles. c) Si–O–Si bond angles.

The optimisation resulted in a slight change in the models' atomic structures. As can be seen from Fig. 3.10, the Si–O bond lengths show similarly shaped distributions before and after optimisation, but the average bond length shifts up to 1.61 Å, in much closer agreement with the experimental value of 1.62 Å.[74] Similarly, the O–Si–O and O–Si–O bond angles, shown in Fig. 3.10, show similar shapes before and after optimisation. The average of the O–Si–O angle after optimisation is 109.47°, very similar to the unoptimised structure. However, the O–Si–O angle averages at 146°, very different from the unoptimised structure and much closer to experiment. The

total structure factor of the DFT optimised structures is plotted in Fig. 3.9 along with the original ReaxFF structures and experimental data. The structure factors are very similar at shorter ranges (< 7.5 Å^{-1}) before and after DFT optimisation, with the optimised structures showing better agreement at longer ranges. The error compared to the experimental data is reduced after optimisation, indicating that the optimisation is a useful step in calculating the atomic structure of a-SiO_2.

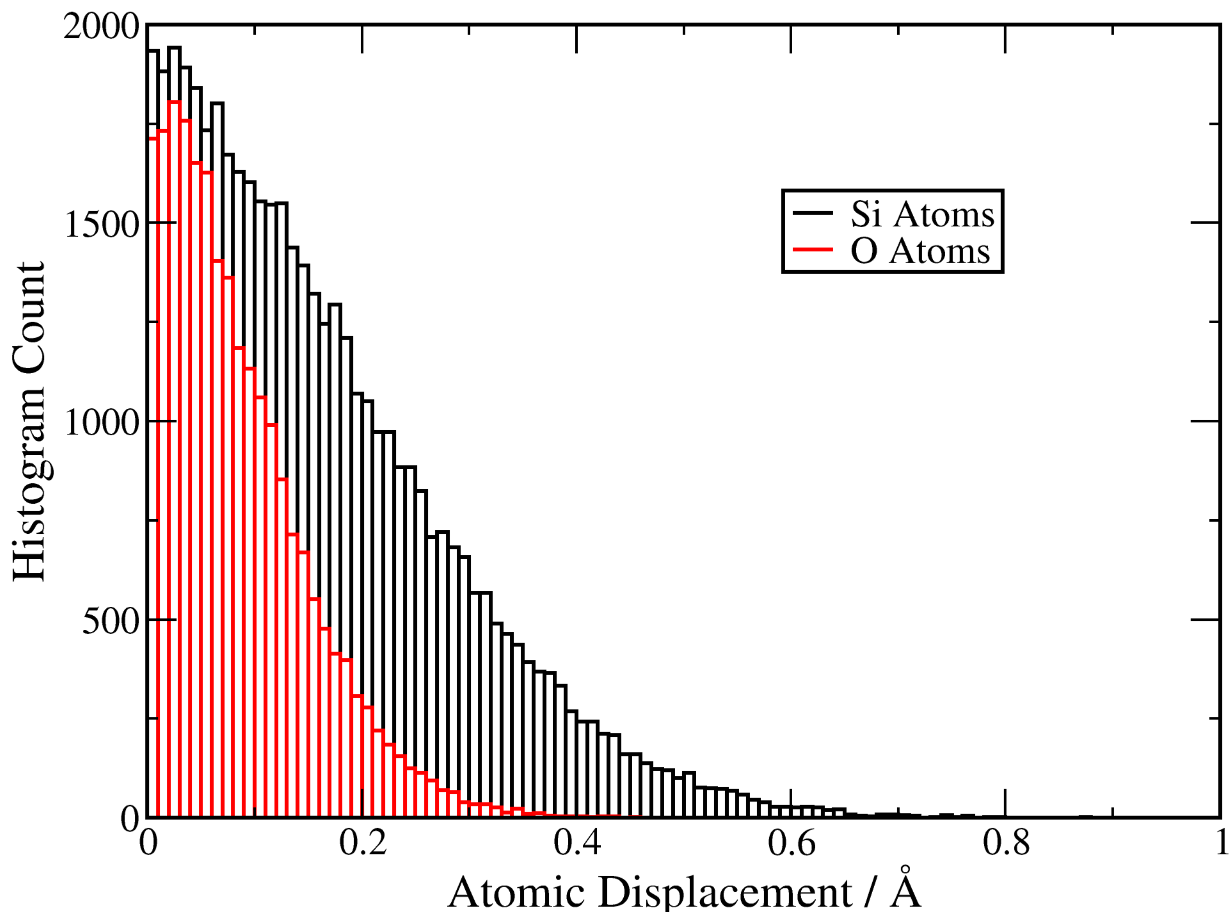

Figure 3.11: Histogram of the atomic displacements of the ReaxFF a-SiO_2 models before and after DFT optimisation.

To obtain a measure of the difference between the ReaxFF structures before and after DFT optimisation, their displacement fields have been calculated as:

$$\mathbf{D} = [\mathbf{J}_{3,1} \cdot (\mathbf{R}_{DFT} - \mathbf{R}_{ReaxFF})^{\circ 2}]^{\circ \frac{1}{2}}, \tag{3.6}$$

where $\mathbf{D}$ is a matrix in which element i is the displacement of the ith atom, $\mathbf{J}_{3,1}$ is a 3×1 matrix of ones, $\circ$ indicates the Hadamard product, $\mathbf{R}_{ReaxFF}$ and $\mathbf{R}_{DFT}$ are

matrices of the atomic coordinates before and after DFT optimisation, respectively. The displacements of all atoms are plotted in Fig. 3.11 for both Si and O atoms. The displacements peak at well below 0.1 Å and extend to 0.4 Å and 0.8 Å for O and Si atoms, respectively. These results indicate that the ReaxFF structures are very close to a DFT minimum, but that the parameters for the Si atoms could be better optimised.

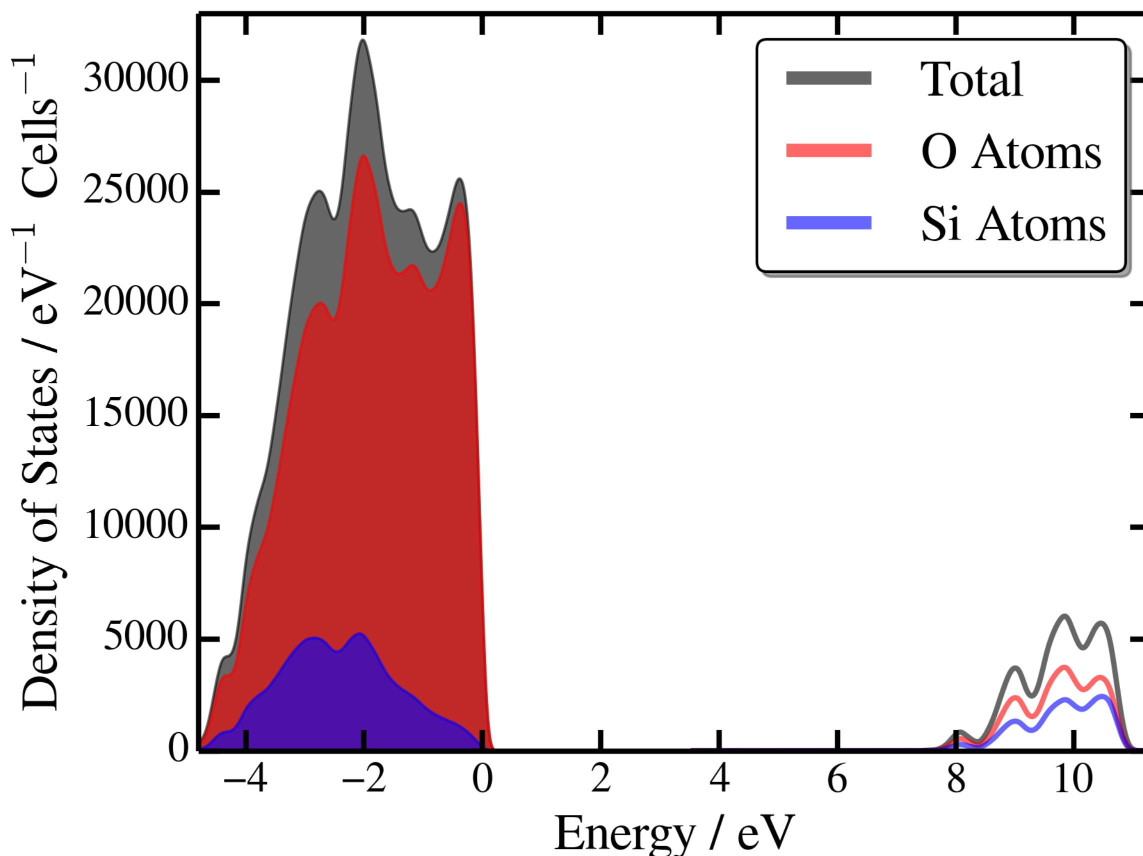

Figure 3.12: Electronic densities of state from 320 models of a-SiO_2. Each state is broadened by a Gaussian with a sigma value of 0.1 eV. The black curve is the total, while the red and blue curves are the densities of state projected onto Si and O atoms, respectively. The areas of the curve which are filled in to the baseline indicate occupied states, while the curves which are not filled in indicate unoccupied states. The states' energies are normalised so that the Fermi level lies at 0.0 eV.

To assess the electronic structures of the a-SiO_2 models, their electronic densities of state were calculated. Fig. 3.12 shows a summation of these extracted densities of state from the 320 models of a-SiO_2. Each state is broadened by a Gaussian with a sigma value of 0.1 eV to simulate homogeneous broadening. In addition, the densities of state were projected onto Si and O atoms in order to assess each

atom type's contribution to the total density of states. All states are aligned so that the Fermi level lies at 0.0 eV and the occupied states lying below the Fermi level are filled in to the base line. Immediately, one can see that a-SiO_2 is an insulator with a very wide band gap. The average band gap extracted from these calculations is 8.1 eV and ranges from 7.1 to 8.4 eV. This is a slight underestimation of the experimental SiO_2 band gap, which has been measured optically as 8.8 eV.[75] The traditional exchange-correlation functionals, such as the local density and gradient corrected approximations, are known to underestimate the band gap of materials, with the band gaps of these models calculated with PBE (a gradient corrected functional) averaging at 6.4 eV . However, the inclusion of Hartree-Fock exchange is known to improve the calculated band gap. Increasing the amount of Hartree-Fock exchange increases the band gap, but it also changes the chemical properties of the material in an unpredictable manner. In fact, in the literature many studies have used the proportion of Hartree-Fock exchange as an effective tuning parameter to replicate the band gap. However, in this thesis the amount of HF exchange will remain at 0.2, the value quoted in the original PBE0_TC_LRC functional's paper. It is also clear to see that the top of the a-SiO_2 valence band is dominated by contributions from O atoms. In fact, these are contributions from O non-bonding 'p' states. The bottom of the conduction band is made up of hybrid Si 'sp' states as well as non-bonding O 'p' orbitals as well. An interesting property that emerges from these calculations is that the extrema of the bands are not entirely delocalised, but are instead partially localised at particular locations in these structures. The disorder of the amorphous SiO_2 structures leads to deviation from band theory, with the states induced by disorder known as the band's Urbach tails in the literature.[76] The ability of these Urbach states to act as precursors to strong localisation is known as Anderson localisation [77] and these states in a-SiO_2 are explored in detail in chapter 6.

3.3.3 Summary

A molecular dynamics procedure is established to generate a-SiO_2 structures by adjusting the time step, thermostat and barostat and following a melt and quench procedure. The ReaxFF potential is used to generate 320 a-SiO_2 samples. The resulting amorphous structures are characterised and found to agree very well with experiment; the density is very close to the experimental value as are the total structure factors. These structures were then optimised using DFT leading to an even better agreement of the atomic structure with experiment. Their electronic structures were extracted showing that the calculated band gaps are in reasonable agreement with experiment, albeit a little too low. These results indicate that the use of molecular dynamics and ReaxFF can provide an accurate description of the structure and disordered nature of amorphous silica. Further optimisation using DFT is not necessary to improve the description of the atomistic structure, but is necessary to extract the electronic structure.

3.4 Constructing the Si/SiO_2 Interface

Making a credible model of the Si/SiO_2 interface has proved to be extremely challenging due to a lack of information of the microstructure of the interface. From transmission electron microscope (TEM) images it is known that silicon evolves from its crystalline elemental form into the totally disordered and fully oxidised amorphous silica over a 5 Å abrupt transition region.[78,79] It is also known that Si–O–Si angles are more compressed at the interface than in bulk silica.[80] X-ray reflectivity (XRR) experiments reveal that the density of the SiO_2 layer in the Si/SiO_2 system is higher than that of bulk SiO_2, measuring between 2.36 g cm^{-3} and 2.41 g cm^{-3}. X-ray photoelectron spectroscopy (XPS) measurements again show that the transition region is approximately 5 Å and also give a measure of the concentration of partially oxidised silicon atoms across the interface. From this data, Si^{+1} and Si^{+2} species appear right at the interface on the bulk silicon side. On going further into the transition region

the Si^{+1} and Si^{+2} species subside and Si^{+3} appears. The XPS data indicates that the ratio of the partially oxidised silicon atoms is 1:2:3 for Si^{+1}:Si^{+2}:Si^{+3}.[81] This experimental data sets out the criteria for an ideal model of the interface. In summary, the model must satisfy the following criteria:

- Contain an a-SiO_2 layer which matches the geometrical description of bulk amorphous silica past the interface and a substrate which matches elemental Si before the interface.
- The model must contain a transition layer which neither matches bulk silicon nor bulk silica.
- Contain an a-SiO_2 bond length distribution which is slightly longer than that of bulk a-SiO_2 in the interface region.
- Possess an Si-O-Si angle distribution which is more compressed with respect to bulk silica.
- The density of the amorphous silica layer should be higher than that of bulk amorphous silica.
- The correct distribution of silicon in intermediate oxidation states across the interface, obtained from XPS experiments.

3.4.1 Melt and Quench *in situ*

A model of the Si/SiO_2 interface was prepared starting from a 3x3x4 periodic supercell of crystalline silicon. Oxygen atoms were then inserted in the 001 direction between silicon atoms over 4 layers to make a layer of silica. This initial stack is shown in Fig. 3.13. Inserting oxygen atoms between silicon atoms results in the SiO_2 layer being very similar to the crystal structure of β-cristobalite; however, the lateral cell vectors of this silica layer, which are the same as the silicon unit cell (5.28 Å), are much more compressed than the β-cristobalite cell vectors (7.12 Å). To remove some of the stress that comes from compressing this β-cristobalite layer, the silica layer

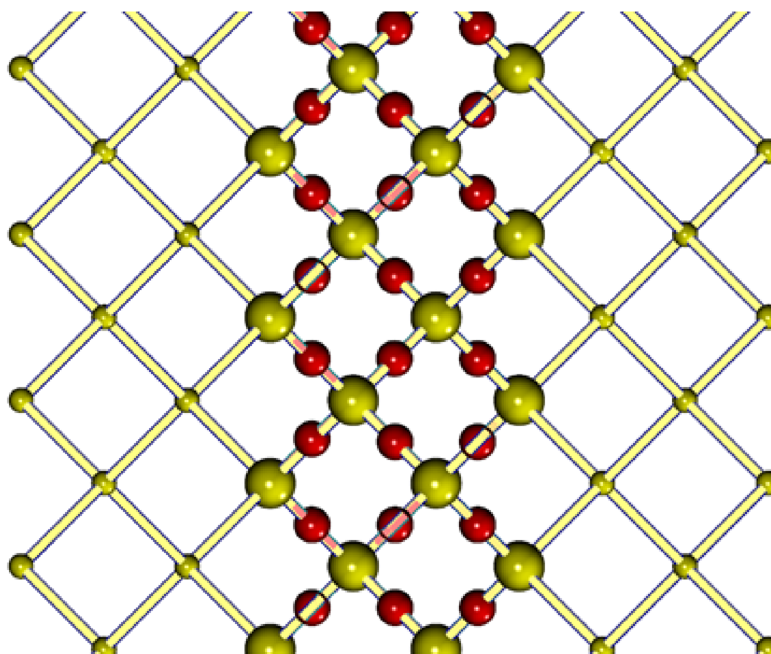

Figure 3.13: Silicon supercell with oxygen atoms inserted to form silica layer. Note that the atomic structure of the SiO_2 layer is almost identical to that of β-cristobalite.

was then extended in the direction of the interface so that the density of the silica layer corresponded to that of β-cristobalite. Random velocities from a Gaussian distribution were then assigned to all atoms so that the temperature of the system was 300 K and a molecular dynamics simulation was then run for 20 ps. The temperature and pressure were maintained at 300 K and 1 bar using a Berendsen thermostat and barostat whose time constants are obtained from section 3.3.1. The temperature of the silicon substrate was then fixed at 300 K while the temperature of the SiO_2 layer was brought up to 5000 K to form a liquid melt of the silica layer. The temperature of the silica layer was then fixed at 5000 K, while the temperature of the silicon substrate remained fixed at 300K, and a simulation was run for 1ns. The silica layer was then cooled down to 300 K at a rate of 6 K ps^{-1}.

The resulting structure is shown in Fig. 3.14. Upon visual inspection, it appears that many oxygen atoms have moved out of the silica region and penetrated the silicon substrate. Due to the high temperature required by the ReaxFF potential to melt SiO_2 (see section 3.3.1), the oxygen atoms have a very high velocity which allows them to move through the silicon substrate easily. The system prepared this way also

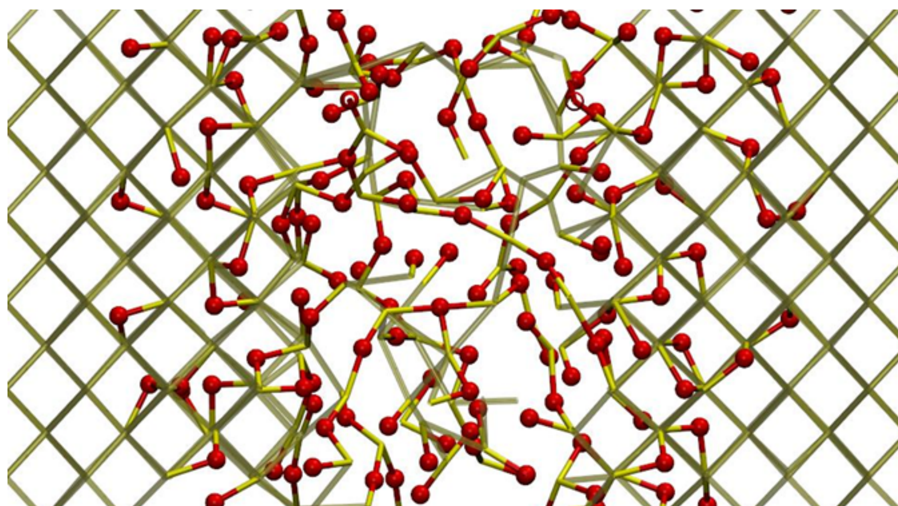

Figure 3.14: Si/SiO_2 stack after *in situ* melt and quench of the SiO_2 layer. SiO_2 layer does not form an abrupt interface with oxygen atoms penetrating deep into the silicon substrate. In addition, there is a large number of coordination defects both in the Si substrate and the SiO_2 layer.

generates a wide range of coordination defects, including triply coordinated oxygen atoms, singly coordinated oxygen atoms and overcoordinated silicon atoms. Although this analysis is not particularly extensive, it already indicates that this method is unsuitable for the creation of an ideal Si/SiO_2 interface system. For the purposes of investigating the defects which may exist at the interface, the stack prepared in this way cannot be used as there are far too many coordination defects which distort the physics and chemistry of the ideal Si/SiO_2 interface.

3.4.2 a-SiO_2 Layer Strained to Silicon Lateral Dimensions

To overcome the limitations of the melt and quench method and use it to model the Si/SiO_2 interface, the procedure needs to be improved in a way that would eliminate coordination defects. A similar method was then investigated in which the amorphous silica layer is made in an independent system so that it can be inserted between the silicon substrate. This a-SiO_2 layer is made starting from a periodic model of β-cristobalite whose lateral cell dimensions have been fixed to that of silicon (in this case 5.28 Å for both the a and b cell parameters). The size of the box in the 001 direction is allowed to move by using a Berendsen barostat that adjusts the pressure of the system by scaling only the z dimension of the simulation box. Random velocities

are assigned to all atoms in the system so that the system's temperature is 300 K and a molecular dynamics simulation with 3D periodic boundary conditions is run for 20 ps. The temperature and pressure are again controlled using the Berendsen thermostat and barostat. The temperature of the system is then raised linearly to 5000 K and the temperature is then maintained at 5000 K for 1 ns. The system is then cooled down to 300 K at a rate of 6 K ps^{-1} and minimised to give an amorphous silica sample sandwiched between silicon.

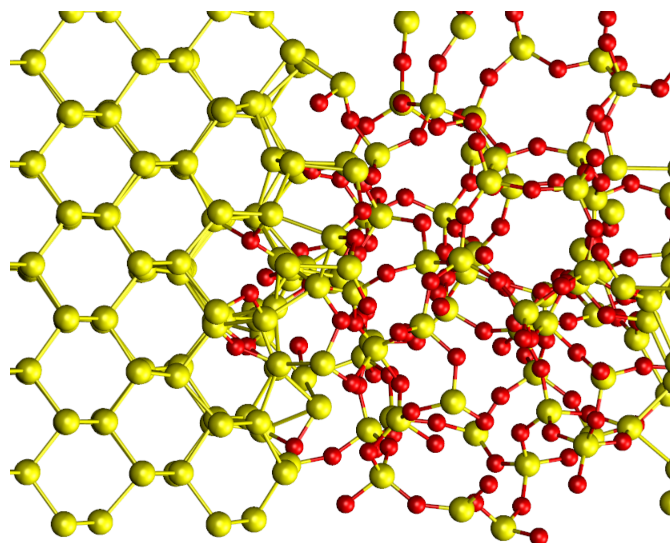

Figure 3.15: Si/SiO_2 interface made with a-SiO_2 layer placed on top of silicon.

The resulting amorphous silica structure is a continuous random network which contains no defects. It has the same geometrical distributions as the amorphous silica described in section 3.3.1. The amorphous silica layer was then heated to 600 K and equilibrated at that temperature for 20 ps. In a separate system, a $3 \times 3 \times 3$ supercell of crystalline silicon was heated to 600 K and equilibrated also for 20 ps. The atomic coordinates and velocities of the silica system were then copied into the crystalline silicon system, with the coordinates of the silica atoms translated in the 001 direction so that the silica layer was placed over the silicon substrate separated by a 1.6 Å vacuum gap on either side of the silica layer. This vacuum gap is introduced so that the atoms at the surfaces of the silicon substrate and the silica layer will have freedom to try and position themselves in energetically favourable positions and is also the reason for heating the system up to 600 K. The box will be allowed to relax

in the dimension perpendicular to the interface and it is hoped that new bonds will be formed at the interface. The 1.6 Å gap was chosen after several simulations were run with vacuum gaps ranging from 1.6 Å to 2.5 Å. The simulations which contained the 1.6 Å vacuum gap produced the least overcoordinated oxygens while the larger vacuum gaps resulted in unphysical surface terminations for both the Si and SiO_2 layers. A molecular dynamics simulation is then run on this Si/vacuum/SiO_2 stack under periodic boundary conditions for 1ns with the temperature maintained at 600K and the pressure maintained at 1 bar. The system was then cooled down to 300 K at a rate of 6 K ps^{-1} and Fig. 3.15 shows the interface formed using this method. Immediately upon visual inspection, it can be seen that the interface formed is abrupt and amorphous.

The geometrical properties of this interface model are presented in Fig. 3.16. The Si–O bond length distribution peaks at around 1.65 Å. This is slightly longer than that of bulk silica and is to be expected according to infra-red absorption (IR) experiments.[2] However, the bond lengths range from 1.55 Å to almost 2.0 Å in contrast to IR experiments which do not find bond lengths longer than 1.75 Å. The mean O–Si–O angle is 109.22°, which is to be expected as the SiO_4 units maintain their rigid tetrahedral shape. As can be seen in Fig. 3.16, the Si–O–Si angle peak has shifted to the left with respect to the peak in bulk amorphous silica (see Fig. 3.7). The mean Si–O–Si angle from this interface model is 136.60°, in excellent agreement with the conclusion reached by Hirose *et al.* (drawn from XPS experiments and molecular orbital calculations) that the Si-O-Si angle is reduced to 135°.[82] The oxidation state of silicon across the interface is also shown in Fig. 3.16. It shows that Si^{+1} and Si^{+2} appear first at the interface while Si^{+3} appears deeper into the interface. The profile shows a gradual change over a 5 Å region from elemental silicon (Si^0) to fully oxidised silicon (Si^{+4}), qualitatively similar to what is seen in XPS experiments. The ratio of partially oxidised silicon atoms in this model is calculated as 1:0.4:0.3 (Si^{+1}:Si^{+2}:$^{+3}$). This ratio does not match XPS[83] data which shows a ratio of Si^{+1}:Si^{+2}:$^{+3}$ of 1:2:3. The density of the silica layer is 2.37 g cm^{-3} which is also in good agreement with

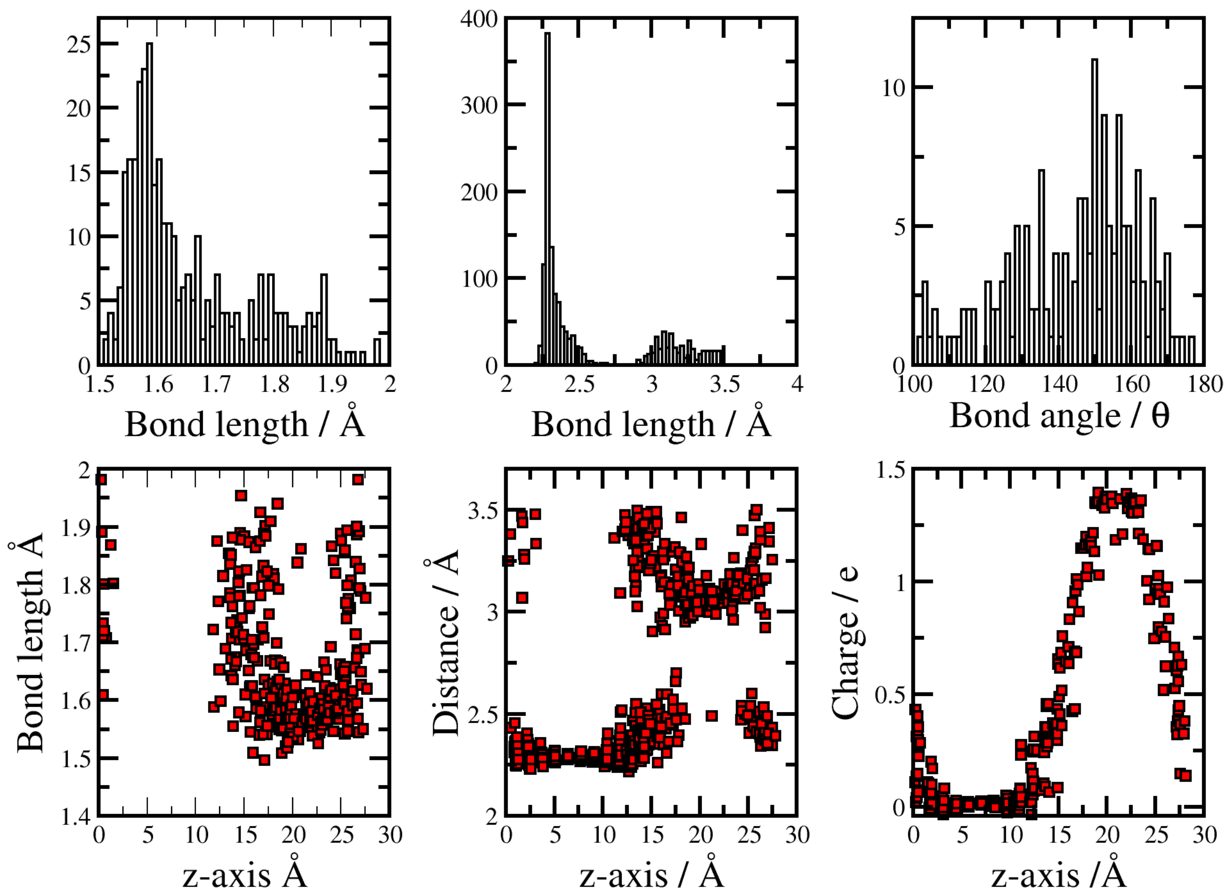

Figure 3.16: Geometrical properties of Si/SiO$_2$ interface made with a-SiO$_2$ layer placed on top of silicon. a) The Si–O bond length distribution in the stack. b) The Si–Si nearest neighbour distance in the stock. Note that it displays a bimodal distribution; one for the bonds in the Si substrate, the other for the Si nearest neighbours in the a-SiO$_2$ layer. c) The Si–O–Si bond angle distribution. d) The Si–O bond length distribution as a function of its position along the z axis. e) The Si–Si distances as a function of position along the z axis. f) The ReaxFF charges calculated for Si as a function of position on the z axis.

experiment.[81]

3.4.3 Summary

Using this method, one can reproduce bond angle statistics, density of amorphous silica and the qualitative profile of silicon oxidation states across the interface. However, the bond length distribution contains lengths which are far too long. The concentration of silicon in intermediate oxidation states in the transition region does not match the experimental ratio seen by XPS experiments. This needs to be corrected if the model is to be used to study defects at this interface as the defect's properties will be

strongly influenced by the chemistry. The wrong chemistry at the interface will lead to a wrong description of the defect.

3.5 Conclusions

An interatomic potential known as ReaxFF was chosen to model amorphous silicon dioxide. The potential allows the charges of the individual atoms to be calculated based on the system's instantaneous geometry. ReaxFF was used to construct 320 models of a-SiO_2 using a melt and quench method showed excellent agreement with experimental data. The melt and quench method was extended to the Si/SiO_2 system. However, it requires additional modification before it can be used to confidently study the atomic structure of the Si/SiO_2 stack.

4

Defects in Bulk SiO_2

4.1 Introduction

Point defects can strongly influence a material's physical and chemical properties. The properties of silicon dioxide have long been exploited in a number of technological applications. In particular, SiO_2 is used in electronic devices due to its extremely high quality interface with the semiconducting Si substrate – high quality in this context means very few defects at the interface between Si and SiO_2. Defects in SiO_2 have been implicated in many electronic device reliability issues, such as random telegraph noise (RTN), bias temperature instability (BTI), and stress-induced leakage current,[11] as well as in degrading the device performance by reducing the channel mobility.[84] It is thought that defects in the oxide can capture and emit the available carriers in the

semiconductor channel of electronic devices, leading to a strong electrostatic effect on the carriers flowing through the device.

This chapter serves two purposes. Firstly, it presents a brief overview of defects in bulk silica, particularly those that have been implicated in electronic device reliability issues. Secondly, a number of defects that have been studied in the literature have been re-calculated to assess the validity and accuracy of the computational methods used in this thesis, discussed in detail in chapters 2 and 3.3.1. The defects studied in this chapter are the oxygen vacancy and its charged variants. Initially, the electronic structure of oxygen vacancies in α-quartz are investigated as it is instructive to investigate defects in a crystalline environment with minimal structural disorder. In addition, many crystalline point defects are thought to have analogues in amorphous silica.[85] The positively charged vacancy, a variant of which is widely known as the E' centre, and the negatively charged vacancies are then studied. Finally, the oxygen vacancy and its charged configurations are studied in a-SiO_2.

4.2 Quartz

4.2.1 Neutral Oxygen Vacancy

The neutral oxygen vacancy – also known as oxygen deficient centre I (ODC I) – has been modelled previously using various methods, including *ab initio* and semi-empirical calculations, and modelled within an embedded cluster scheme and periodic boundary conditions. Blöchl calculated the structure of the neutral vacancy in a 72 atom periodic cell of α-quartz.[86] His calculations were performed using DFT with the exchange and correlation described within the generalised gradient approximation (GGA). Sulimov *et al.*[87] also modelled the neutral oxygen vacancy in quartz using the embedded cluster method[88] which allowed them to model larger systems than if they were to use quantum mechanical methods on their own. In Sulimov's investigation, a cell of quartz containing 9270 classical atoms and up to 67 quantum atoms was used initially. An oxygen atom was removed from the region which is

calculated quantum mechanically to form the oxygen vacancy. Various calculations were performed with the quantum mechanical region varying in size from a cluster containing two silicon atoms (and four oxygen atoms) to eighteen silicon atoms (forty-nine oxygen atoms). The quantum mechanical region was allowed to relax while the classical region remained fixed and the structure of the neutral oxygen vacancy was elucidated.

Results from both Sulimov and Blöchl's calculations provide a similar picture on the structure of the neutral oxygen vacancy in α-quartz. Removal of the oxygen atom from between the two silicon atoms leaves behind a dangling bond on each of the silicons. The silicon atoms, initially ≈ 3.2 Å apart, then displace toward each other to form a fairly strong Si–Si bond which measures 2.4 Å. Sulimov also investigated the displacement field of the neutral oxygen vacancy which was found to be very long ranged indeed, extending to as far as 13 Å away from the vacancy site. The long range network relaxation has been shown to be asymmetric due to the absence of inversion symmetry in quartz.[87]

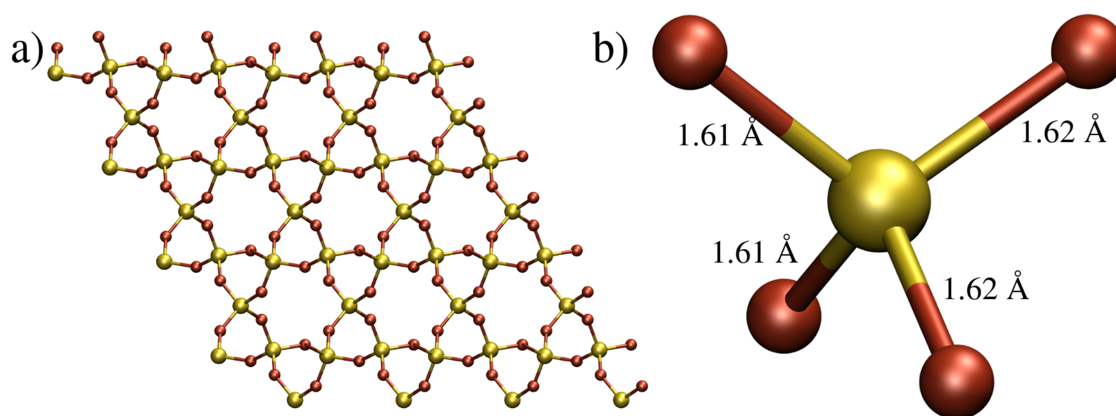

Figure 4.1: a) Crystal structure of α-quartz and b) asymmetry of an SiO_4 tetrahedron in α-quartz.

In this investigation, the neutral oxygen vacancy in α-quartz was modelled using periodic DFT as described in chapter 2. Initially, a $3 \times 3 \times 3$ cell of α-quartz containing 243 atoms was constructed using coordinates obtained from X-ray diffraction studies.[89] To describe the electrons around the Si and O atoms, the GTH pseudopotentials[90] and double-ζ basis sets (including polarisation functions)[91] were ap-

plied to the atomic coordinates. The exchange and correlation were described by the PBE0_TC_LRC functional[30] with a cutoff radius of 2.0 Å for the truncated Coulomb operator. The electronic structure was then calculated within the DFT formalism using the CP2K code and the system's geometry was optimised with respect to its energy so that the maximum force per atom in the system is less than 37.1 pN. Optimisation of this structure lead to the peculiar α-quartz structure; for each SiO_4 tetrahedron, there are two long (1.61 Å) and two short bonds (1.60 Å). Fig. 4.1 shows both the α-quartz structure and a single SiO_4 tetrahedron with the short and long bonds highlighted.

To model the neutral oxygen vacancy, an oxygen atom was then removed randomly from the optimised α-quartz cell, leaving behind a cell containing 242 atoms. All oxygen atoms have one short and one long bond to silicon resulting in the same chemical environment, so it does not matter which oxygen atom is removed. The system was then optimised, resulting in the structure of the neutral oxygen vacancy, which is shown along with its highest molecular orbital (HOMO) in Fig. 4.2. Optimising the vacancy displaced the silicon atoms surrounding the vacancy toward each other, forming a Si–Si bond of 2.44 Å. This is in excellent agreement with the bond length calculated by Blöchl in a smaller periodic model containing only 72 atoms and calculated using the PBE functional using a plane wave code. The newly formed bond is a σ bonding state which is high in Si 'p'-orbital character. The one-electron defect level associated with the vacancy is a deep state, lying 0.8 eV above the valence band, shown in the calculated electronic density of states in Fig. 4.2.

	This investigation	Blöchl paper [86]
Si_L-Si_S	2.439	2.445
Si_L-O(3+)	3.884	3.893
Si_S-O	1.653	1.642
Si_L-O	1.648	1.641
All bond lengths are measured in Å		

Table 4.1: Comparison of neutral oxygen vacancy geometries in different models

A comparison of this geometry with Blöchl's model is presented in table 4.1, showing excellent agreement. The displacement field has also been calculated and

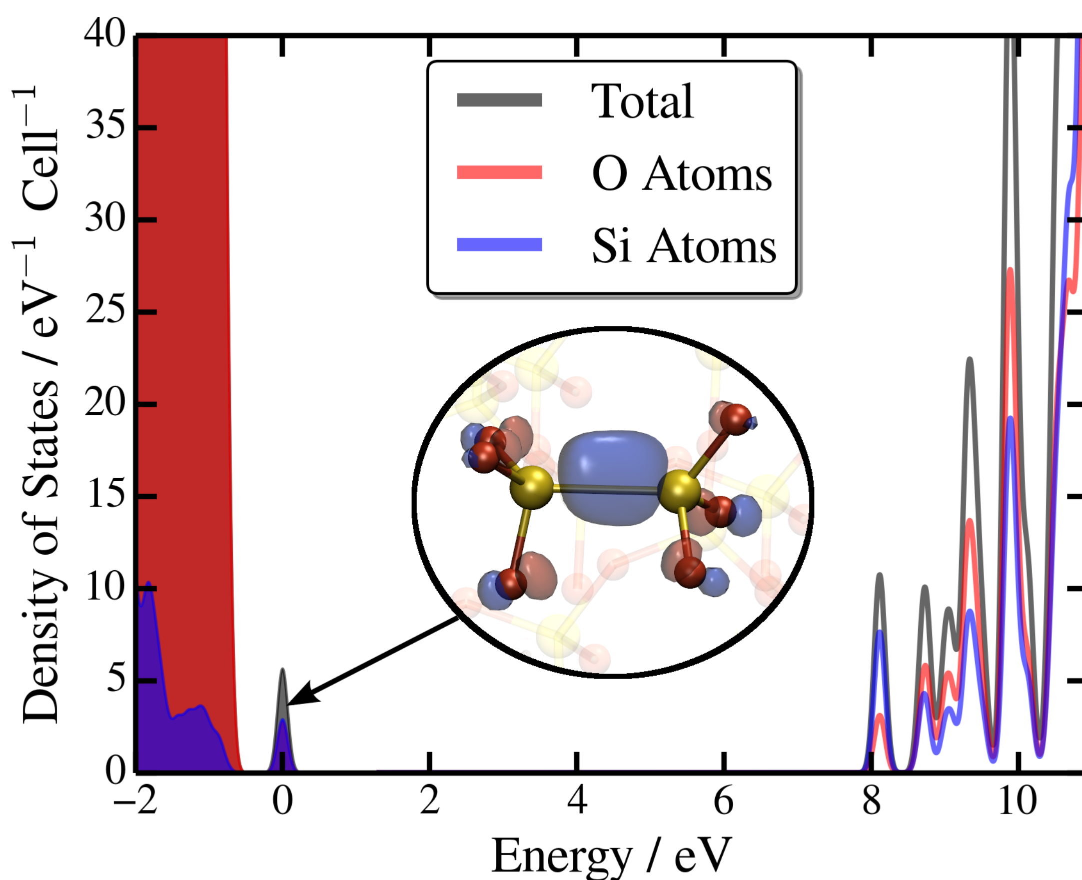

Figure 4.2: Atomic and electronic structure of neutral oxygen vacancy in α-quartz The graph shows the electronic density of states for a single NOV in a 242 atom cell of α-quartz. An occupied state breaks off the top of the valence band and is highly localised at the vacancy, as seen in the inset which visualises this state as an isosurface (with an isovalue of 0.09) alongside its atomic structure. The Si atoms surrounding the vacancy displace towards each other forming a Si–Si bond.

is shown in Fig. 4.3. It is interesting to see that although the local structure of the neutral oxygen vacancy had converged in Blöchl's smaller periodic model, in these calculations, containing 242 atoms and a cell 5 Å bigger in each dimension, the displacement induced by this defect persists right up to the edge of the simulation box. It would be interesting to investigate whether the displacement field is even more long ranged than this or whether the long ranged displacement is an artefact of some parameter of the calculation.

4.2.2 Positive Oxygen Vacancy

The positive oxygen vacancy (POV) has been studied extensively both experimentally and theoretically as it is implicated in various device reliability issues.[84] In particular, *ab initio* calculations of the POV have been used to explain the origins of $^1/_f$ noise and thermally stimulated current in MOS devices,[84,92,93] with suggestions that these

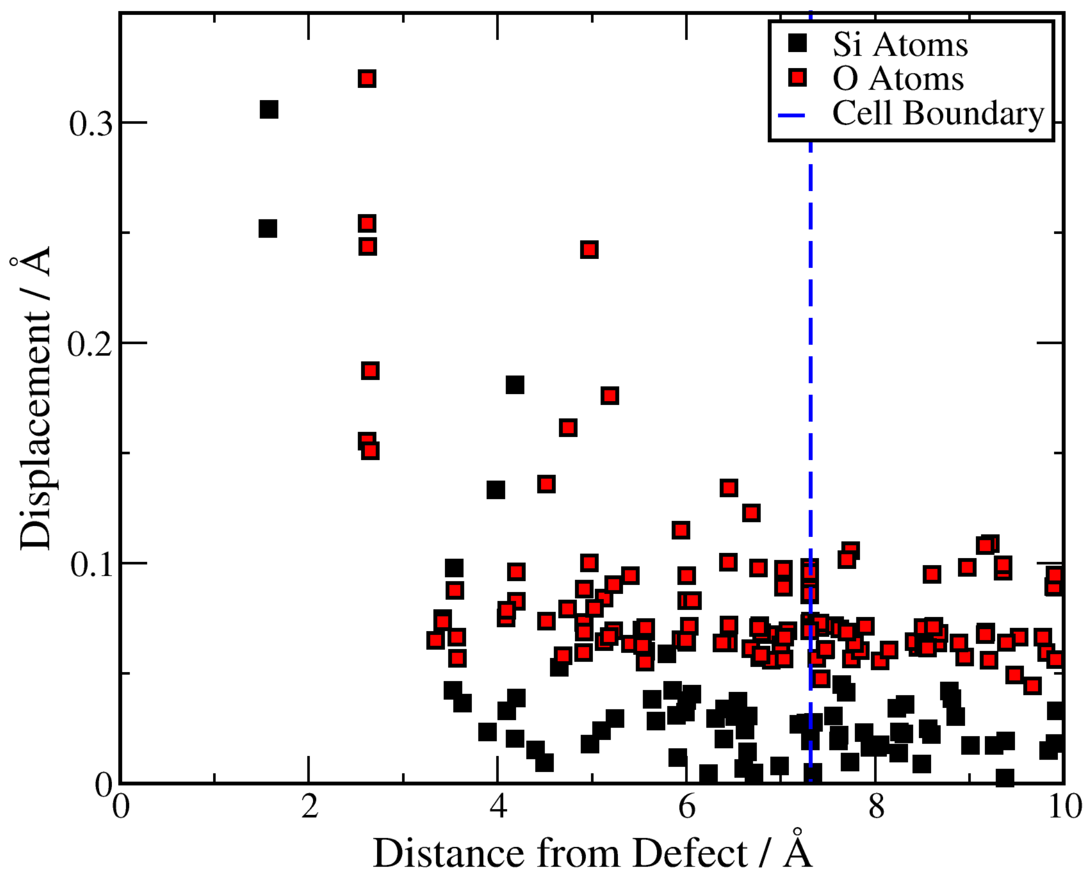

Figure 4.3: Displacement field of neutral oxygen vacancy in quartz.

issues are caused by thermally activated capture and emission of holes at neutral oxygen vacancy sites. A similar mechanism has been proposed for explaining NBTI; however, the atomic nature of the hole traps involved has not been fully resolved.[94–96]

Various structures have been proposed for the POV, assuming that it is formed directly from the neutral oxygen vacancy. A hole is introduced into the neutral oxygen vacancy which localises at that site giving the structures of the POV. The most prominent of the positive oxygen vacancies are categorised into two kinds: The first is a “dimer” vacancy configuration, with an analogue known as the E'_δ centre in a-SiO_2,[86,97] while the second is a centre in which one of the Si atoms relaxes through the plane of its oxygen neighbours forming a ‘puckered’ configuration known as the E'_1 centre in α-quartz with its analogue known as the E'_γ centre in a-SiO_2.

Blöchl investigated the positive oxygen vacancy using the same calculation details as for his neutral oxygen vacancy calculations discussed earlier in this chapter. After introducing a hole into the optimised NOV in quartz, the atomic coordinates are relaxed resulting in the dimer configuration of the positive oxygen vacancy. Mysovsky *et al.* also calculated the structure of the positive oxygen vacancy using the embedded cluster method.[98] The quantum mechanical cluster used in this study was a $Si_{11}O_{33}$ cluster, while the whole system (quantum mechanical cluster embedded into classically polarisable system) contained 9270 atoms. The electronic structure of this quantum mechanical cluster was calculated using DFT with the exchange-correlation described using the GGA functional. The orbitals were described using a local orbital basis set which consisted of norm-conserving pseudopotentials for the core orbitals and a double-ζ basis set for the valence orbitals. The structure of the dimer configuration was then obtained by putting a hole into the optimised neutral oxygen vacancy structure and optimising the atomic coordinates.

Both Mysovsky and Blöchl’s studies reach similar conclusions, the dimer configuration is highly similar to the structure of the neutral oxygen vacancy but the Si–Si bond is relatively weak. Blöchl finds that the vacancy bond expands by 23%, so that the Si–Si bond is comparable in length to an oxygen bridge in quartz.

The puckered configuration is a relaxation of one of the silicon atoms through the plane of its oxygen neighbours, forming a bond with an oxygen atom behind it. This happens due to the asymmetry of the tetrahedral unit, such that there is always an oxygen atom behind the silicon atoms associated with the long Si-O bonds while there is no oxygen atom behind the silicon atoms associated with the short Si-O bonds.

Here, both the dimer and puckered configurations of the POV in quartz were investigated. The dimer configuration was obtained spontaneously upon the addition of a hole into an NOV structure. However, to obtain the puckered configuration, a perturbation to the structure is required to overcome the energetic barrier to its formation. Despite there being a barrier, the puckered configuration was found to be more thermodynamically favourable than the dimer configuration.

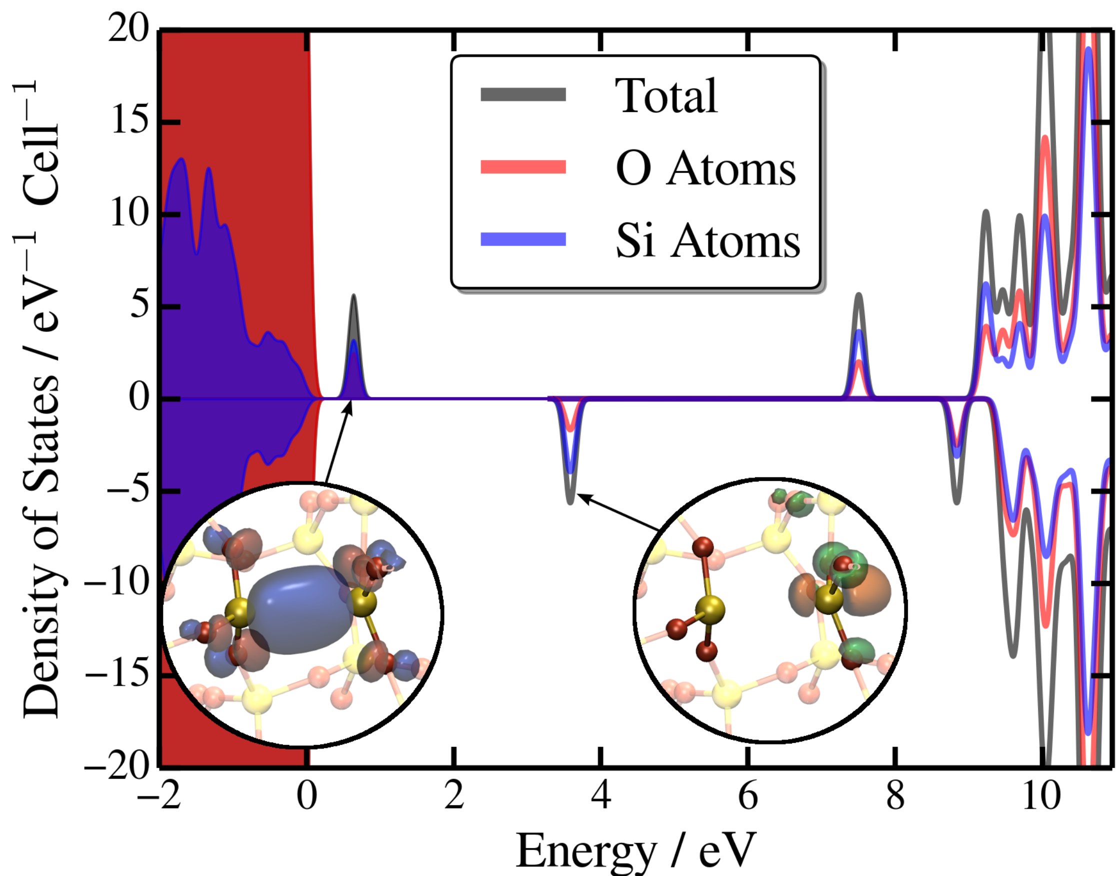

Figure 4.4: Atomic and electronic structure of the dimer configuration of the positive oxygen vacancy in α-quartz. The graph shows the electronic density of states with the filled in section indicating the occupied states. The densities in the positive y-axis are from α spin states while the β-spin states occupy the negative y-axis. The highest occupied state in the α-spin and lowest unoccupied state in the β-spin are visualised in the insets along with the atomic structure of the dimer configuration.

Dimer configuration

Using the same calculation parameters described in chapter 4.2.1, the positive oxygen vacancy was investigated. Starting from the neutral oxygen vacancy structure, a hole was added to the system and its geometry was optimised. The atomic structure is presented in the insets of Fig. 4.4 (note that both insets show the same atomistic structure). Adding a hole into the system displaces the two Si atoms surrounding

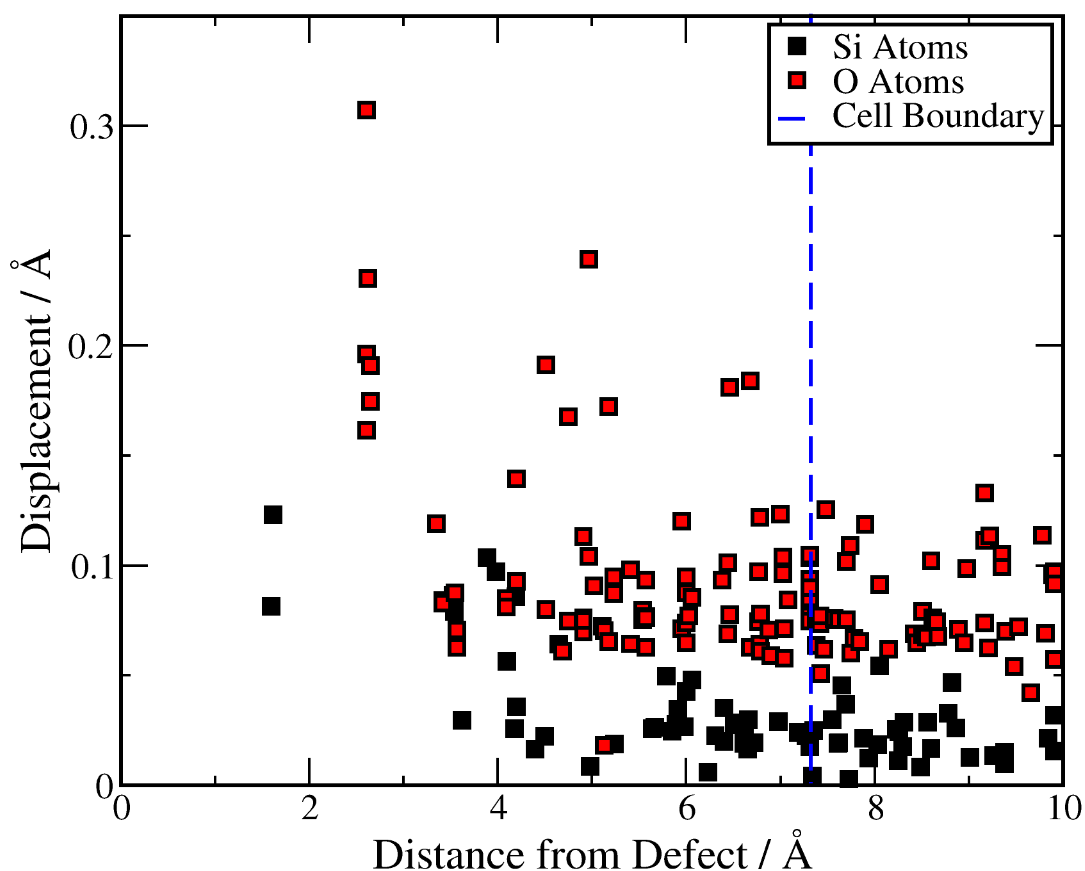

Figure 4.5: Displacement of the atoms from their lattice sites when the POV is introduced. The black squares are Si atoms and the red squares are O atoms.

the vacancy from their position in the bulk. A longer range distortion can also be seen in the displacement field shown in Fig. 4.5, although it is not as strong as that of the neutral oxygen vacancy. The Si–Si bond in the dimer configuration is 2.93 Å, showing that it is significantly weaker than that in the neutral oxygen vacancy. This can be understood as an electron taken out of the stabilising bonding orbital, leading to a weaker bond between the two Si atoms and causing them to displace away from each other. This idea can be confirmed by visualising the highest occupied and lowest

	This investigation	Blöchl paper [86]	Mysovsky paper [98]
Si_L-Si_S	2.932	3.011	2.890
Si_L-O(3+)	3.608	3.554	
Si_S-O	1.603	1.600	
Si_L-O	1.598	1.597	
All bond lengths are measured in Å			

Table 4.2: Comparison of positive oxygen vacancy dimer configuration geometries in different models

unoccupied states in the α and β spin channels, respectively. They can both be seen in the insets of Fig. 4.4. The HOMO in the α channel shows a bonding orbital between the two Si atoms, while the LUMO of the β channel, the state from which an electron was removed, is clearly localised on just one of the Si atoms. The relaxation of the dimer configuration moves an occupied defect state further into the band gap, so that it lies 1.2 eV above the valence band, shown in Fig. 4.4. Calculating the spin moment reveals that the spin density is shared between the Si atoms surrounding the vacancy, although it is shared asymmetrically. We can categorise the two Si atoms based on whether the oxygen removed formed a long bond or a short bond, which we will refer to as Si_L and Si_S, respectively. The spin moment of Si_L, the Si on which the hole is localised (see LUMO in β-channel in Fig. 4.4) is 0.36 while it is slightly higher on Si_S at 0.41. We also find that Si_L has a slightly more positive Mulliken charge of $+0.96|e|$ compared to the $+0.94|e|$ of Si_S. This follows from the spin moment calculation, as the unpaired spin is due to an electron which is less localised on Si_L and therefore that centre is more positively charged. However, both Si atoms are much less positively charged than the average charge of $+1.09|e|$ for the remaining bulk Si atoms. The geometrical properties of this model and those obtained from the literature are presented in table 4.2. The structure calculated in this periodic model containing 242 atoms agrees excellently with previous results, suggesting that the dimer configuration is well described in cells containing 72 atoms.

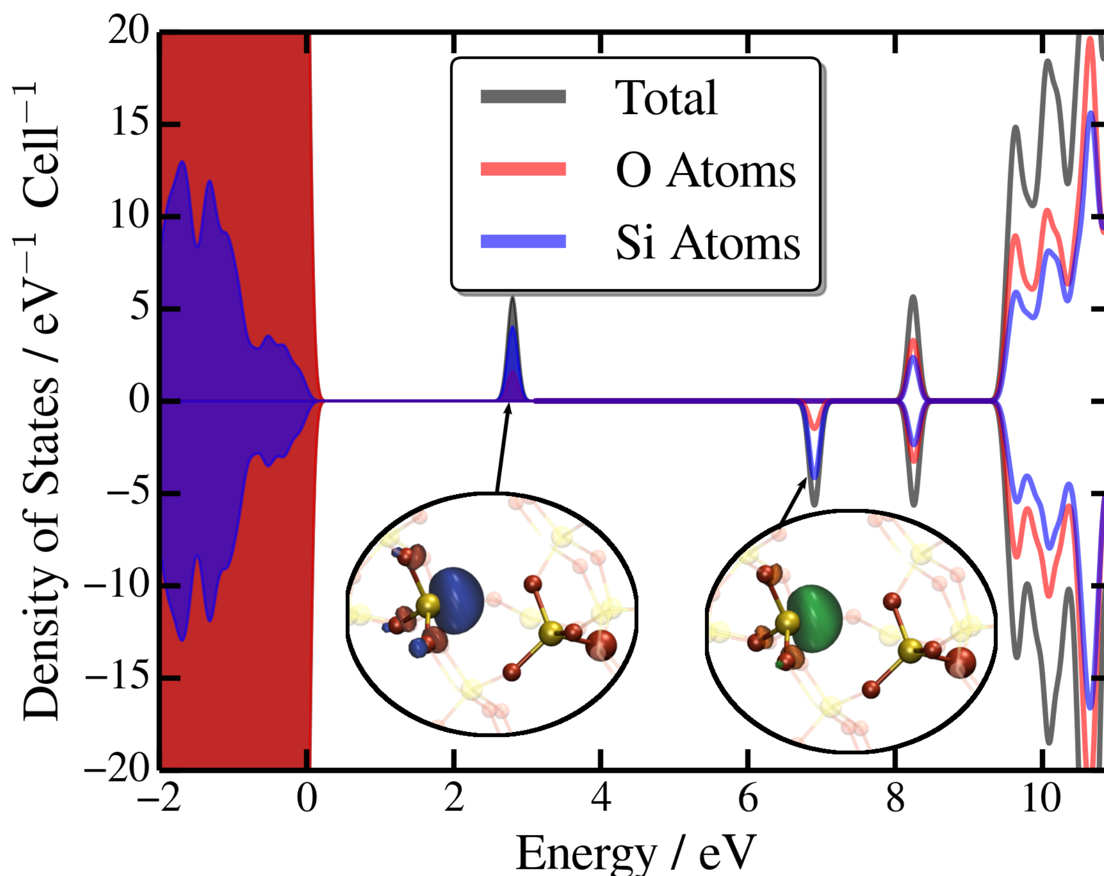

Figure 4.6: Atomic and electronic structure of the puckered configuration of the positively charged oxygen vacancy in α-quartz. The graph shows the electronic density of states, with the positive and negative sections of the y-axis showing the density of α and β electron states, respectively. The HOMO of the α electrons and LUMO of the β electrons are shown in the inset, with the states visualised as red and blue polyhedra for the occupied state, while they are green and orange for the unoccupied state.

Puckered Configuration

As discussed earlier, the puckered configuration of the positive oxygen vacancy is a relaxation of the silicon atom associated with the long Si–O bond through the plane of its oxygen neighbours to benefit from a weak interaction with the oxygen behind it. There is a potential energy barrier between the dimer configuration and the puckered configuration which prevents the puckered configuration from being spontaneously generated by hole trapping at the neutral oxygen vacancy structure. In order to model the puckered configuration and overcome this energetic barrier, a Si atom in the dimer configuration of the positively charged vacancy was manually translated through the plane of its oxygen neighbours, followed by an optimisation using the calculation

details presented in chapter 4.2.1. The structure of the puckered configuration is presented in the insets of Fig. 4.6. The optimisation resulted in a weak bond forming between the Si which has relaxed through the plane of its neighbours, which shall be referred to as Si_B, and there is now no bonding state at all between the two Si atoms. The Si atom which hasn't moved through the plane of its neighbours and which is now 3-coordinated is referred to as the 3c-Si. The calculated spin moments reveal that there is almost no spin density on Si_B which has a spin moment of 1.7×10^{-3}, but is instead almost entirely localised on the 3c-Si with a spin moment of 0.85. The 3c-Si is also much less positive with a Mulliken charge of $+0.86|e|$, while the Si_B has a Mulliken charge of $+1.14|e|$, comparable to the remaining bulk Si atoms' average of $+1.10|e|$, but slightly more positive. The geometry of this configuration is presented in table 4.3 along with a comparison with previous results. The geometry calculated

	This investigation	Blöchl paper [86]	Mysovsky paper [98]
Si_L-Si_S	4.328	4.358	4.320
Si_L-O(3+)	1.881	1.852	1.910
O(3+)-Si	1.812	1.793	1.790
Si_S-O	1.650	1.643	
Si_L-O	1.602	1.599	
All bond lengths are measured in Å			

Table 4.3: Geometry of the puckered configuration of the positive oxygen vacancy in different studies.

agrees excellently with previously published results. The density of states of this puckered configuration shows that the occupied and unoccupied states associated with this defect sit 2.8 and 6.9 eV above the valence band, respectively, revealing that this configuration acts as an effective hole trap. The hyperfine interactions of this unpaired electron's spin with the nuclei around the defect have been calculated. The hyperfine interaction depends upon the spin density at the nucleus, therefore the use of a pseudopotential in place of the core electrons is not applicable. An accurate description of the electrons at the nucleus is required, so it is therefore necessary to describe the core electrons with a basis set. In this calculation, a 6-311G** basis set[99,100] was used on the Si and O atoms and the defect structure was reoptimised

	This investigation	Blochl paper [86]	Mysovsky paper [98]	Experiment [101]
Si_S	-46.45	-45.4	-49.93	-45.31
	-40.31	-39.6	-43.6	-39.07
	-40.30	-39.6	-43.55	-39.06
Si_{S1}	-1.18	-1.4	-1.08	-0.92
	-0.97	-1.2	-0.92	-0.75
	-0.97	-1.2	-0.91	-0.75
Si_{S2}	-1.45	-1.5	-1.16	-0.98
	-1.22	-1.3	-0.99	-0.79
	-1.21	-1.3	-0.98	-0.79
All results are measured in mT				

Table 4.4: Principal values of the hyperfine tensor for the puckered configuration in this model and from previous theoretical and experimental studies. The experimental results are for what is known as the E'_1 centre in α-quartz.

within this basis. This basis led to minimal geometric changes; none of the bond lengths changed by more than 0.05 Å. The hyperfine coupling tensor was calculated and diagonalised to extract the principal values and compare to previous theoretical values and experiment. This is presented in table 4.4. The calculated hyperfine values are in excellent agreement with both previous theoretical calculations and experimental results for what is known as the E'_1 centre in α-quartz.

4.2.3 Negative Oxygen Vacancy

The NOV introduces an unoccupied state which sits below the bottom of the α-quartz conduction band. We investigate whether an electron can be localised in this state. Starting from the optimised configuration of the NOV, we added an electron to the system and optimised its geometry. This resulted in weak atomic displacements in the vicinity of the defect, with the Si–Si bond length remaining at 2.4 Å. However, analysis of the electronic structure reveals that the electron has indeed localized on the Si–Si bond, as shown in the inset of Fig. 4.7. The Mulliken charges of the two Si atoms surrounding the vacancy are +0.62 and +0.74 $|e|$, clearly much more negative than the average of +1.08 $|e|$ for the remaining bulk Si atoms in α-quartz. The extra electron occupies a state which sits 3.0 eV below the bottom of the α-quartz conduction band, as shown in Fig. 4.7. The negative oxygen vacancy's atomic structure is very similar

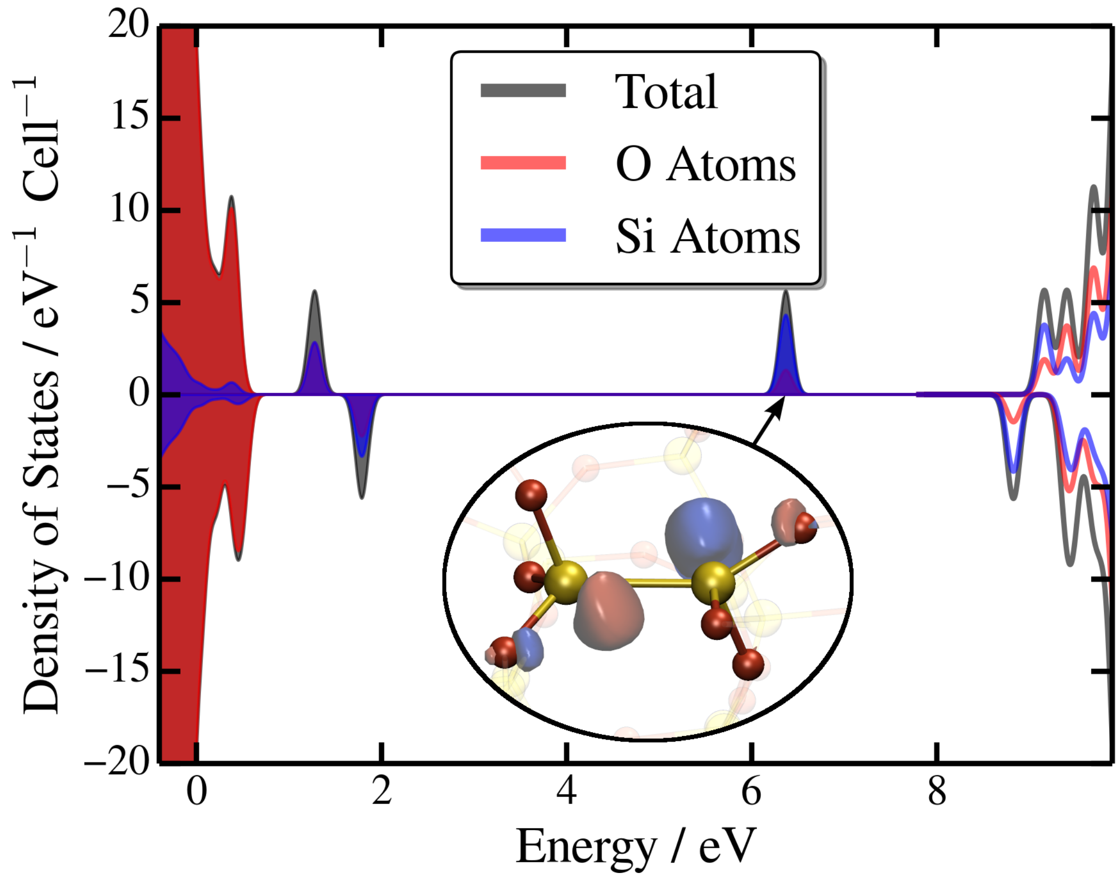

Figure 4.7: Atomic and electronic structure of the negatively charged oxygen vacancy in α-quartz. The highest occupied state in the α channel of electrons is visualised in the inset using an iso-value of 0.1. The defect levels are plotted against the Si–Si length around the negative oxygen vacancy.

to that of the NOV and the dimer configuration of the positively charged oxygen vacancy, but the extra electron is localised in an anti-bonding state between the two Si atoms surrounding the vacancy.

4.2.4 Summary

The oxygen vacancy in α-quartz has been calculated in a number of charge states. Our results for the neutral and positive charge states of the vacancy agree well with previous theoretical and experimental studies in the literature. The unoccupied state of the neutral oxygen vacancy can be occupied by an electron to make the negatively charged oxygen vacancy. All of the vacancy's charged variants are accompanied by strong lattice distortions.

4.3 Amorphous Silicon Dioxide

We now turn to exploring the oxygen vacancy defects in amorphous SiO_2 (a-SiO_2). Due to the similarity in short-range order between α-quartz and a-SiO_2, one can initially explore analogous structures to those presented in the previous section. In fact, the structures of vacancies have indeed been shown to be analogous in a-SiO_2 as well as for other defects such as interstitials.[102,103] In addition, the vacancies in a-SiO_2 have been well studied due to the implication of the positively charged vacancy known as the E′ centre in various reliability issues.[9,84,104,105]

Here, 20 of the a-SiO_2 models generated in chapter 3 were used to study the charged variants of the oxygen vacancy. Unlike crystalline α-quartz where only one model was examined, the vacancy in a-SiO_2 was calculated in 20 different models due to the structural disorder of the amorphous samples. This leads to the defect's properties being spread over a distribution rather than being discrete, requiring it to be studied in a number of different configurations. Initially, the neutral vacancy was studied, followed by its positive and negatively charged variants.

4.3.1 Neutral Oxygen Vacancy

The neutral oxygen vacancy (NOV) in a-SiO_2 was modelled using periodic DFT as described in chapter 2 and using 20 of the a-SiO_2 models constructed in chapter 3. The electrons are again described using the GTH pseudopotentials[90] and double-ζ basis sets (including polarisation functions)[91] while the PBE0_TC_LRC functional[30] exchange-correlation functional[30] was applied with a cutoff radius of 2.0 Å for the Coulomb operator. In each of the 20 models, an O atom was randomly removed from the structure followed by a geometry optimisation. In all of the models, this resulted in the Si atoms surrounding the vacancy displacing towards each other to form an Si–Si bond, analogous to the NOV in α-quartz. However, unlike the NOV in α-quartz, in a-SiO_2 the Si–Si bond length is a distribution which averages at 2.53 Å and has a width of 0.69 Å. The distribution of bond lengths can be seen in Fig. 4.8. These

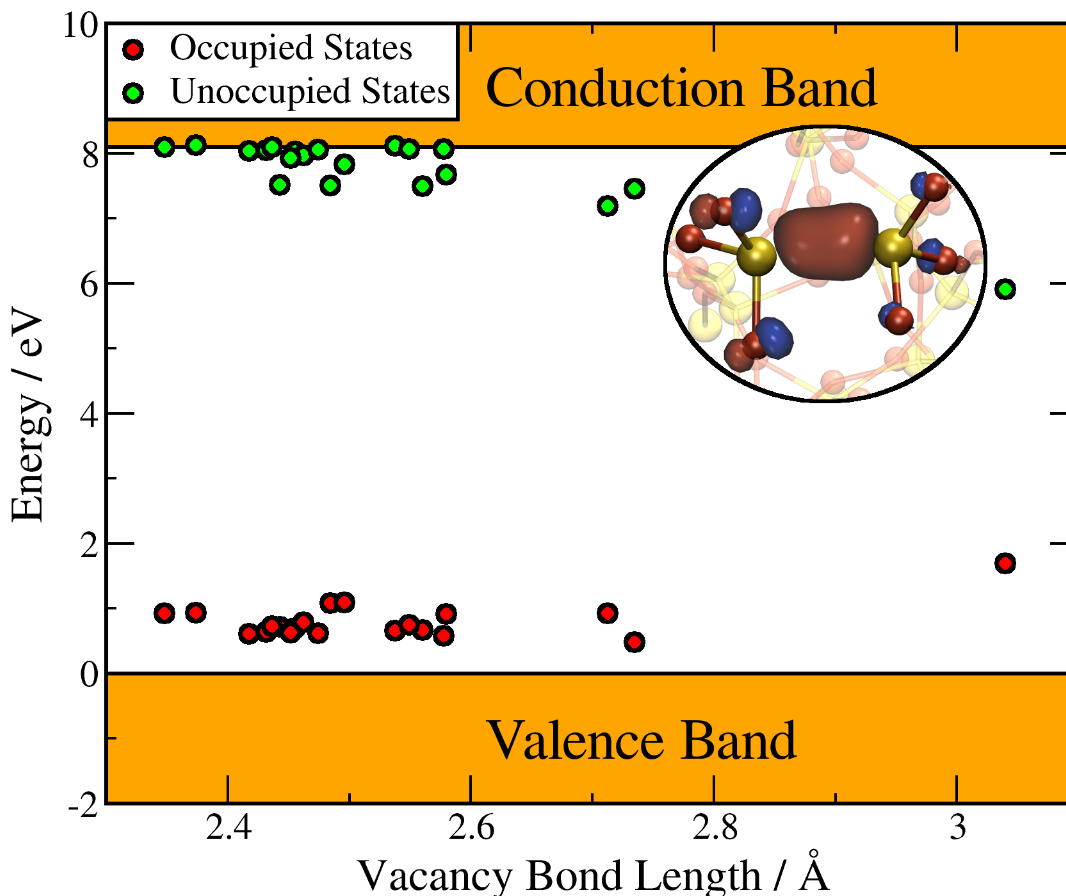

Figure 4.8: Atomic structure and electronic structure plotted against Si–Si bond of the neutral oxygen vacancy in a-SiO_2. The inset shows the HOMO of a single configuration of the NOV. The graph shows the one-electron states associated with the defect plotted against its Si–Si bond length. The shaded in regions indicate the average valence and conduction band edges in a-SiO_2, while the red and green circles represent the occupied and unoccupied defect states, respectively.

results are in good agreement with the results from embedded cluster calculations by Mukhopadhyay *et al.*[59,106]

The NOV introduces a deep occupied state in the a-SiO_2 band gap, similar to that of α-quartz. This state sits on average 0.81 eV above the a-SiO_2 valence band and ranges over 1.02 eV. An unoccupied state associated with the defect breaks off from the bottom of the a-SiO_2 conduction band, sitting on average 0.92 eV below it and ranging across 2.83 eV. The distribution of these states is plotted against the Si–Si vacancy bond length. The defect's occupied states show a weak correlation with the bond length, while the unoccupied states show a weak anticorrelation. Mulliken charge analysis reveals that the Si atoms surrounding the vacancy average at +1.05

$|e|$ and range from +1.0 to +1.10 $|e|$, much more negative than the +1.43 $|e|$ of bulk Si in a-SiO_2. It is interesting to note that the charges of the two Si atoms surrounding the vacancies display a random asymmetry, that is there is no predictable way of determining whether one Si will be more or less negatively charged than the other Si making up the vacancy.

4.3.2 Positive Oxygen Vacancy

The positively charged oxygen vacancy was studied in 20 different a-SiO_2 models. Starting from the NOV configurations described in the previous section, a hole was added to each of the 20 systems and their geometries were optimised. In all configurations, this resulted in a significant displacement of the Si atoms surrounding the vacancy so that the average distance between them is 3.16 Å, ranging between 2.7 and 4.3 Å away from each other. The Si–O bonds of these Si atoms averages at 1.58 Å, slightly shorter than the average Si–O bond length of 1.61 Å in a-SiO_2. The atomic structure of these configurations are analogous to the dimer configuration of the positive oxygen vacancy in α-quartz. The unpaired spin is localised between these two Si atoms, with their Mulliken spin moments averaging at 0.43 and ranging from 0.34 to 0.59. Their average Mulliken charge is +1.49 $|e|$ and ranges from +1.47 to +1.51 $|e|$. The narrow range of the Mulliken spin moments and charges indicates that both Si atoms surrounding the vacancy are very similar.

The positive oxygen vacancy possesses an occupied one-electron state in the α-channel of electrons that sits on average 1.0 eV above the valence band. However, it shows a wide distribution ranging over 2 eV with a strong dependence on the Si–Si distance of the two Si atoms surrounding the vacancy, shown in Fig. 4.9. The hole introduced into the β-spin channel of electrons localises on a state which sits deep in the a-SiO_2 band gap, on average 3.8 eV above the valence band, and its position also shows a strong dependence on the Si–Si distance.

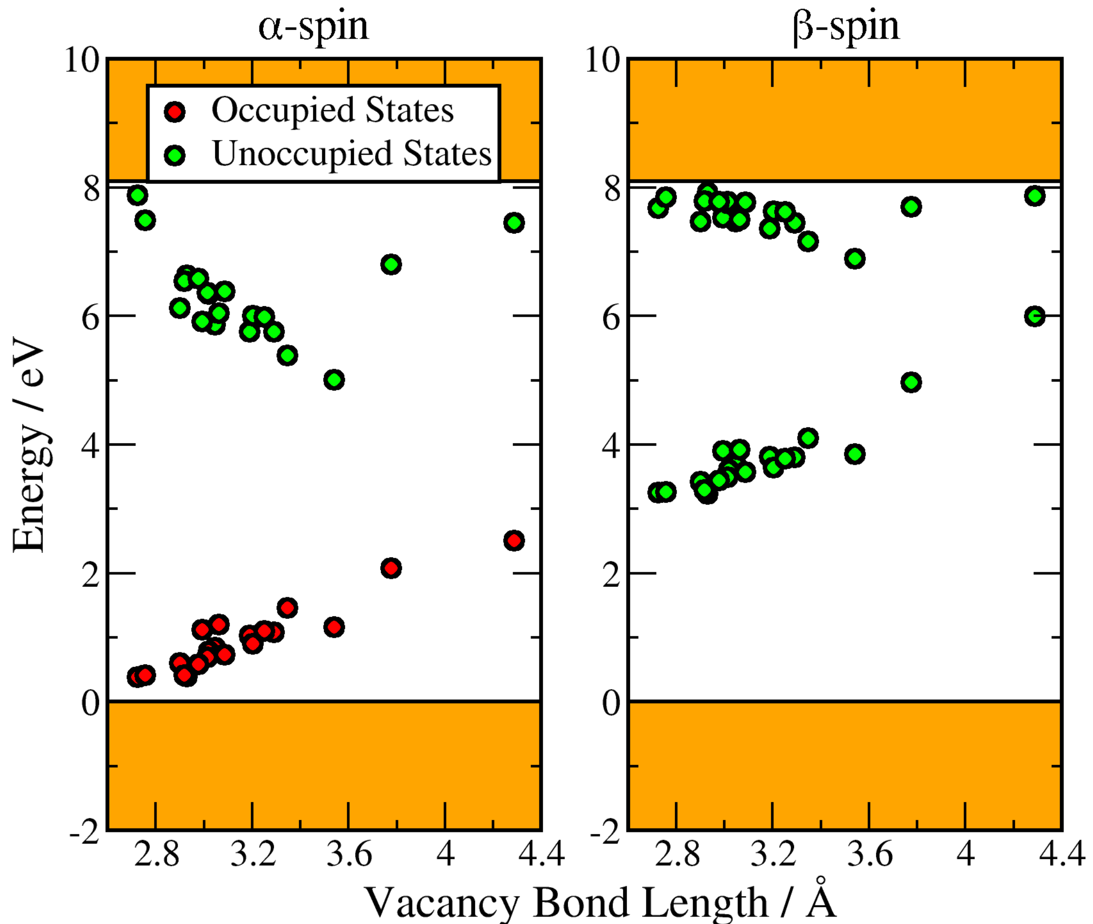

Figure 4.9: One-electron level of the positive oxygen vacancy in a-SiO_2 plotted against the Si–Si length of the Si atoms surrounding the vacancy. The left panel shows the states from the α spin channel while the left panel shows the β spin states. The red circles are the occupied and the green circles are the unoccupied states. The average of the bands and their edges are coloured in orange, with the valence band at the bottom and the conduction band at the top.

4.3.3 Singly Negative Oxygen Vacancy

To model the negatively charged vacancy, a single electron was added to each of the 20 neutral oxygen vacancy configurations described in section 4.3.1. This resulted in a strong local distortion around the vacancy, with the Si–Si bond extending to an average of 3.1 Å, similar to the positive oxygen vacancy. The range of bond lengths, however, is much narrower for the negatively charged vacancy, ranging over 0.3 Å. The average Mulliken charge of the Si atoms surrounding the vacancy drops to an average of +0.98 $|e|$, ranging from +0.8 to +1.1 $|e|$, suggesting that these Si sites are more negatively charged than the average Si in bulk a-SiO_2. The unpaired spin is highly localised between these two Si atoms, with their average Mulliken spin

moment averaging at 0.46 and ranging from 0.24 to 0.72. The broad distribution of Mulliken spin moments suggests that the electron has a tendency to localise at one of the Si sites around the vacancy. However, there is no clear correlation to suggest at which Si site the electron would localise. The calculated one-electron levels for the

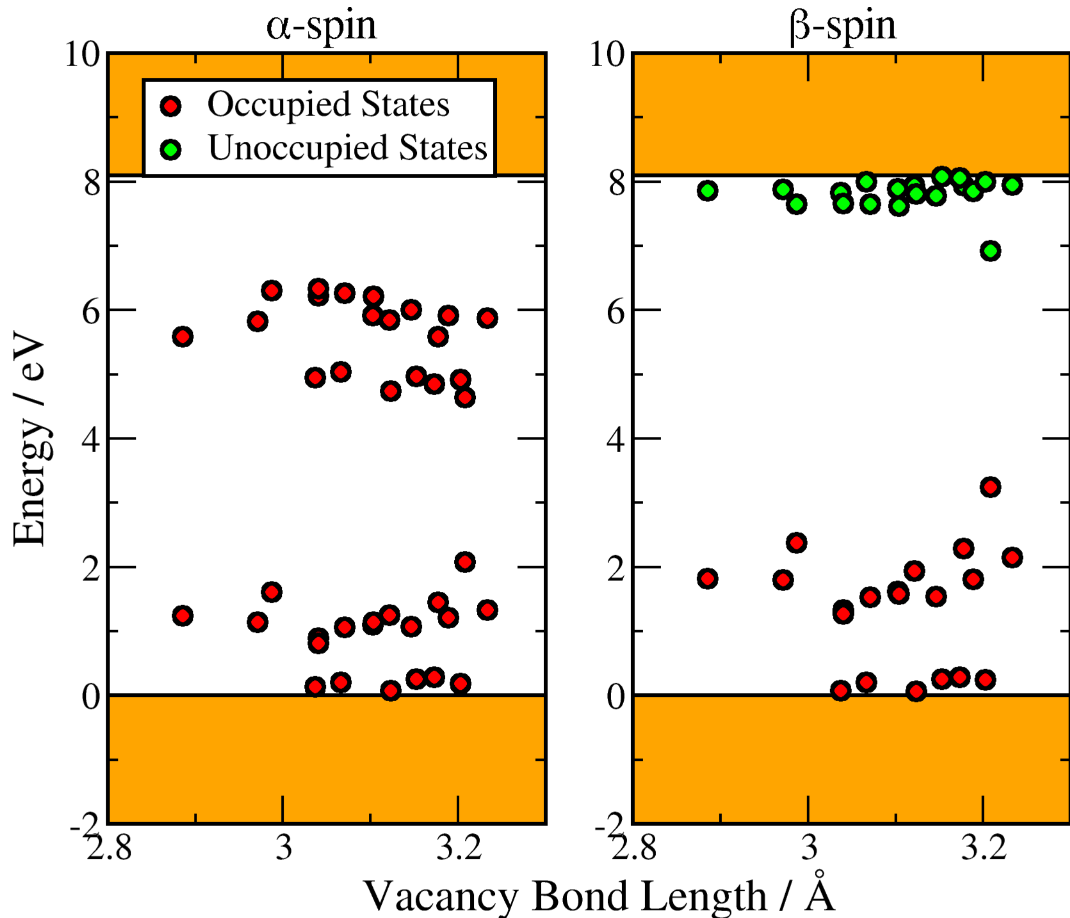

Figure 4.10: One-electron level of the negative oxygen vacancy in a-SiO_2 plotted against the Si–Si length of the Si atoms surrounding the vacancy. The left panel shows the states from the α spin channel while the left panel shows the β spin states. The red circles are the occupied and the green circles are the unoccupied states. The average of the bands and their edges are coloured in orange, with the valence band at the bottom and the conduction band at the top.

20 configurations of the negative oxygen vacancy are plotted against their respective Si–Si bond lengths in Fig. 4.10. Unlike the positive oxygen vacancy, there is no strong correlation of the defect's one-electron level with the Si–Si bond length. The addition of an electron into the α-channel of electrons localises an occupied state which sits deep in the a-SiO_2 band gap, averaging at 4.1 eV above the valence band and shown on the left panel of Fig. 4.10. Visualisation of this occupied state indicates that the

electron now occupies an anti-bonding orbital between the Si atoms surrounding the vacancy, explaining the extension of the Si–Si bond relative to the neutral oxygen vacancy.

4.3.4 Summary

The oxygen vacancy has been calculated in 20 models of a-SiO_2. The structures of these vacancies are analogous to their counterparts in crystalline α-quartz. However, due to the disorder inherent to the amorphous structures, the defect's structural and electronic properties can be highly dependent on their respective local chemical environments.

4.4 Discussion

The oxygen vacancy has been modelled in both α-quartz and a-SiO_2 in a number of charge states. The first thing to note is that the vacancies modelled here in α-quartz show analogous structures in a-SiO_2. Although this is true of these models, this result should not be extrapolated to the conclusion that all defects in α-quartz have analogues in a-SiO_2. Due to the disorder inherent to the amorphous structures, the defect's structural and electronic properties can be highly dependent on their respective local chemical environments, unlike their counterparts in α-quartz.

Having calculated the vacancy in its various charge states, we can examine their thermodynamics. The formation energy of the vacancy from bulk SiO_2 was calculated according to equation B.1 in the appendix. Fig. 4.11a shows the formation energies of the vacancy in α-quartz plotted against the Fermi Level of the system, with zero set as the top of the α-quartz valence band. We find that the neutral configuration is thermodynamically stable over a limited range of Fermi energies, between ≈ 4.0 and 5.5 eV. The formation energies of the vacancy in a-SiO_2 have also been calculated. Instead of plotting the formation energies of each vacancy, it can be instructive to inspect their thermodynamic switching levels; the Fermi level at which the formation

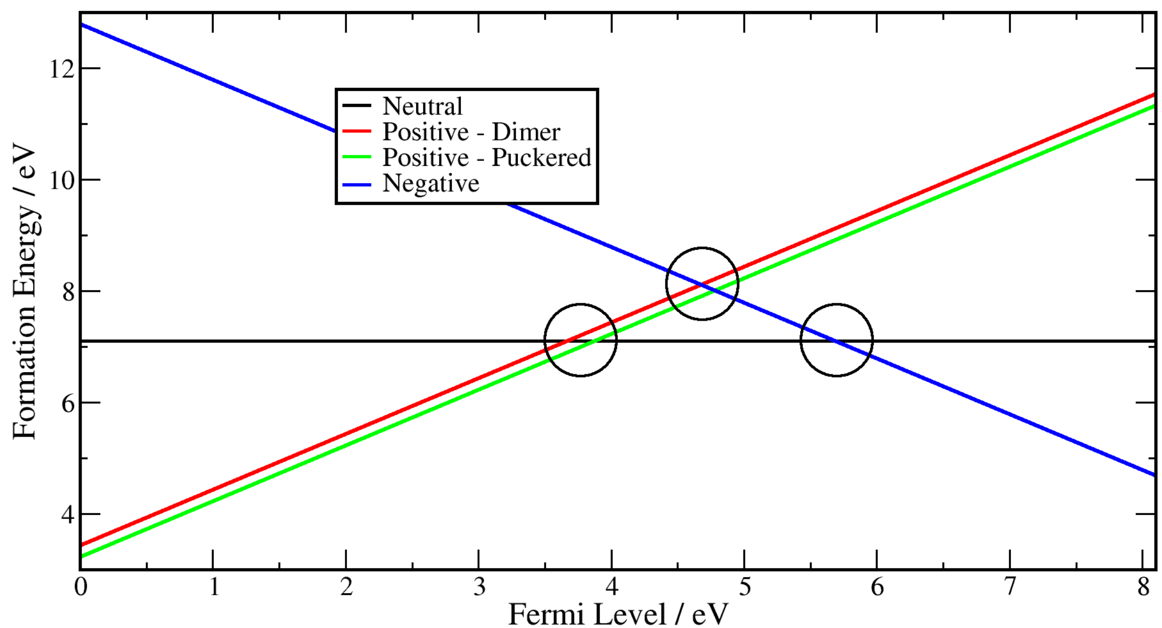

(a) Formation energy plotted against the Fermi level for the oxygen vacancy in α-quartz. The straight black line is the neutral charge state, the red and green lines are the dimer and puckered configurations of the positively charged vacancy, respectively, while the blue line is the negative charge state.

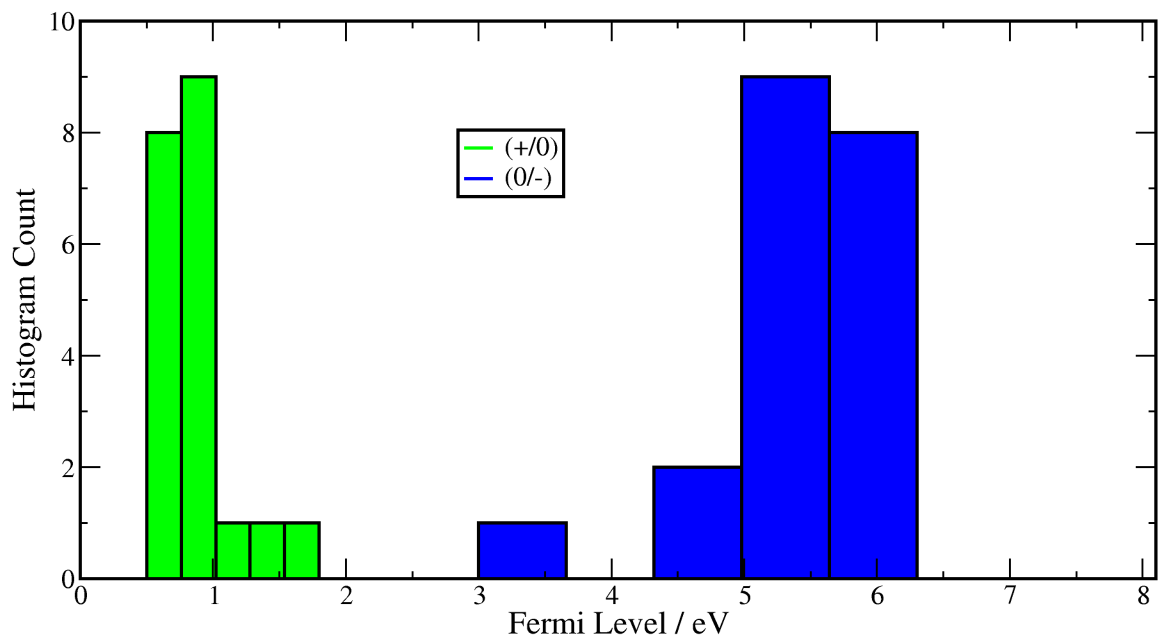

(b) Histogram of the thermodynamic switching levels of the oxygen vacancy in a-SiO_2 plotted against the Fermi level. The (+/0) switching level is coloured in green while the (0/-) switching level is coloured in blue.

Figure 4.11: Thermodynamics of the oxygen vacancy in α-quartz and a-SiO_2.

energy of a defect in two different charge states is equal, as indicated by the circles in Fig. 4.11a. These are plotted in a histogram for all 20 configurations of the a-SiO_2 vacancies studied and is shown in Fig. 4.11b. It is clear to see that the switching levels are distributed over a range of Fermi levels, in contrast to the discrete switching levels of the vacancy in α-quartz. The (+/0) switching levels occur at a much lower Fermi level in a-SiO_2 than in quartz, but the (0/-) level occurs at around the same Fermi level. These switching levels indicate that the vacancy can be thermodynamically stable in the neutral charge state over a wide range of Fermi levels ranging from 0.6 to 6.1 eV, although it is not necessarily the same defect configuration that is stable over this range. In contrast, the vacancy in α-quartz is thermodynamically stable in the neutral charge state over a relatively limited range of Fermi levels, from 4.0 to 5.6 eV. This would make the neutral oxygen vacancy dominant in an Si/SiO_2 system (c.f. Si/SiO_2 band offset[107]), regardless of whether the SiO_2 is in the crystalline or amorphous state. However, when the Fermi level is set to the top of the valence band, the positive charge state is dominant by far while the negative charge state is most stable when the Fermi level is set to the bottom of the conduction band.

5

Electron Trapping at Impurities in Silicon Dioxide

5.1 Introduction

Having reviewed the well known oxygen vacancy defects and their charge trapping states in SiO_2, we now turn our attention to electron trapping at impurities. Silicon dioxide (SiO_2) is a material that is of fundamental importance to a number of technologies. Quartz, the most stable crystalline polymorph of SiO_2, is widely utilized in optical devices due to its high melting temperature and transparency to visible and UV radiation. Electron trapping is known to have a dramatic effect on the performance and reliability of these devices. For example, quartz, which is normally clear

and transparent to visible radiation, becomes coloured upon irradiation at higher energies.[108] The colouration is thought to be due to electrons trapping at localized impurity sites throughout the structure. These trapped electrons absorb throughout the electromagnetic spectrum and will therefore affect any radiation passing through the sample. These interactions can attenuate the signals passing through the structure and are therefore usually undesirable properties.

So far, the dominant electron traps in quartz have been associated with impurity-related centres. It has been well established, both experimentally and theoretically, that electrons can be trapped by Ge impurities substituting for Si in both α-quartz[16,109] and in a-SiO_2,[85] with experimental models of these centres recently revisited by Griscom.[110] Pacchioni *et al.*[16] calculated a germanium substitution in a silica cluster (with fixed hydrogen atoms terminating the cluster) representative of α-quartz; the cluster used was a $H_{12}O_{16}Si_4Ge$ cluster. DFT was employed with the exchange and correlation described by the hybrid B3LYP functional.[35,111] The orbitals on Ge and the first O and Si neighbours were described by a 6-31 G basis set while the rest of the Si and O atoms were described by a 3-21G basis set. The cluster was terminated by hydrogens described by a MINI-1 basis set. They showed that electrons can indeed be trapped at Ge impurities in SiO_2 in a deep, localized state. The electron trapping is accompanied by a strong structural relaxation.

Ge dopants in Si-based technologies have come back into the fore due to a number of technological advances. The use of SiGe alloy materials has allowed the discovery of new, advanced electronic devices and has improved the performance of existing Si devices.[112] The structure of a SiGe device is formed by implantation of Ge into Si followed by oxidation. The native oxide formed is mainly SiO_2 due to the highly negative free energy of formation of SiO_2, which is much more negative than that of GeO_2, rejecting the Ge and forming a sharp Ge rich layer at the interface.[113] Nonetheless, several studies have investigated the concentration of Ge in the native oxide under various processing conditions.[114–116] It is found that Ge persists in the oxide, and that the Ge present in the oxide exists as GeO_2, not as elemental Ge

clusters which were originally thought to exist due to the processing conditions.[117] Therefore it is important for us to understand the charge trapping properties of Ge impurities in SiO_2.

In addition, a trapped electron has been observed in α-quartz containing Li impurities using ESR.[118] It is formed after a double irradiation, with the second irradiation thought to trap an electron at the free Li ion. Analysis of the experimental conditions and the ESR parameters obtained indicates that the electron is in fact trapped at a four-coordinated Si site while the Li ion resides nearby and stabilizes the trapped electron. Although this defect has been identified experimentally, there is no theoretical model of this defect centre reported in the literature.

In this chapter, we investigate electron traps at Ge and Li impurity sites in α-quartz. An atomistic defect model is developed for each impurity and they are contrasted against each other. The structure of these electron traps is found to be qualitatively very similar. Finally, each model is compared to experimental data.

5.2 Calculation Details

All calculations discussed in this chapter were performed in a $3 \times 3 \times 3$ supercell of α-quartz whose structure was obtained from a crystal database.[119] This supercell was then optimized in the neutral, spin singlet charge state using DFT implemented in the CP2K code,[27] as discussed in chapter 2. The non-local functional PBE0_TC_LRC was used in all calculations with a cutoff radius of 2.0 Å for the truncated Coulomb operator.[34] Inclusion of Hartree-Fock exchange provides a more accurate calculation of the band gap compared to the semi-local functionals such as PBE. It also better describes localized states that may be involved in charge trapping processes such as those studied in this chapter. The CP2K code uses a Gaussian basis set with an auxiliary plane-wave basis set.[25] The Gaussian basis set employed for all atoms was a double-ζ basis set with polarization functions[91] in conjunction with the Goedecker-Teter-Hutter (GTH) pseudopotential.[90] Calculating hyperfine interactions necessitated the use of

all electron basis sets using the Gaussian and augmented plane-wave (GAPW) approach. The basis sets with contraction schemes of (8831/831/1),(8411/411/11) and 6-311G** were used for silicon,[120] oxygen[121] and Li,[122] respectively. The plane wave cut-off was set to 5440 eV (400 Ry). In order to reduce the computational cost of calculating the Hartree-Fock exchange terms, an auxiliary basis set was used as described in chapter 2.3.2. This auxiliary basis set is a much sparser Gaussian basis set containing less diffuse and fewer primitive Gaussian functions than the full basis set employed in the rest of the calculation. This allows the Hartree-Fock exchange terms, whose computational expense scales to the fourth power of the number of basis functions, to be calculated on a much smaller basis set than the rest of the calculation and therefore much faster. The pFIT3 auxiliary basis set was used for the Li, Si and O atoms, with the Hartree-Fock exchange terms calculated using a full basis set on the Ge atoms.

All geometry optimizations were performed using the Broyden-Fletcher-Goldfarb-Shanno (BFGS) optimizer to minimize forces on atoms to within 37 pN (2.3×10^{-2} eV Å^{-1}). After optimization in the neutral charge state, a single Si atom in the cell was substituted for a Ge atom and optimized again to create the Ge-doped α-quartz model. To create the Li-doped quartz models, no Si atoms were substituted but an Li interstitial was instead added to the system. One extra electron was then added to the Ge-doped system along with a background positive charge that is uniform across the entire cell while the cell containing the Li interstitial was charge neutral. The optimization resulted in the electron trapping centres in these systems.

In order to check the convergence of each defects' properties, the electron trapping centres were also modelled in α-quartz cells containing 576 atoms. However, the results reported in this chapter are for the cells containing 243 atoms. The results for the larger cells have not been included as they are consistent with those obtained in the smaller cells, indicating that the 243 atom cells of α-quartz are sufficient for this study. Barriers between configurations were calculated using CI-NEB (see chapter 2.6). Linear interpolation was used to generate 10 images which made up the band

to be optimized with each of the images connected by a spring with a force constant of 2 eV Å^2.

The calculated energies were corrected, where necessary, for the interaction between the charged defects using the method of Lany and Zunger,[123,124] described in equation B.2 in the appendix.

5.3 Results of calculations

5.3.1 Ge-doped α-quartz

The first centre that was studied was the electron trapping at Ge impurities in α-quartz.[109] The model of this centre has been developed both experimentally and theoretically, with it first being characterized by Weil *et al.* using ESR,[109] and reviewed recently by Griscom.[110] The experimental characterization of electrons trapped in Ge-doped α-quartz reveals two distinct defects: the Ge(I) and Ge(II) centres.[109,125] It has been suggested that both these defects reside on the same GeO_4 tetrahedron in α-quartz and a-SiO_2, with the Ge(I) centre assigned as the ground state.[109,110] The energy difference between these two defect centres was measured as 0.0025 eV at 15 K and 0.0078 eV at 300 K.[109] On the theoretical side, cluster calculations by Pacchioni *et al.* of what he called the Ge electron centre (GEC) have demonstrated that a four-coordinated Ge atom in silica can trap an electron. This is accompanied by an orthorhombic distortion of the pseudo-tetrahedral Ge centre which results in two short and two long Ge–O bonds.[16]

Here, we use the same terminology as Pacchioni and calculate the GEC in α-quartz. Calculations were performed in 243 atom periodic cells of α-quartz with one Si atom substituted for Ge. Geometry optimization in the neutral charge state maintains the tetrahedral coordination of the Ge impurity, similar to the remaining Si atoms in bulk α-quartz. However, the Ge–O bonds are slightly longer than its Si counterpart, with two long (1.74 Å) and two short (1.73 Å) Ge–O bonds and O–Ge–O angles of $\approx 109°$. The Ge introduces an unoccupied state which sits below the bottom of the α-quartz

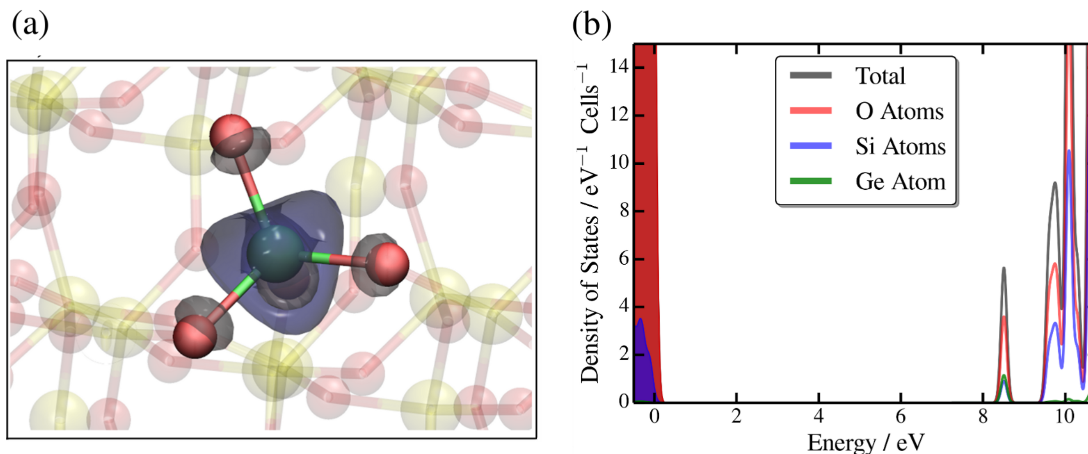

Figure 5.1: a) The molecular orbital associated with the lowest unoccupied state in Ge-doped α-quartz. It is strongly localized on the Ge impurity and its neighbours. The isovalue of the density surfaces is 0.02. b) The density of states of neutral Ge-doped quartz is shown underneath the structure. An unoccupied state which is high in Ge and O character sits below the bottom of the conduction band.

conduction band and is highly localized on the Ge atom and its neighbours, as can be seen in Fig. 5.1a. The calculated one-electron band gap of α-quartz is 8.6 eV. The empty state sits 0.8 eV below the bottom of the conduction band and projection of the density of states onto the individual atoms further confirms that the state is highly localized on Ge and O atoms (see Fig. 5.1b). The neutral Ge atom has a Mulliken charge of +1.76 $|e|$ in α-quartz.

An extra electron was then added to this cell to make the GEC. It initially occupied the localized, empty state on the Ge atom. The Coulombic interaction between the extra electron and its slightly negatively charged O neighbours repels them away in order to lower the total energy of the system. This results in an opening of the O–Ge–O angle formed by the longer Ge–O bonds which in turn localizes the electron further on the Ge atom. The two long Ge–O bonds elongate by 0.2 Å, becoming 1.9 Å, and the O–Ge–O angle opened up to 150°. The remaining two short Ge–O bonds extended slightly, up to 1.8 Å. The bond lengths and angles of the negatively charged GEC centre are asymmetric, similar to the Ge impurity in the neutral charge state. The spin density is strongly localized on the Ge atom and its oxygen neighbours (see Fig. 5.2a), with the Ge atom possessing a Mulliken spin moment of 0.72. The Mulliken charge of the Ge atom is now +1.33 $|e|$, about 0.43 $|e|$ lower than in the

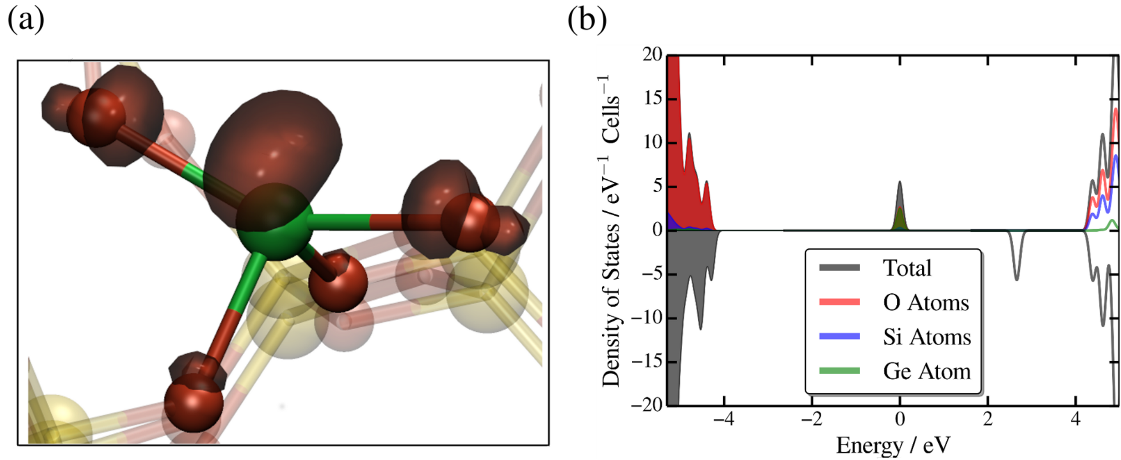

Figure 5.2: a) The spin density of the negatively charged Ge-doped α-quartz with the spin density localized on the Ge centre and its neighbours. The isovalue of the density surfaces is 0.02. b) The density of states of the negatively charged Ge centre in quartz. An occupied state sits deep in the band gap and is high in Ge character.

neutral system. The optimization results in the occupied one-electron defect level sitting 4.1 eV below the conduction band, as can be seen in Fig. 5.2b. The relaxation energy of the system (i.e. the total energy difference between the system with the electron at the bottom of the conduction band and the final structure) is 1.51 eV.

As mentioned above, it has been suggested that the Ge(I) and Ge(II) electron spin resonance (ESR) signals can result from the electron trapping on the same GeO_4 tetrahedron.[110] Calculations were made to check whether an electron could localize in different configurations on the same GeO_4 tetrahedron by creating initial configurations that would favour these metastable states. In particular, the five remaining O–Ge–O angles were opened on the same GeO_4 tetrahedron described above to see if an electron can localize on each O–Ge–O different angle in the tetrahedron. This was accomplished by manually displacing the two neighbouring O ions of the original, ideal GeO_4 tetrahedron to create an electron trapping precursor. The two Ge–O bonds associated with the displaced O atoms were 1.9 Å and the angle between them was somewhere between 150° and 160°. The geometry of these systems, each containing a newly opened O–Ge–O angle, were then optimized in the negative charge state. Energy minima associated with all 5 remaining combinations of Ge–O bond pairs were found. Their relaxation energies range between 1.36 eV to 1.51 eV. The

Mulliken charges of all the Ge atoms are lower than in the neutral system, ranging from +1.34 to +1.38 $|e|$. These results suggest that an electron can indeed localize on the same GeO_4 tetrahedron Ge doped α-quartz in six different configurations.

All six configurations show qualitatively similar geometries: elongation of two Ge–O bonds and the opening of O–Ge–O angle between them. However, there are quantitative differences in the extent of O–Ge–O angle opening which ranges from 132° to 150°. The electronic density of states of all six configurations shows an occupied one-electron level that sits 4.31 eV on average below the bottom of the α-quartz conduction band with a distribution of 0.1 eV. The relative energies of the six different configurations are plotted with respect to the O–Ge–O angle in Fig. 5.3. A general trend can be seen; the lowest energy configuration has the widest O–Ge–O angle and smaller O–Ge–O angles result in higher total energies. The smaller O–Ge–O angles are due to the different local environments that each O–Ge–O angle exists in. The α-quartz unit cell is not highly symmetric with each O–Ge–O angle being in a unique chemical environment. Due to this, some of the O–Ge–O angles have larger space to relax into.

The isotropic hyperfine splitting constants were calculated for all six configurations of the Ge electron centre. The splitting due to the interaction between the Ge^{73} nucleus ranges from -26.325 mT to -31.19 mT, with the lowest energy structure possessing an isotropic hyperfine constant of -29.17 mT. The calculated values are in the range of the experimental values of -28.47 mT and -28.956 mT reported by Isoya *et al.* for the Ge(I) and Ge(II) centres.[109] Although it was found that an electron can localize on the same GeO_4 tetrahedron, the structure of the Ge(II) centre cannot be correlated with any of the structures. More accurate calculations of the hyperfine splittings would be needed in order to conclusively identify the atomic structure of the Ge(II) centre.

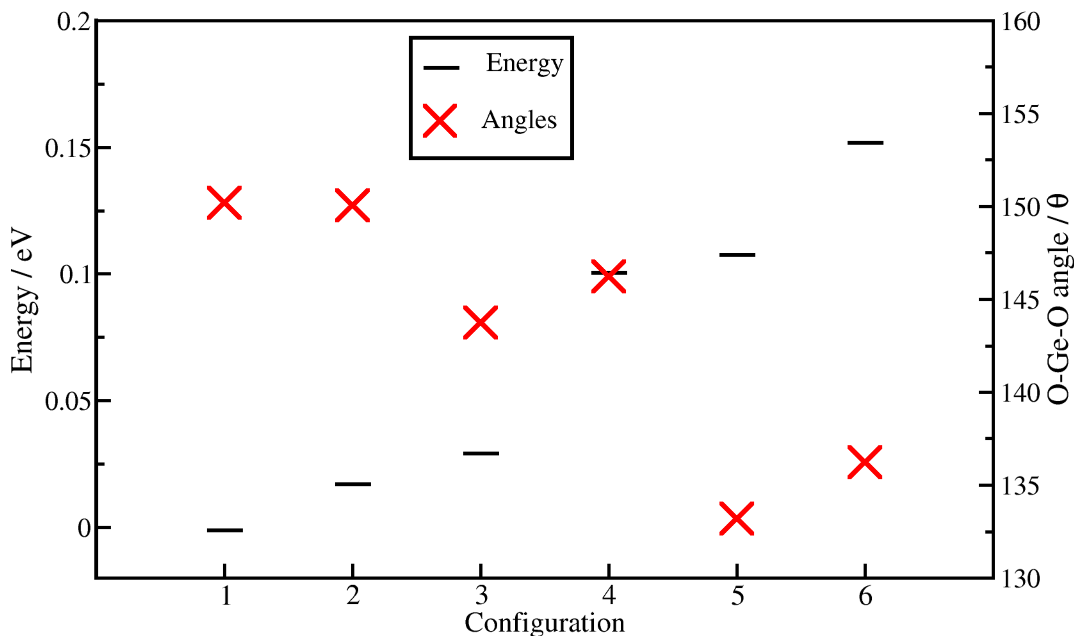

Figure 5.3: Energies of the six different electron trapping configurations in Ge-doped α-quartz plotted alongside the O–Ge–O angle. The energies are shown on the left hand side y-axis and marked as black lines on the graph, while the O–Ge–O angles are shown on the right hand side y-axis and marked on the graph as red crosses.

5.3.2 Li-doped α-quartz

Jani *et al.* experimentally studied the effect of Li impurities in α-quartz,[118] particularly properties of the $[AlO_4/Li]^0$ centres. A Li electron centre in quartz was found to be formed by a two-step irradiation process. The first irradiation step performed at 150-300 K moves the Li away from its Al counterpart.[126] The second step, performed after cooling the quartz sample down to 77 K, forms a $[SiO_4/Li]^0$ centre. The ESR spectrum of this centre shows splittings of 0.09 mT from a ^7Li and 40.47 mT from a ^{29}Si. This centre was found to be stable below 180 K and has been characterized by Jani *et al.* as an extra electron trapped at a four-coordinated Si site with an adjacent Li^+ ion providing stability.[118] This model has been supported by early molecular cluster calculations by Wilson *et al.*,[127] but no further calculations have been carried out to confirm the structure of this defect.

In this chapter, we attempt to further elucidate the structure of the electron trap in Li-doped α-quartz. In these calculations, a Li atom was added to a 3x3x3 supercell of α-quartz and the geometry of the system was optimized in the neutral charge state

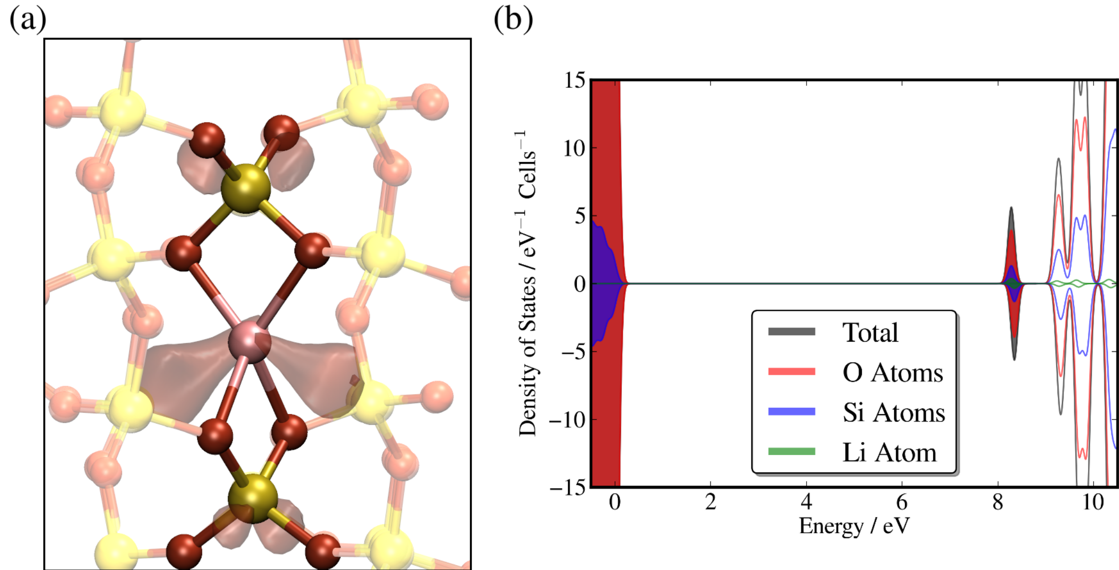

Figure 5.4: a) Spin density of a Li interstitial atom in α-quartz. The spin density is highly localized on the Li atom and its surrounding Si neighbours. The isovalue used to plot this surface was set to 0.02. b) The density of states associated with the interstitial Li in α-quartz. An occupied state sits just below the bottom of the α-quartz conduction band and is highly localized on the Li atom as well as the Si and O atoms.

initially. The Li atom occupies an interstitial position in the α-quartz lattice, as can be seen in Fig. 5.4a, with a one-electron level sitting $\approx$ 1.5 eV below the bottom of the α-quartz conduction band shown in Fig. 5.4b. It sits in an α-quartz channel between four O atoms, the nearest neighbours sitting 1.96 or 1.98 Å away. The Li remains rather neutral with a Mulliken charge of +0.2 $|e|$. The spin density is highly localized on the Li centre with a Mulliken spin moment of 0.75. These results indicate that the interstitial Li remains atomic in nature with no electron transfer taking place. The average Mulliken charge of the Si atoms in this model is +1.44 $|e|$, ranging from +1.40 to +1.49 $|e|$.

Inspired by the opening of the O–Ge–O angle in Ge-doped α-quartz, perturbation of the lattice in a similar manner to the Ge electron trap was investigated to see if it would induce electron transfer from the Li atom to nearby O–Si–O angles. An O–Si–O angle of one the nearest Li interstitial's neighbours was opened in a manner similar to the O–Ge–O described above. Relaxing the structure results in an electron transferring from the Li atom and localizing on the perturbed O–Si–O angle, as shown

in Fig. 5.5a. The relaxed structure has an extended O–Si–O angle of 150° while the Li ion is located 2.62 Å away from the Si centre, bound to the two O neighbours, which are not associated with the O–Si–O angle opening. The spin density plot of the system in Fig. 5.5a shows that the unpaired spin is mostly localized on the Si atom (in the open O–Si–O angle) and two of its oxygen neighbours. Mulliken population analysis reveals that the Li now has a charge of +0.49 $|e|$ while the Si at the centre of the wide O–Si–O angle has a Mulliken charge of +1.1 $|e|$. The Mulliken charge of Si ions in quartz is +1.43 $|e|$, indicating that the Si has gained negative charge. The Mulliken spin moment of the Li atom is now reduced to 0.04 while the spin moment on the Si is 0.86.

The Li^+ ion is stabilized by its interaction with the lone pairs on its oxygen neighbours. The total energy of the Li stabilized electron centre is 0.28 eV lower than that of the Li interstitial atom in α-quartz, i.e. the trapping energy of the Li stabilized electron centre is 0.28 eV. The small trapping energy reflects the fact that the initial state is already a fairly deep electron trap.

The barrier for transferring an electron from the atomic Li to the Si ion was calculated using the CI-NEB method, described in chapter 2.6. Starting with the interstitial as the initial configuration and the electron trapping state as the final configuration, a band was set up by interpolating between these two points and was subsequently optimized. The barrier was found to be 0.68 eV. De-trapping from this state requires overcoming a barrier of 0.96 eV. The occupied one electron state of the unpaired electron is located 3.1 eV below the bottom of the quartz conduction band (see Fig. 5.5b). This demonstrates the stabilizing role of the Li^+ ion in creating the $[SiO_4/Li]^0$ electron centre.

The calculated hyperfine splittings due to the interaction of the unpaired electron with the surrounding nuclei were calculated and are shown in Table 5.1. They are also compared with the experimental results by Jani *et al.*[118] in that table. The strongest hyperfine interaction is with the ^{29}Si ion, with an isotropic hyperfine splitting of 43.07 mT. Smaller hyperfine splittings come from the ^{7}Li ion and on the ^{17}O neighbours.

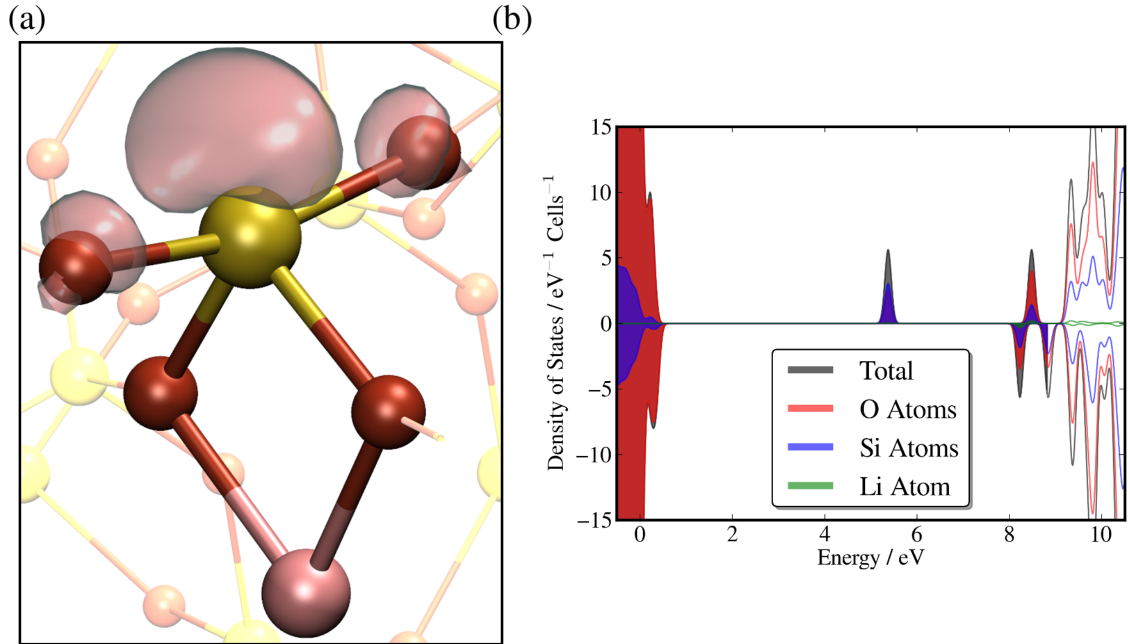

Figure 5.5: a) Spin density of the electron trapped at an Si atom from an Li impurity. The spin is highly localized on the Si atom and its O neighbours. Isovalue of the density plot is 0.015. b) Density of states of the electron trap. An occupied state sits deep in the band gap and is high in Si and O character.

Signal	Theory	Experiment [118]
a_{iso} Si	43.07	40.47
a_{iso} Li	0.11	0.09
Principal values	0.089	0.088
	0.096	0.098
	0.16	0.15

Table 5.1: Hyperfine splittings and principle values of the hyperfine tensor (in mT) of the Li electron trap in α-quartz. The experimental values of hyperfine interactions for the Li-doped quartz are shown for comparison.

These results are in excellent agreement with experiment, as can be seen in table 5.1.

To summarize, an Li impurity in α-quartz can lead to an electron being trapped at an Si atom in a similar manner to the Ge electron trap in α-quartz. A common feature of both centres is that the electron is highly localised on either Ge or Si ion and is accompanied by an energy gain, elongation of two metal-oxide bonds and a significant opening of the –O–(Ge)Si–O– angle.

5.4 Discussion and Conclusions

These calculations demonstrate the qualitatively similar character of electron localization for two impurities in crystalline SiO_2. In α-quartz, a substitutional Ge atom provides a local structural perturbation which facilitates the localization of an extra electron at the Ge site. For the first time, the atomistic structure of the $[SiO_4/Li]^0$ centre has been calculated, showing that a Li atom in α-quartz donates an electron to a neighbouring Si ion and further stabilizes the defect state by the Coulomb interaction between the trapped electron and the Li^+ ion. In both cases, the electron localization on Ge and Si ions is facilitated by the opening of the O–Si(Ge)–O angle. The electron localization in pure bulk α-quartz requires opening O–Si–O angle from 109° to 134°, but introducing this distortion costs 0.57 eV.

It is interesting to note that the experimentally measured ESR signal of the $[SiO_4/Li]^0$ centre in Li-doped α-quartz is reduced to zero at around 180 K.[118] The calculated barrier for de-trapping is rather high at 0.96 eV, suggesting that it is perhaps not the electron transferring back to the Li atom which is responsible for the disappearance of the ESR signal. As mentioned earlier in this section, the interaction between the trapped electron and the Li ion provides a stabilizing Coulomb potential well for the trapped electron. As all the Si ions in α-quartz are equivalent, diffusion of the Li ion into a nearby equivalent position provides an equally stabilising Coulomb potential well for another equivalent Si atom. This will lead to electron tunnelling from the original Si site to a new site. This may offer a possible alternative explanation to the temperature dependence of the ESR signal. The calculated barrier for Li^+ ion diffusion in pure α-quartz is 0.4 eV.[128] Using NEB, the barrier for diffusion of Li^+ of the $[SiO_4/Li]^0$ centre between equivalent sites across a ring in α-quartz was calculated as 0.56 eV. This Li^+ ion displacement is accompanied by an electron transfer to another Si site and is equivalent to diffusion of the whole centre. At low temperatures the Li ions cannot overcome this diffusion barrier, hence the strong, discrete ESR signal. However, at increased temperatures Li ions start moving around and the ESR signal should decrease until it vanishes completely due to rapid electron transfer

between Si sites.

To summarize, these results demonstrate that the character of electron trapping for the Ge and Li impurities in α-quartz are qualitatively similar. The structure of both electron traps involves an opening of an O–Si(Ge)–O angle. In chapter 6, we discuss whether electrons can be trapped at intrinsic sites in SiO_2 in a similar manner as we have seen in this chapter.

6

Intrinsic Electron Trapping Sites in Silicon Dioxide

6.1 Introduction

As mentioned in the introduction of chapter 5, electron trapping is known to have a dramatic effect on the performance and reliability of electronic devices employing SiO_2 as a gate insulator and charge trap flash memory devices.[84,129] In that chapter, we focussed on electron trapping at impurities in SiO_2 and saw that electrons could be trapped in Ge- and Li- doped SiO_2 in deep states in the band gap. We now turn to whether electrons can be trapped at intrinsic sites, i.e. unaided by impurities or coordination defects.

Little is known regarding the possibility of *intrinsic* electron trapping in the a-SiO_2 network. Bersuker *et al.* used molecular models to suggest that electrons can be trapped by Si–O bonds in a-SiO_2, leading to their weakening and thus facilitating bond dissociation.[130] Using a F_3Si–O–SiF_3 cluster, chosen to simulate the structure of two SiO_4 tetrahedra facing each other, they showed that an extra electron introduced into this cluster may localize on a Si–O bond, causing the other Si–O bond associated with the oxygen to contract and strengthen. The extra electron localizes in an oxygen 'p' state, significantly weakening one Si–O bond. The O–Si–O angle after the electron has been localized on the Si–O bond is 144°.

Further calculations by Camellone *et al.* have shown that electrons can be trapped in non-defective continuum random network models of a-SiO_2.[131] In their study, several structures of 72 atoms of a-SiO_2 were generated using classical MD simulations. The electronic structures of these models were then calculated using DFT, utilizing the generalized gradient approximation (GGA) for the exchange-correlation functional and including a self-interaction correction. The potential energy surface of the system with an extra electron was explored along a reaction coordinate defined as the elongation of one Si–O bond. The global energy minimum corresponds to the neutral equilibrium geometry where the electron is delocalized over the system, but a metastable state was found where the Si–O bond extended to 1.83 Å. In this state, an electron is localized on the Si atom. Extension of the Si–O bond and electron localization also resulted in expansion of the O–Si–O angle up to 156.44°. The barrier from the delocalized state to the metastable localized state was found to be 0.23 eV, with the localized state higher in energy by 0.17 eV. Recent calculations have also demonstrated that silicon dangling bonds at SiO_2 surfaces are deep electron traps and can form corresponding negatively charged defects.[132] However, these theoretical predictions have not yet been confirmed experimentally due to challenges in identifying and characterizing electron trapping centres in SiO_2.

Unlike in optical fibres and other optical devices, where electrons and holes are created by electronic excitation, in MOS devices they are often injected from the Si

substrate. For example, electron trapping at an energy of 2.8 eV below the conduction band of a-SiO_2 has been observed using photon-stimulated tunnelling experiments in device-grade oxides grown on Si and SiC crystals in a series of papers.[133–136] Furthermore, low-temperature capacitance[137] and Hall effect measurements[138,139] on 4H-SiC MOS devices revealed that the density of these electron trapping states can be as high as 10^{14} cm^{-2} eV^{-1}. The trap density of 10^{13} cm^{-2} measured inside a 2-nm thick near-interface SiO_2 layer[133,136] corresponds to $\approx 5 \times 10^{19}$ cm^{-3} in terms of volume concentration. This is much higher than observed densities of the established intrinsic defects in thermally grown a-SiO_2. The absence of a comparable density of electron traps in bulk a-SiO_2 suggests that electron trapping at 2.8 eV deep centres takes place not on pre-existing defects but rather at intrinsic sites in the oxide network itself. Whether the substrate plays any role in stabilizing these traps remains unclear. These results, as well as the insight gained from the electron trapping at impurities described in chapter 5, motivate further investigation of the possibility of electron trapping in amorphous silica network.

In this chapter, electrons are shown to trap in continuous non-defective a-SiO_2 networks, forming deep electron states in the gap. The geometric structure of these centres is highly similar to that of electrons trapped by Ge, where the key to the electron trapping is the wide opening of the O–Ge–O angle, or Li centres in quartz, where it is facilitated by the opening of the O–Si–O angle. It turns out that precursor Si sites with wide enough O–Si–O angles, which occur naturally in a-SiO_2 structures, can facilitate spontaneous electron trapping at Si sites. Using this *fingerprint* we estimate the concentration of intrinsic electron trapping sites in a-SiO_2.

6.2 Calculation Details

6.2.1 Classical Calculations

The calculations presented in this work make use of both classical force-fields and *ab initio* theory. The ReaxFF[51] force-field was used to generate 20 models of amorphous

SiO_2, each containing 216 atoms, modelled within periodic boundary conditions and as described in chapter 2. ReaxFF was parametrized to reproduce the properties of various silica polymorphs, small silica clusters and silicon polymorphs.[52] This force-field allows one to calculate Si and O atoms in varying oxidation states based on the instantaneous geometry of the system. This is accomplished by assigning a charge dependent atomic energy and exploiting the electronegativity equalization principle.[42]

The extended bulk silica structures used in this study - containing up to 401,760 atoms - were generated using the potential created by van Beest, Kramer, and van Santen (BKS).[38] It takes the functional form:

$$V(\mathbf{r}) = \frac{q_i q_j}{\mathbf{r}} + A_{ij} e^{(-b_{ij}\mathbf{r})} - C_{ij} r_{ij}^{-6} \tag{6.1}$$

The parameters for Si and O are taken from Ref.[38] and are included in table A.1 in the appendix. This Buckingham-type potential allows one to perform calculations much faster than the ReaxFF potential and is more suited to creating large a-SiO_2 structures. As can be seen in the results, comparing results obtained with two very different force-fields gives more confidence in our predictions. All classical atomistic simulations were performed using the LAMMPS code.[61] To generate amorphous structures, classical molecular dynamics simulations were run using ReaxFF and BKS to melt and quench crystalline SiO_2 structures into an amorphous state, as described in chapter 3. However, for the BKS simulations, the temperature was raised to 7000 K instead of the 5000 K melting temperature used for ReaxFF. The differences in melting temperature stem from the differences in parametrization and use of different functional forms in the potentials. The BKS structures have a higher density of 2.37 g cm^{-3}. The Si–O bond lengths of the BKS structures average at 1.61 Å, while the O–Si–O angles average at 108° and the Si–O–Si angles average at 142 °.

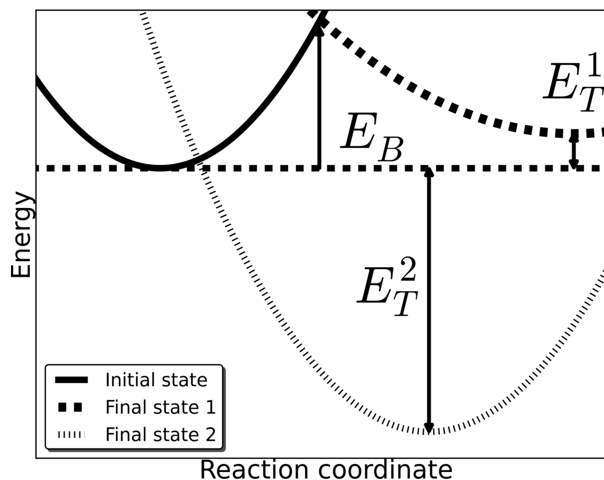

Figure 6.1: A schematic of one-dimensional diabatic potential energy surfaces corresponding to an initial electronic state and two final electronic states of the system with extra electron. The energy labelled E_B is the thermal barrier to electron trapping. The energies labelled E_T are the trapping energies, calculated as the total energy difference between the initial and final state. There are two trapping energies shown in the figure. The physical meaning of the negative E_T^1 is that the final state is thermodynamically unstable with respect to the initial state. The final state 2 is thermodynamically stable with respect to the initial state.

6.2.2 Density Functional Theory Calculations

Density functional theory (DFT), implemented in the CP2K code, was used to further optimize geometries of the ReaxFF structures and calculate their electronic structures,[27] as described in the calculation details section of chapter 5.

To discuss the electron trapping by impurities in perfect crystalline or amorphous SiO_2 structures, the total energies of the initial and final states with the extra electron in the system were compared, as illustrated in Fig. 6.1. The left diabatic curve (labelled as 'initial state' in Fig. 6.1) represents the system with an extra electron in the initial state while the right curves (labelled as 'final state 1 or 2') represent the final state with the electron localized on, for example, a Ge impurity or on a Si ion in the pure matrix after full geometry relaxation. E_B is the thermal barrier for electron trapping from the initial state to the localized state and E_T is the trapping energy, calculated as the total energy difference between the initial and final electronic states. In this chapter, two different scenarios are discussed. Trapping from the initial state to the 'final state 1' in Fig. 6.1 requires a thermal barrier to be overcome.

The final state is higher in energy, corresponding to a negative trapping energy, and is thermodynamically less favourable than the initial electronic state. The second scenario corresponds to electron trapping from the initial state to the 'final state 2' in Fig. 6.1. This electron trapping is barrier-less or has a small barrier, the final state is thermodynamically more favourable and corresponds to a positive E_T. The physical meaning of the initial and final states is discussed below for each particular system.

6.3 Results of Calculations

6.3.1 Electron Trapping in Bulk α-Quartz

An extra electron was added into the perfect α-quartz lattice and the geometry was optimized using DFT, resulting in the electron becoming fully delocalized at the bottom of the conduction band with no change in the structure of the lattice. This is in good agreement with previous theoretical calculations. Using the insights gained from electron trapping at impurities in SiO_2, perturbations to the α-quartz structure were investigated to see if they could lead to localization of an electron. The key to electron trapping in Ge- and Li-doped α-quartz seemed to be the wide O–(Ge)Si–O angle. Therefore, the O–Si–O angle was perturbed in order to see whether this would allow an electron to localize at that site.

The SiO_4 tetrahedra in α-quartz are made up of two shorter Si–O bonds and two longer Si–O bonds and a discrete O–Si–O angle which measures $\approx 109.5°$. These calculations started from the neutral optimized structure of α-quartz. A random Si atom was chosen and the two O atoms associated with the two longer Si–O bonds were displaced so that an O–Si–O angle became greater than 135°. The O–Si–O angle associated with the two longer Si–O bonds was chosen by analogy with the lowest energy electron trap in Ge-doped α-quartz. An extra electron was then added to the now perturbed system and the geometry was optimized. This lead to the extra electron localizing on the Si atom at the centre of the Si site around which the O atoms had been displaced. The geometry optimization further opens the O–Si–O angle to

161° and the two Si–O bonds elongate from 1.61 to 1.74 Å, while the other two bonds of the tetrahedron both elongate to 1.69 Å. This structural relaxation is similar to the one observed for both the Ge and Li electron centres in chapter 5. The spin density of the system is now highly localized on the Si site, as can be seen in Fig. 6.2a. The relaxation is highly localized around the defect, and as can be seen in Fig. 6.2a the surrounding α-quartz lattice remains highly crystalline. Mulliken population analysis reveals that the charge of the Si ion, on which the electron is localized, is $+1.04\ |e|$, significantly lower than the $+1.43\ |e|$ average charge of Si in α-quartz, and that the Mulliken spin moment is 0.86, indicating that the spin is highly localized on it. The electron trap creates a one-electron state 2.5 eV below the bottom of the α-quartz conduction band which is principally Si and O ‘sp’ in character. The position of this level can be seen in the density of states plotted in Fig. 6.2b.

The barrier to self-trapping an electron into this state from a delocalized conduction band state was calculated using CI-NEB as 0.57 eV, while the (self)-trapping energy of this system was found to be -0.32 eV. This indicates that the self-trapped electron polaron state in pure α-quartz is thermodynamically unstable with respect to the delocalized state (see Fig. 6.1). De-trapping from the localized state into the delocalized state requires overcoming a barrier of 0.25 eV. The O–Si–O angle at the maximum of this barrier is 134°.

To summarize, these results show that an electron can be trapped in deep states at Si sites in α-quartz. The trapping is driven by a wide O–Si–O angle. In bulk α-quartz, all bonds have an equilibrium value of 1.61 Å, therefore to create an electron trapping site, an O–Si–O angle has to be opened. This requires overcoming an energetic barrier of 0.25 eV.

6.3.2 Electron trapping in amorphous SiO_2

Electron trapping in a-SiO_2 was studied using twenty periodic models of bulk a-SiO_2. Each model contained 216 atoms. The geometries of the ReaxFF generated amorphous structures were optimized in the neutral charge state within DFT and then

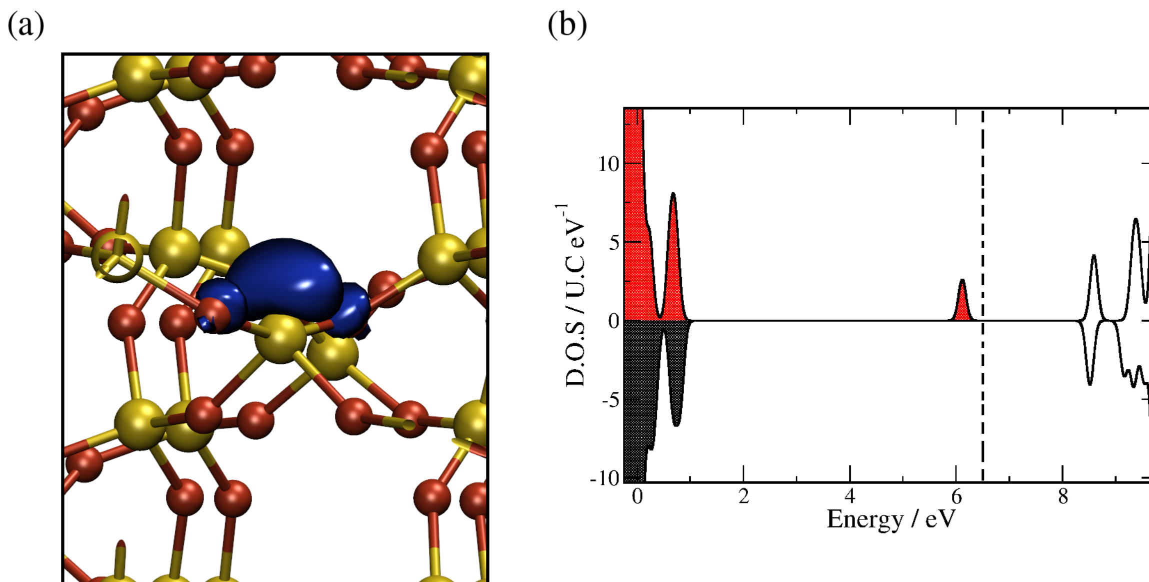

Figure 6.2: The square modulus of the wave function of an extra electron occupying the lowest state at the bottom of the conduction band of a-SiO_2. The bigger spheres connected to four atoms are Si atoms and the smaller spheres connected to two atoms are O atoms. The darker blobs represent the magnitude of the modulus of the wave function. The isovalue used to represent the square modulus of the wave function is 0.005.

an extra electron was added to each model. In chapter 3, the geometrical distributions of a-SiO_2 were discussed with Fig. 3.10 showing the distributions of Si–O bond lengths, O–Si–O and Si–O–Si angles obtained after DFT geometry optimization of the neutral cells. The geometrical properties of the optimized structures change slightly with respect to those obtained with ReaxFF, whose distributions can be seen in Fig. 3.7. The Si–O bond lengths of these 20 models after DFT optimization average at 1.62 Å, ranging from 1.58 Å to 1.67 Å. The Si–O–Si angles average at 147°, ranging from 112° to 179°, while the O–Si–O angles average at 109°, ranging from 95° to 137°. Analysis of the ring size distribution after DFT optimization shows the 4- and 5-member rings to be dominant with smaller contributions from 3- and 6- member rings. The electronic structure calculations predict an average one electron band gap of 8.1 eV, ranging from 7.7 to 8.3 eV over all 20 models. For comparison, the one-electron band gap of α-quartz is 8.6 eV.

These calculations start from 20 models of a-SiO_2 optimized in the neutral charge state. In each model, an extra electron was added so that each system is negatively

charged. Along with the extra electron, an extra uniform positive charge was added to each system. The extra electron initially occupies the lowest unoccupied state. In all structures, this state is partially localized on several Si and O ions, as illustrated in Fig. 6.3a for one of the structures. In comparison, a state which sits deep in the conduction band is shown in Fig. 6.3b. This band-like state is delocalized over all atoms in the system, in contrast to the partially localized lowest unoccupied state. The energetic position of the lowest band-like state is highlighted as the mobility edge on the density of states plotted in Fig. 6.3c. Each system's geometry was then optimized with the extra electron, resulting in spontaneous electron localization in four out of the twenty models. This localization was accompanied by a strong local distortion around a single SiO_4 tetrahedron, similar to the trapped electron centre relaxation in α-quartz. In each of the four structures, the extra electron is localized on one Si ion, with the two O neighbours repelled so that an O–Si–O angle is opened to $\approx$ 172°, as shown in Fig. 6.4a. The Si–O bonds making up this O–Si–O angle extend from 1.63 and 1.64 Å to 1.78 and 1.82 Å, respectively (see Fig. 6.4). Mulliken population analysis shows that as a result of the electron localization, the Si ion charge decreases by about 0.25 $|e|$ compared to its charge in the neutral system. The average gain in energy resulting from the barrier-less electron localization (E_T in Fig. 6.1) in the four models is 1.25 eV, ranging from 0.72 to 1.71 eV. The electron state occupied by the extra electron is located at $\approx 3.17 \pm 0.05$ eV below the bottom of the SiO_2 conduction band, indicating a deep electron trap. This was calculated as the difference in energy between the highest occupied and lowest unoccupied single-particle states. The single-particle state of the electron trap from the four models is plotted in Fig. 6.4.

The hyperfine splittings induced by the localized electron have been calculated and are shown in Table 6.1. The strongest hyperfine interaction is with the Si ion; however, there is a significant interaction with the nearby oxygen atoms. Interestingly, some of the hyperfine interaction values are similar to the experimental values of a defect known as the E′ centre in amorphous silica.[101] This is not surprising considering the

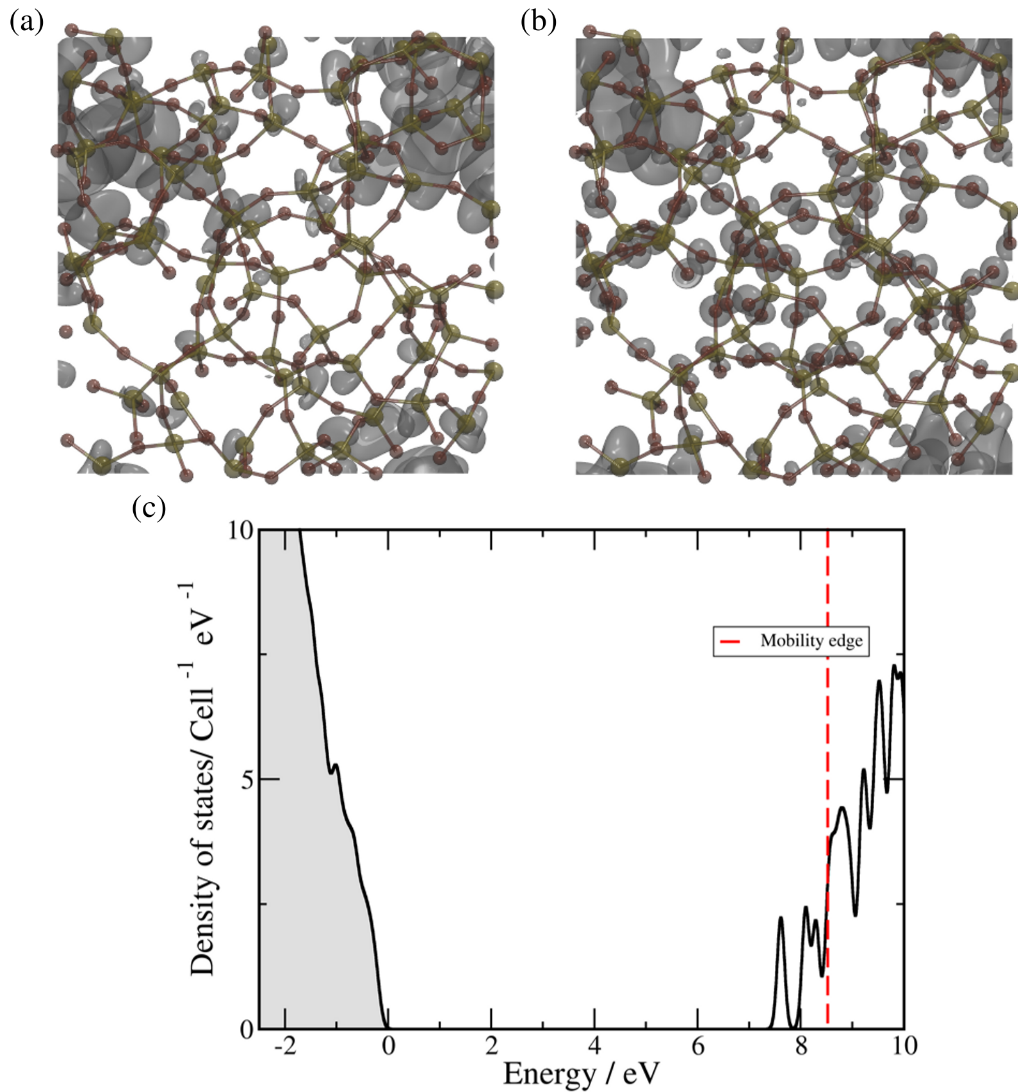

Figure 6.3: The square modulus of the wave function of an extra electron occupying the lowest state at the bottom of the conduction band of a-SiO_2. The bigger spheres connected to four atoms are Si atoms and the smaller spheres connected to two atoms are O atoms. The darker blobs represent the magnitude of the modulus of the wave function. The isovalue used to represent the square modulus of the wave function is 0.0005.

strong electron localization on one Si ion. However, more models would be needed to give a more accurate distribution of the hyperfine values accessible to experiment.

In all four cases, the Si ion on which the electron traps initially forms the widest O–Si–O angle in the sample, exceeding 132°. In the sixteen remaining a-SiO_2 samples, where the distribution of O–Si–O angles was slightly narrower, the extra electron remained delocalized. To investigate whether this wide O–Si–O angle held the key to the electron localization, structural distortions were introduced to make two other random O–Si–O angles the widest in two separate systems. An angle in one of the systems was increased from 120.3° to 132.1°. Adding an extra electron into this system and optimizing the geometry results in the electron localizing on the Si ion within the perturbed angle and causes it to open further to 160.68°. An angle in a separate system was changed from 121.3° to 132.0°. When the electron was added to this system, the O–Si–O angle opened to 164.5°. These results demonstrate that, although a wide O–Si–O bond angle serves as an efficient precursor to spontaneous electron trapping in a-SiO_2, thermally activated trapping can also take place at other sites by opening an O–Si–O angle. These results also make apparent the link between the geometric structure of a trap and its electronic properties and allows one to use the criterion of wide O–Si–O angles as a *fingerprint* for identifying precursor sites for spontaneous electron localization in initial a-SiO_2 structures and estimating the concentration of such sites.

6.3.3 Concentration of electron trapping sites in a-SiO_2

As suggested above, by analysing the structure of an a-SiO_2 sample for the presence of O–Si–O angles exceeding 132° one can estimate the lower limit of the concentration of precursor sites which can act as electron trapping centres. The results from the twenty models of a-SiO_2 samples indicate that the presence of an O–Si–O angle exceeding 132° always leads to spontaneous localization of extra electrons in a-SiO_2. This angle is at the tail of the O–Si–O angle distribution in regular SiO_2 structures constructed using the ReaxFF potential and optimized using DFT.

Atom	Bond length/Å	Values / mT
Si		-50.98
		-45.45
		-45.23
O	1.82	-4.181
		-2.660
		-2.624
O	1.78	-5.714
		-4.357
		-4.298
O	1.70	-1.548
		-1.216
		-1.212
O	1.70	-1.581
		-1.264
		-1.259

Table 6.1: Geometrical parameters and the average principal values of the hyperfine tensor of the electron trap in a-SiO_2 from the four models. The bond lengths shown are with respect to the Si atom on which the electron is trapped.

To test whether the existence of these precursor sites and their concentration depends on the model of amorphous structure and to obtain better statistics, three additional samples of amorphous SiO_2 were created using the BKS interatomic potentials[38] as described in section 5.2. These potentials are often used in studying the structural properties of a-SiO_2 and give good agreement with experimental data.[59,68,69] The three samples created have dimensions of $50 \times 25 \times 5$ nm^3, $25 \times 12.5 \times 2.5$ nm^3, and $12.5 \times 7 \times 1.5$ nm^3 and include 401,760; 55,296 and 8,640 atoms, respectively. These models were searched for O–Si–O angles exceeding the fingerprint value of 132° to estimate the concentration of electron trapping precursor sites. The concentration of such sites in all models proved to be very similar with a volume concentration of 4×10^{19}cm^{-3} in the sample containing 401,760 atoms. It is interesting to note that in spite of the difference in cell sizes and force-fields used, this concentration agrees well with the original observation of four trapping sites in twenty 216 atom samples.

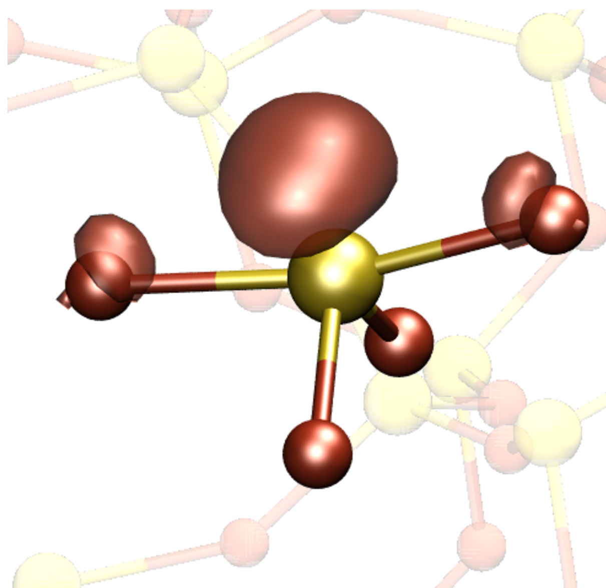

Figure 6.4: Atomic structure and spin density distribution of an intrinsic electron trap in a-SiO_2. We highlight the SiO_4 tetrahedron on which the electron traps and show the spin density only on the nearest ions. The spin density isovalue is 0.02.

6.4 Discussion and Conclusions

These calculations demonstrate that electrons can indeed trap at intrinsic sites in both crystalline and amorphous SiO_2. The distribution of geometrical parameters in the disordered a-SiO_2 leads to the existence of precursor Si sites which can spontaneously trap an electron in a state $\approx$ 3.2 eV below the bottom of the conduction band. The estimated concentration of these precursor sites is 4×10^{19} cm^{-3}. The large average distance between precursor sites suggests that diffusion of trapped electrons via a thermally activated tunnelling mechanism should be quite inefficient and they are more likely to move via thermal activation into the mobility edge states of amorphous silica at high temperature.

These results differ from those previously reported by Bersuker[130] and Camellone[131] which focussed on the effect of the Si–O bond length and its relation to intrinsic electron trapping in SiO_2. The calculations presented above indicate that the O–Si–O angle is a more efficient precursor for electron trapping in SiO_2. The differences in these results from those presented by Camellone *et al.* could stem from our use of a non-local functional as opposed to the generalized gradient approximation (GGA),[131] as GGA tends to underestimate the degree of electron or hole localization.[140,141]

The high volume concentration of large O–Si–O angle electron trapping precursor sites suggests that the electron trapping can be abundant in a-SiO_2 samples. However, identifying these electron traps in relatively pure bulk samples may require irradiating at liquid nitrogen temperatures, where both trapped electrons and holes are immobile.[142] These results suggest that trapped electrons can be stable even at room temperature. However, trapped holes become mobile below 200 K and can recombine with electrons. These results also support the common perception that the abundance of impurities, such as Al, Ge, Li, Na and water in quartz as well as in silica glass samples may lead to efficient electron trapping by impurity centres and further hamper the identification of intrinsic electron traps in a silica network.

These intrinsic trapping states are correlated to electron traps identified experimentally in MOS devices[143] at an energy of 2.8 eV below the conduction band of a-SiO_2 grown on Si and SiC crystals.[133–136] Experimentally, these traps were populated by illuminating the MOS structures by photons of energy sufficient to excite electrons from the semiconductor valence or conduction band above the edge of the SiO_2 conduction band. They had initially been correlated with oxygen deficient centres at the near-interfacial oxide.[134,135,144] However, later experiments on nitridated SiC/SiO_2 samples questioned this attribution, particularly when taking into account the fact that the density of known O-deficiency centres (E'_γ and E'_δ centres) rarely approaches the density range of 10^{13}cm^{-2} found for the 2.8 eV deep electron traps. Although these electron traps are especially pronounced in 4H-SiC/SiO_2 devices, they seem to play a role in all devices containing SiO_2 as the insulating material, suggesting that they may be intrinsic to the oxide. For instance, these traps are expected to appear below the conduction band of Si nano-crystals in the case of quantum confinement.[145,146]

The intrinsic electron traps in a-SiO_2 discussed in this chapter could be good candidates for understanding these data. The calculated concentration of precursor sites for intrinsic electron traps approaches the experimentally observed value for the states filled by photo-stimulated tunnelling from SiO_2 valence band. However,

populating such a density of electron traps via electron injection from an electrode through the SiO_2 conduction band should be much less efficient because an electron capture event requires dissipating about 1.5 eV of relaxation energy into phonons during the trapping process. This is likely to be slower than fast electron transport in the conduction band of a thin oxide towards an opposite electrode. In order to keep the additional (unpaired) electrons on these centres, one must ensure sufficiently high strength of electric field is externally applied to the interface. The latter can hardly be realized under the conditions of an ESR experiment because the presence of conducting electrodes impairs the quality factor of the microwave resonator. Furthermore, all available experimental evidence concerns interfaces of SiO_2 with semiconducting materials (Si, SiC), which might suggest that the experimentally observed high probability of electron trap occupation may be related to the strain in the SiO_2 network near the interface, while in the bulk of the film their concentration may be lower. The observed trap photo-ionization energy at 2.8 eV is between the values calculated for α-quartz (2.5 eV) and a-SiO_2 (3.0 eV). The results in this chapter indicate that the geometry of the oxide structure can significantly affect the position of the defect level, and the discrepancy between the experimental value and our a-SiO_2 value may reflect the higher oxide density in thermally grown oxides[2,147] rather than the density obtained in this work.

To summarize, these results demonstrate that, similar to holes,[142] electrons can be trapped at structural precursor sites in an amorphous silica matrix, forming deep electron states in the oxide band gap. The geometric structure of trapped electron centres in a-SiO_2 are qualitatively similar to the extrinsic electron trapping centres studied in chapter 5. In a-SiO_2, these states may be responsible for the electron trapping observed at interfaces of SiO_2-based MOS devices and should be present in bulk SiO_2 samples.

7

Optical Absorption Spectra of Trapped Electrons in SiO_2

7.1 Introduction

The previous two chapters presented calculations which characterized intrinsic and extrinsic electron traps in a-SiO_2. However, unambiguously identifying all sites responsible for electron trapping in a-SiO_2 has proved particularly challenging because of a large number of possible charge redistribution channels and the presence of water and impurities in most samples. Thus, spectroscopic evidence of intrinsic electron trapping in a-SiO_2 is still missing. In this chapter we calculate the optical absorption spectra of the intrinsic electron traps in a-SiO_2 using the embedded cluster method

and TDDFT described in chapter 2 and compare it to low temperature experimental optical absorption spectra measured by Prof. Katsumi Tanimura.

In order to assess the accuracy of the method, we first calculate the optical absorption spectrum of the GEC in α-quartz, described in chapter 5, as an absorption band at 4.2 eV has been universally attributed to it. We then calculate the spectra for the intrinsic electron traps in a-SiO_2, and by analysing this data and comparing it to experimental optical absorption spectra, an absorption band was identified that can indeed serve as a signature of intrinsic electron traps.

7.1.1 Experimental Observations

In order to identify absorption bands associated with electron trapping centres in SiO_2, optical absorption spectra of electron irradiated SiO_2 were measured at 80 K by Prof. Katsumi Tanimura of Osaka University. A detailed account of the experimental observations is given below.

Three different, high-purity a-SiO_2 samples were used in order to differentiate the results that are specific to only a given sample from those that are common to all samples. These include Suprasil W1 (SW1), Viosil-SCF (SCF), and Viosil-SZ (SZ); all fabricated by Shin-Etsu Quartz, LTD. SW1 has less than a few ppm of OH ions but includes a considerable amount of dissolved O_2. SZ contains almost no chemical impurities - concentrations of both Cl and OH ions are less than 1 ppm - however, it includes 500 ppm of oxygen deficiency (so called ODC(I)) centres that exhibit a strong absorption peak at 7.6 eV. On the other hand, SCF has no Cl ions (less than 1 ppm), but includes about 1000 ppm of OH ions. All samples were cut and polished to a size of $8 \times 10 \times 1$ mm and irradiated with electron pulses (1 MeV, 20 ns duration) generated from a Febetron (HP43710A) at 80 K. The optical absorption spectra were measured using a spectrophotometer (Shimazu UV-3100). A Xe-arc lamp with optical filters was used as the light source for optical excitation of the irradiated specimens. Red light with a wavelength range from 600 to 780 nm, and UV light with a peak at 320 nm (3.87 eV) and a band pass of 10 nm was generated by combining appropriate

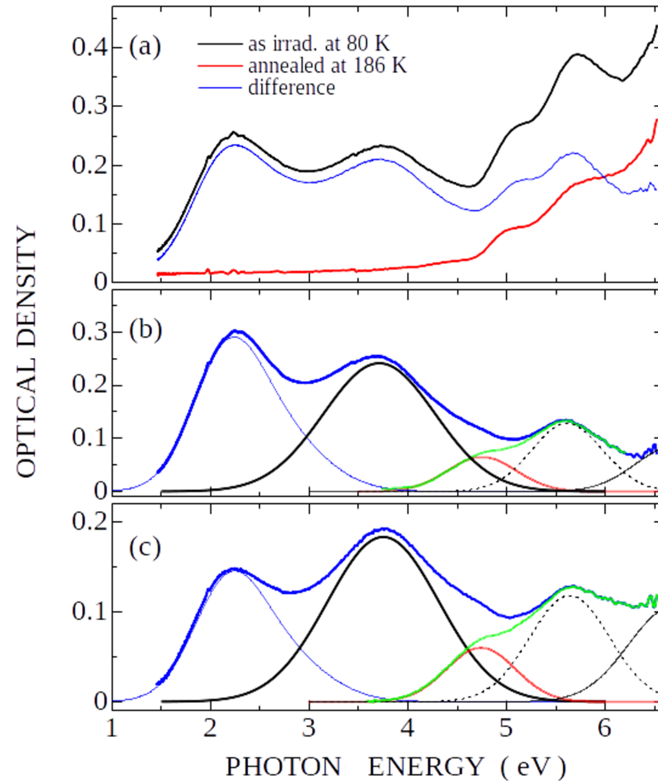

Figure 7.1: a) Optical absorption spectra of electron-irradiated a-SiO_2(SZ). The black curve was recorded at 80 K after electron irradiation. The red curve was recorded at 80 K after an anneal at 186 K. The blue curve is the difference between the black and red curves, revealing the absorption components due to centres annihilated during the anneal. b) and c) show the difference spectra between the absorption bands of electron-irradiated a-SiO_2 and those after selective excitation: b) by red light (600 - 780 nm) and c) by UV light (320 $\pm$ 10 nm). The difference spectra are de-convoluted into the absorption bands due to STH2 (thin blue solid curve at 2.2 eV), a 3.7 eV band (thick solid curve), a 4.7 eV band (thin red curve), the E′ band (broken curve centred at 5.8 eV) and the rest of the spectrum (solid green curve).

filters.

The black curve in Fig. 7.1a shows the optical absorption spectrum induced by electron-pulse irradiation at 80 K. Several peaks are clearly distinguishable. The lowest-energy peak at 2.2 eV is the absorption band due to self-trapped holes with two-centre type configurations (STH2).[148] The peaks at 5.1 eV and 5.7 eV are associated with B2 and E′ centres, respectively. The strong absorption peaking at >6.5 eV is usually attributed to ODC(II) or B_2 centres.[149] We note that similar peaks with almost the same heights have been generated in SW1 and SCF samples, which contain almost no oxygen vacancies (see Fig. 2 in ref. [148]). The peak at 3.7 eV is an, as yet, unidentified band which is commonly generated in a-SiO_2 samples irradiated and

measured at low temperatures and thus not related to specific pre-existing lattice imperfections in a-SiO_2.

To reveal the origin of the 3.7 eV band, its growth kinetics was measured as a function of the electron dose. In Fig. 7.2, the growth characteristics of the E′ centres (5.7 eV), STH2 (2.2 eV), and the 3.7 eV absorption band are shown. The yield of E′ centres increases linearly with the dose, while those of the STH2 and the unidentified centre are strongly correlated and show a tendency to saturate at doses greater than $\approx 1.5 \times 10^5$ Gy.

The thermal stability of the defects responsible for the optical absorption spectrum in Fig. 7.1a was studied by a pulse annealing method. The red line in Fig. 7.1a shows the absorption spectrum after warming the irradiated sample up to 186 K for 5 mins, followed by absorption measurement at 80 K. The peaks at 2.2 eV and 3.7 eV are completely annealed out, which is also demonstrated by the blue curve showing the difference between the initial low temperature and the post-anneal spectra. It is also evident that absorption bands with energies above 4.5 eV are also partially annihilated after annealing at 186 K.

The results obtained during the growth and anneal processes indicate that the 3.7 eV band is either an absorption band of STH2 or is due to a centre formed as a partner of a self-trapped hole. The former possibility can be ruled out based on the

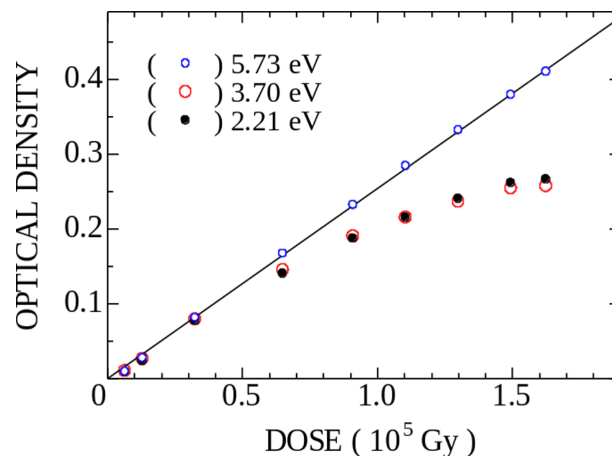

Figure 7.2: Growth kinetics of the optical absorption bands of electron irradiated a-SiO_2 measured at 80 K. The 2.21 eV and 3.70 eV peaks show a trend to saturate at a dose greater than 1.5×10^5 Gy.

symmetry of the centre revealed by the polarized bleaching experiments.[148] The 2.2 eV band shows a clear dichroism by which the asymmetric spectral shape of the STH2 band could be determined. However, the 3.7 eV band does not show any dichroism, indicating that the centre is not a two-centre type.

Alternatively, the 3.7 eV band could originate from an electron component of electron-hole pairs created by the irradiation. Part of the holes self-trap, hence the STH2 signal observed in our optical absorption spectra (see Fig. 7.1). Another part could be trapped by oxygen vacancies forming E′ centres, which absorb at 5.7 eV, or by other pre-existing defects. Electrons can also trap on pre-existing oxygen vacancies,[150] impurities, or on intrinsic network sites.[151] The calculated optical absorption of negatively charged oxygen vacancies peaks at about 3.3 eV[150] and they can contribute to the 3.7 eV absorption in SZ samples which include considerable amount of oxygen vacancies. However, as noted above, the 3.7 eV band is induced also in SW1 and SCF samples, which do not include pre-existing oxygen vacancies.

Optical bleaching experiments at 80 K can shed more light on the origins of absorption spectra by releasing trapped holes and electrons into valence and conduction bands, respectively, as a result of selective excitation. Fig. 7.1b exhibits a difference spectrum of the sample before and after bleaching by red light (600-780 nm), which selectively excites only STH2. This excitation results in bleaching of the 3.7 eV band, as well as other higher energy bands. Interestingly, the B_2 band is little affected by the excitation, although a substantial amount of the E′ band is bleached. Similarly, Fig. 7.1c shows the spectral components after selective excitation by UV light (320 $\pm$ 10 nm). The excitation in the 3.7 eV band results in bleaching of the 2.2 eV band and some of the higher energy bands including that of the E′ centre.

The ratio between the 2.2 eV and 3.7 eV bands is not the same in the two different photo-bleaching events, demonstrating that they are associated with different centres and support the assertion that the centre giving rise to the 3.7 eV absorption band is an electron partner associated with STH2. Figs. 7.1b and c also demonstrate that the decay of 3.7 eV band is always associated with the decay of the spectral components

around 4.7 eV and above 6 eV. This feature is not specific to the SZ sample, but is common to SCF and SW1 and hence characteristic to localized electron centres in a-SiO_2.

To summarize, optical absorption measurements made after electron irradiation at low temperature exhibit an unidentified peak at 3.7 eV in addition to the peaks at 2.2, 4.7 and 5.7 eV associated with defects. The 3.7 eV peak is correlated with STHs in a-SiO_2 but is distinct from that centre. The remainder of the chapter is devoted to calculating the optical absorption spectra of intrinsic electron traps in a-SiO_2 and comparing them to this experimental data.

7.2 Calculation Details

To investigate the origins of the absorption bands of the intrinsic electron trap in a-SiO_2, their optical transitions were calculated using an embedded cluster method described in chapter 2.5 implemented in the GUESS code.[88] The inhomogeneous broadening of the absorption spectra due to the structural disorder of the glass samples was included by using seven independent models of a-SiO_2 which were generated as described in chapter 3. To assess the reliability of the method, the optical absorption spectrum of the GEC in α-quartz was calculated initially and compared to its well known experimental spectrum. To model the GEC, only one model of the α-quartz lattice was used.

Each model was adapted for use in an embedded cluster model as follows. A spherical nanocluster was generated from the unit cells obtained in chapter 3. Each nanocluster was divided into two regions - I and II. Region I is located in the centre of the nanocluster and is further subdivided into three concentric regions of different physical descriptions. The centre of Region I consists of a cluster of atoms which are treated using DFT implemented in the Gaussian09 code. We used a hybrid BxLYP functional with x=32.5% exchange, which provides a better description of the band gap than the B3LYP functional[35] and improves the functional's linearity.[152] The Si

and Ge atoms are described with a 6-31G* basis set while the O atoms with a 6-31G basis set. The outer section of Region I is described by a core-shell variant of the classical BKS potential.[87] In the core-shell model, an atom is divided into two point charges connected by a spring, allowing the atoms to change their polarization. The central quantum region is interfaced with the outer classical ions by the embedding pseudopotentials, described in detail in ref.[87] The outer Region II is composed of non-polarizable ions which are fixed in perfect lattice sites and interact with the ions in Region I by the classical BKS potential without shells.[38] All atoms in Region I are allowed to relax during geometry optimizations to provide the atomic structure of the electron traps. The optical absorption spectra of the electron traps were then calculated using the time-dependent DFT (TDDFT) method,[24] as implemented in the Gaussian09 code.

7.3 Results of Calculations

7.3.1 Optical Absorption of the Ge Electron Trapping Centre

The optical absorption spectrum of the well-known Ge electron centre (GEC) in α-quartz was calculated. The GEC was used to ensure that the embedding methods can accurately calculate the optical absorption spectra of localized electron centres in SiO_2, due to their similar structures and due to the fact that the GEC's absorption spectrum has been measured. The GEC in α-quartz is responsible for the Ge(I) ESR signal.[109] This signal strongly correlates with an optical absorption band at 4.2 eV, which is universally attributed to this centre.[125,148,153,154] Optical absorption spectra of Ge-doped SiO_2 include additional bands that peak at ≈ 5.8 eV and higher energies, which have also been tentatively assigned to the GEC in a-SiO_2.[155]

A quantum cluster containing 72 atoms and representing the α-quartz structure was embedded into the rest of the crystal as described in the calculation details. A single Si atom at the centre of the quantum cluster was substituted for a Ge atom and the geometry of the system was optimized in the neutral charge state. The relaxation

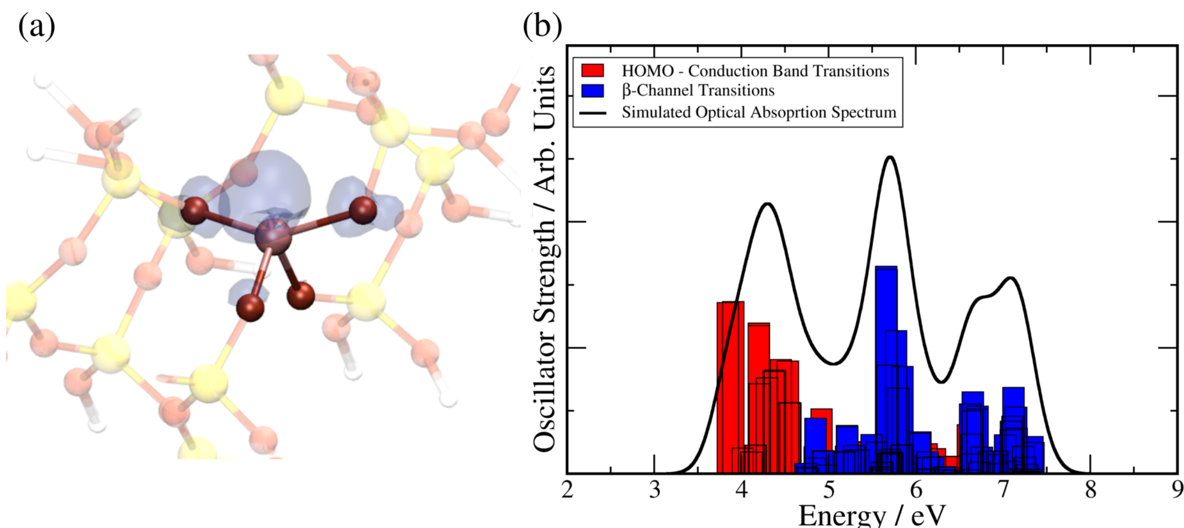

Figure 7.3: a) Atomic structure and spin density of the GEC in α-quartz. The GeO_4 tetrahedron is highlighted, where the pink ball is Ge, the Si atoms are yellow balls, the O atoms are red balls and the spin density is the blue polyhedron. b) Simulated optical absorption spectrum of the Ge electron trap in α quartz. The black line is a sum of all Gaussian broadened excitation energies weighted by their respective oscillation strengths. The bar plot shows the excitation energies and their respective oscillation strengths. Red bars correspond to electronic transitions in the α channel while blue bars correspond to β channel.

resulted in an extension of the Ge–O bonds to 1.72 Å compared to the Si–O bonds (1.64 Å) in α-quartz; however, the GeO_4 tetrahedron remains intact. The calculated band gap of the system is 7.2 eV with a Ge unoccupied state located just below the conduction band and strongly localized on the Ge atom. These results are consistent with the calculations on the GEC in a periodic model described in chapter 5.3.1.

An extra electron was then added to the system followed by a full geometry optimization of Region I. This resulted in a strong local relaxation, where the O–Ge–O angle opened from 109° up to 148° and the extra electron localized on the Ge atom, as shown in Fig. 7.3a. The Ge–O bond lengths extend asymmetrically, so that two bonds measure 1.83 Å while the other two bonds measure 1.87 Å. This defect introduces an occupied electron state which sits 5.0 eV below the α quartz conduction band.

The optical transition energies and oscillator strengths of the GEC in α-quartz were then calculated. The calculated optical absorption spectrum is plotted in Fig. 7.3b as a solid black line. The bar plot shows all one-electron transitions weighted by

their oscillator strengths. Each absorption is Gaussian broadened by 0.3 eV in order to simulate homogeneous broadening. The total spectrum shown by the black line is a sum of broadened excitation energies, weighted by their respective oscillator strengths. The optical transitions can be categorised into two types. The transitions of the first type are highlighted as red bars while those of the second type are highlighted as striped blue bars. The first type is caused by transitions of the unpaired electron localized on the wide O–Ge–O angle into quasi-local states at the bottom of the a-SiO_2 conduction band (see also transition 1 in the inset of Fig. 7.4b). The calculated spectrum exhibits a peak with a maximum at 4.2 eV which is a transition of this first type, in excellent agreement with the experimental signal. The second type is due to transitions of a β-spin electron from the occupied non-bonding oxygen 'p' orbitals, which have broken away from the top of the a-SiO_2 valence band due to the structural distortion introduced by the defect, to the unoccupied state which is localized on the wide O–Ge–O angle (see also transition 2 in the inset of Fig. 7.4b). In our calculated spectrum, they comprise 2 peaks with maxima at around 5.8 and 7.1 eV. The O 'p' states, which split from the top of the valence band, are localized around the wide O–Ge–O angle, similar to the O 'p' states of the nearest O neighbours highlighted in Fig. 7.3a. The 5.8 eV peak agrees very well with the band recently assigned to the GEC in a-SiO_2.[155]

7.3.2 Optical Absorption of the Electron Trapping Centre

Intrinsic electron trapping sites were selected based on a geometrical criterion of an O–Si–O angle greater than 132°. As has been shown in chapter 6, extra electrons can trap at such precursor sites without barrier. Each quantum region was constructed around such a wide O–Si–O angle, with the number of atoms ranging from 96 to 114. Due to the disordered nature of a-SiO_2 and the rather stringent criterion of O–Si–O angles being greater than 132°, it was not possible to standardize the numbers of atoms described quantum mechanically across the seven different glass samples. The quantum region was then interfaced with a classically polarizable region which

contained between 910 and 933 atoms. The diameter of the entire system was $\approx$ 50 nm while the quantum regions are $\approx$ 1.5 nm in diameter. The positions of all atoms in Region I were optimized in the neutral charge state. The band gap averaged over the seven different samples in the embedded cluster model is 7.7 eV, ranging from 7.4 to 8.1 eV.

An extra electron was added into each of the seven samples and their respective geometries were optimized, resulting in seven different intrinsic electron trap configurations, where an electron has localized on an Si atom and an O–Si–O angle has opened from 132° to 174°, ranging over 5°. These electron traps introduce an occupied single-particle state located on average 4.3 eV below the bottom of the conduction band in the a-SiO_2 matrix. The single-particle wave function of this state is shown in Fig. 7.4a.

The transition energies and oscillator strengths of all seven electron trapping configurations were calculated using TDDFT and plotted together with equal weights in Fig. 7.4b. The bar plot shows all one-electron transitions corresponding to the two types explained in the inset of Fig. 7.4b with their respective oscillator strengths. Each absorption line was then Gaussian broadened by 0.3 eV, the same as the GEC, to simulate homogeneous broadening. The black line in Fig. 7.4b was produced as a sum of all Gaussian broadened optical transitions in seven electron trapping centres weighted by their respective oscillation strengths. The strongest transitions of the first type are highlighted as red bars while the second type of transitions are highlighted as striped blue bars. The first type is caused by transitions of the electron localized on the wide O–Si–O angle (see Fig. 7.4a) into quasi-local states at the bottom of the a-SiO_2 conduction band composed of 'd' orbitals of nearby Si atoms and nearby O 's' orbitals. It exhibits a peak with a maximum at 3.7 eV. The second type of excitations is due to transitions of a β-spin electron from the occupied non-bonding oxygen 'p' orbitals, which have broken away from the top of the a-SiO_2 valence band due to the structural distortion introduced by the intrinsic electron trap, to the unoccupied state in the band gap localized on the wide O–Si–O angle. They comprise a peak with a

maximum at around 6.4 eV. The O ‘p’ states, which split from the top of the valence band, are localized around the wide O–Si–O angle, similar to the O ‘p’ states of the nearest O neighbours highlighted in Fig. 7.4a. The whole spectrum is much broader than that for the GEC described in the previous section because transitions in each of the seven configurations have different energies due to disorder in a-SiO_2 and different local environments.

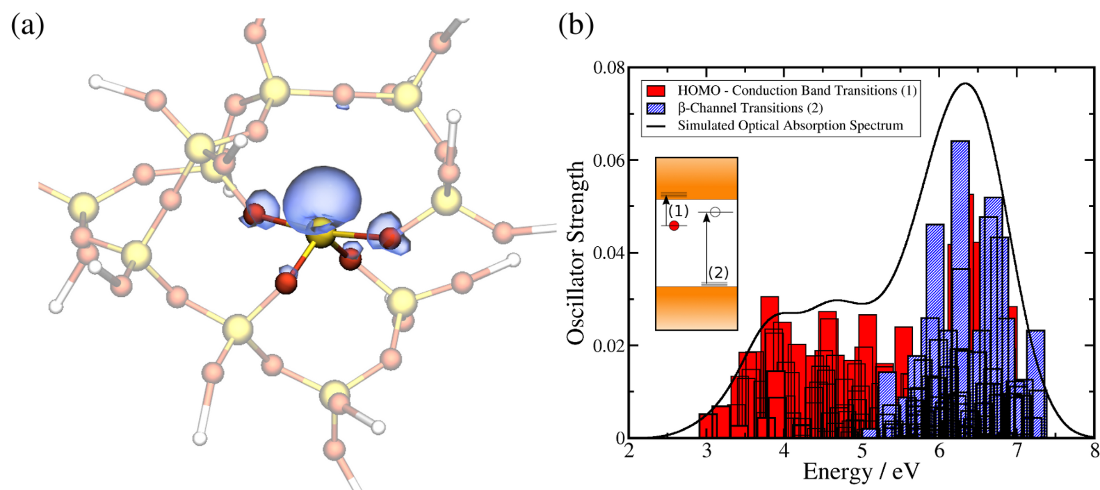

Figure 7.4: a) The one-electron wave-function of the electron localized in a-SiO_2. The tetrahedron with the wide O–Si–O angle is highlighted. b)The calculated optical absorption spectrum of intrinsic electron traps in a-SiO_2. The inset shows a schematic of the optical transitions that can occur in the intrinsic electron trap. Two types of transitions are shown by two colours. See text for discussion.

We note that the calculated spectrum has transitions in the energy range of 3-7 eV. This is consistent with both the anneal and spectral bleaching data, which show significant reduction of optical density at energies exceeding 4 eV (see Fig. 7.1). The nature of both types of transitions is the same as those of the GEC in α-quartz described in the previous section.

7.4 Discussion and Conclusions

Calculated optical absorption spectra of intrinsic electron traps in a-SiO_2 exhibit a band centred at 3.7 eV. This compares very well with experimental optical absorption spectra of electron-irradiated a-SiO_2 recorded at 80 K, where an unidentified peak has been measured at 3.7 eV and where self-trapped holes are immobile. These results

provide the strongest evidence yet for the formation of intrinsic localized electron centres in a-SiO_2 as a counterpart to self-trapped holes and a detailed model of a strongly localized electron in a disordered oxide. This localization is promoted by strained O–Si bonds and occurs on distorted SiO_4 tetrahedra. Therefore one can expect that similar electron traps can exist in other types of silica glasses,[156] as well as in feldspar and other silicates based on networks of SiO_4 tetrahedra. Many of these materials contain, as yet unexplained, deep electron centres responsible for therm-luminescence employed in e.g. luminescence dating.[157] Therefore, the optical signatures of intrinsic electron traps revealed here will be useful for understanding the properties of other silicates as well as the properties and stability of electronic and optical devices which utilize a-SiO_2.

8

Hydrogen's Interactions with Silicon Dioxide

8.1 Introduction

Hydrogen plays an important role in a number of technological applications which utilise a-SiO_2. In particular, hydrogen has long been used in both the microelectronics and fiber optics industries to passivate defects which exhibit electronically or optically detrimental properties (such as the P_b and E' centres[158]). Despite its use in passivating defects, it is also known for its various roles in the chemical and physical processes at Si/SiO_2 interfaces and in bulk amorphous SiO_2.[86,159–162] Hydrogen has been found to be involved in some hydrogen-complexed defects, such as the hydrogen

bridge,[11,163] the 74 G-, and the 10.4 G-doublet centre.[164] These defects are the subject of intense research efforts across a range of sciences; they may lead to severe electronic device degradation[165] and they play a role in radiation induced attenuation (RIA) in optical fibers.[154] The formation mechanisms of the hydrogen-complexed defects are largely unknown. In this chapter, we investigate hydrogen complexed defects which could be relevant to silica's technological applications and propose mechanisms for their formation and further interactions with hydrogen.

The E′ centre is a well known defect in SiO_2. It was first characterized using ESR techniques[101] and a theoretical model was proposed by Rudra and Fowler whereby a hole is trapped at an oxygen vacancy.[166] However, recent experiments using field-dependent recombination of holes trapped in SiO_2 with injected electrons[167] revealed that the paramagnetic state of the E′ centre is not always correlated with the entity bearing the positive charge. It has been suggested that the positive charge is protonic in origin, a hypothesis later corroborated by a number of experimental results.[167,168] Consequently the $O_3{\equiv}Si{-}H$ entity in a-SiO_2, which is easily identified due to its strong infra-red absorbance signal, has been suggested as a possible E′ precursor,[167] where upon hole trapping hydrogen dissociates from the Si–H bond in the form of a proton leaving behind a neutral paramagnetic E′ centre. The question remains as to whether the liberated proton is then trapped in SiO_2 or diffuses through and escapes the SiO_2 layer. A section of this chapter is devoted to understanding how a neutral E′ centre can be formed from Si–H bonds in a-SiO_2.

In addition, EPR analysis of OH-rich synthetic silica after irradiation suggests that atomic hydrogen, which can diffuse rapidly through a-SiO_2,[169] can interact with the a-SiO_2 network to create a charge neutral defect.[170,171] A 0.08 mT doublet due to proton hyperfine splitting has been assigned to a Si dangling bond coordinated by two bridging oxygens and an OH group. This centre is thought to result from the interaction of H^0 with electronically excited, strained Si–O bonds. However, reactions of atomic hydrogen with strained Si–O bonds have not been investigated theoretically and the perception that it interacts weakly with the a-SiO_2 network prevails in the

literature.[172–174] We investigate whether neutral, atomic hydrogen can interact more strongly with the a-SiO_2 network.

Previous theoretical studies have shown that hydrogen, both atomic and molecular, interacts with point defects in SiO_2. Using a cluster model and post Hartree-Fock (HF) methods , Edwards *et al.* studied the interaction of hydrogen molecules with E′-type defects (i.e. a $O_3{\equiv}Si^{\bullet}$ moiety) in α-quartz.[175] The clusters studied were terminated with O–H groups with the terminating H atoms fixed in space. They showed that the H_2 molecule dissociates at an E′ centre to leave behind a free H atom and an Si–H bond, passivating the 3-coordinated Si with a barrier of 0.78 eV. DFT calculations using hybrid functionals performed on small clusters by Lopez *et al.* also indicate the H_2 cracking reaction at E′ centres to be endothermic with a barrier of less than 0.5 eV.[176]

In summary, hydrogen atoms and molecules are known, both theoretically and experimentally, to interact with 3-coordinated Si defects in a-SiO_2 and can passivate the defect. In contrast, hydrogen has been shown to interact negligibly with the a-SiO_2 matrix.[86,172–174] However, recent experiments suggest that atomic hydrogen can in fact create new defects, although the formation mechanisms are entirely unknown.[171] In addition, experiments also show that the 3-coordinated Si defects may have a charge neutral analogue in addition to the well known positively charged vacancies known as E′ centres in a-SiO_2.[167] Furthermore, it has been suggested that the charge state of the E′ centre may be neutral and that it may be formed from an Si–H precursor.

In this chapter, atomic and molecular hydrogen interactions with bulk a-SiO_2 were investigated and shown to create two types of charge neutral defects. The first defect involves hole trapping at Si–H bonds in bulk a-SiO_2 and is shown to create neutral, paramagnetic E′ centres. The presence of a proton nearby is shown to significantly affect the defect's one-electron levels in the band gap. The interactions of atomic hydrogen with pure bulk a-SiO_2 have also been investivated. We find that hydrogen can bind to a bridging oxygen in bulk, stoichiometric a-SiO_2 to generate an under-coordinated Si defect centre facing a hydroxyl [O–H] group which shall be referred to

as a hydroxyl E′ centre herein. This hydrogen-induced defect is charge neutral and is thermodynamically stable over a wide range of Fermi levels including across the Si band gap, suggesting that it could be detrimental to electronic device applications of a-SiO_2. The origins of these defects and how they may play a role in electronic device and optical fiber reliability issues are discussed.

8.2 Calculation Details

The calculations presented in this chapter make use of both classical force-fields and *ab initio* theory to understand how H interacts with a-SiO_2. The ReaxFF [51] force-field was used to generate 116 models of amorphous SiO_2 each containing 216 atoms and periodic boundary conditions were employed, as described in chapter 3. In addition, twenty models of a-SiO_2 were generated with an extra hydrogen molecule introduced into the melting phase in order to study the formation of defects from Si–H bonds. Thus, these twenty models each contained 218 atoms. In order to ensure that Si–H bonds are present in the final structure, the distance between a single Si and H atom was fixed 1.46 Å apart and their coordinates frozen for the entire melt-and-quench procedure. After quenching these structures, they were further optimized using DFT as described in chapter 3. After the optimization, each model contained one Si–H bond and one O–H bond and there were no coordination defects in any of the models. An example of one of the models containing an Si–H and O–H bond is shown in Fig. 8.1.

Density functional theory (DFT), implemented in the CP2K code, was then used to further optimize geometries of all the structures. [27] The same technical details were used as are described in the calculation details of chapter 5.

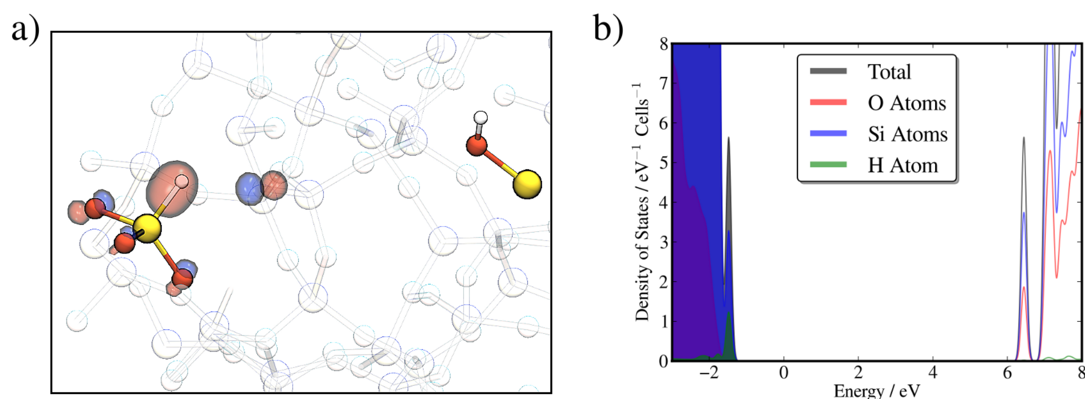

Figure 8.1: a) A model of a-SiO_2 containing an Si–H bond and an Si–O–H bond along with the HOMO of this system. The Si atoms are yellow spheres, O atoms are the darker red spheres H atoms are pale grey spheres. The distance between the Si–H bond and Si–O–H bond is ≈ 6 Å. b) Electronic density of states of a-SiO_2 containing an Si–H and O–H bond. They are projected onto Si, O and H atoms as well as showing the total density of states. A state associated with the Si–H bond sits just above the valence band.

8.3 Results of calculations

8.3.1 Atomic Hydrogen in a-SiO_2

Atomic hydrogen's interactions with a-SiO_2 have been studied in the literature.[172–174] Almost all theoretical studies confirm that atomic H occupies an interstitial position in SiO_2 and prefers to be in the positive or negative charge state depending on the system's Fermi level. That is, interstitial atomic H is not thermodynamically stable in the neutral charge state. In this section, we investigate whether neutral, atomic hydrogen can interact more strongly with the a-SiO_2 network using the DFT methods described in chapter 2.3. Atomic hydrogen was found to interact strongly with long Si–O bonds to produce a defect that is referred to as the hydroxyl E′ centre. The interaction of further atomic H with this centre is also discussed.

Interstitial Hydrogen Atom

As a reference calculation for hydrogen's interactions with a-SiO_2, we calculated the structure and energetics of an interstitial neutral H atom in 26 different a-SiO_2 matrices in order to build up the statistics required for a disordered sample. A single H atom was placed in a random position in each a-SiO_2 sample under the constraint

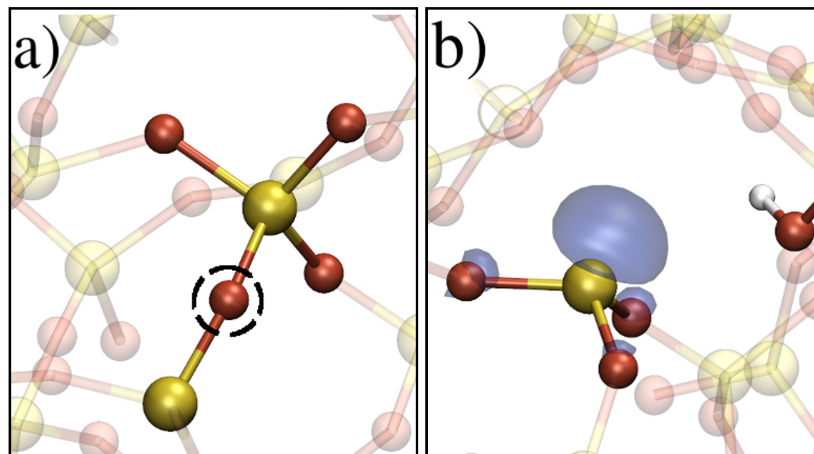

Figure 8.2: Atomic configuration and spin density of the hydroxyl E′ centre and its precursor. The Si atoms are the bigger yellow balls, the O atoms are the smaller red balls and the H atom is the small white ball in each configuration. The spin density are the blue, transparent polyhedra. a) This is an unperturbed SiO_4 tetrahedron. The circled bridging O center has a statistically long Si–O bond which acts as a precursor for the following hydrogen defect configurations. b) The hydroxyl E′ center. a 3-coordinated Si where the spin density is localised on the Si and its three O neighbors. The 3-coordinated Si faces a hydroxyl group.

that it was further than 2 Å away from any nearest neighbor. The total energy of each system was then minimized with respect to its atomic coordinates. Consistent with the literature, we find that interstitial H atoms do not bind and barely interact with a-SiO_2 matrices, with the nearest neighbors found at ≈ 2.6 Å. The spin density of the system is almost entirely localized on the H atom with an average Mulliken spin moment of 0.96 from the 26 systems. The electronic structures of the systems show that the H atom introduces a one-electron level which sits in the a-SiO_2 band gap; 0.7 eV on average and ranging from 0.1 to 1.2 eV above the valence band. The intersitial H atom can sit in any of the voids in a-SiO_2. As the structure is amorphous, the total energy of the system will be different depending on where the H atoms sits. To establish the range of interstitial H atom energies, we placed H in 10 different interstitial positions in the same a-SiO_2 structure and find that the range of total energies is spread over 0.2 eV. These results are in accord with what has been previously reported in the literature.[177]

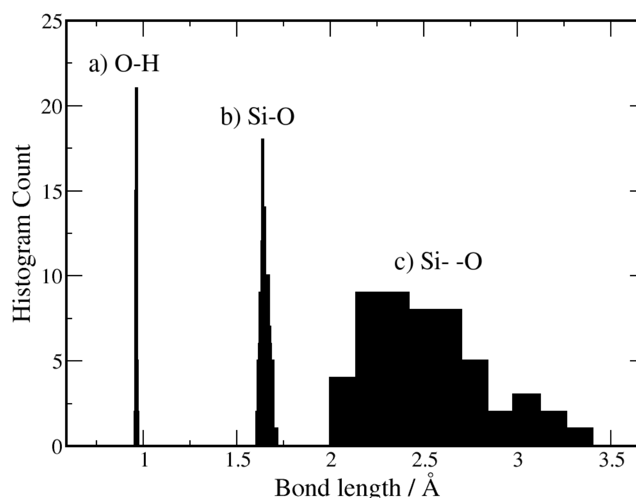

Figure 8.3: Histograms of the bond length distributions around the hydroxyl E′ center. a) Distribution of the O–H bonds of the hydroxyl group belonging to the hydroxyl E′ center. b) Distribution of the three Si–O bond lengths around the 3-cooordinated Si of the hydroxyl E′ center. c) Distribution of the Si- -O distance where the Si belongs to the 3-coordinated Si and the O belongs to the hydroxyl group [see Fig. 8.2]b. Note that '- -' indicates a non-bonding interaction in order to distinguish from the bonding interactions represented by '–'.

Neutral Atomic Hydrogen's Interactions with Bridging Oxygen Sites

To investigate whether a neutral H atom interacts more strongly with O sites in the a-SiO_2 network, we placed it at a distance of 1 Å from bridging O atoms in 116 different a-SiO_2 samples [see Fig. 8.2a]. These geometries were optimized resulting in a new type of defect described below.

Hydroxyl E′ Centre

When atomic hydrogen was placed 1 Å away from long Si–O bonds, shown in Fig. 8.2a, a defect was formed which resembles an E′ centre, i.e. a 3-coordinated Si atom with an unpaired electron,[166] facing a hydroxyl group, shown in Fig. 8.2b. It is therefore referred to as the hydroxyl E′ centre. Preliminary calculations whereby H atoms were placed at random Si–O bonds showed that this defect configuration formed predominantly at long ($>$ 1.65 Å) Si–O bonds. The concentration of such bonds in the a-SiO_2 models discussed in chapter 3 is 2.2%. To obtain a statistical distribution of the hydroxyl E′ centre's properties, H atoms were placed 1 Å away from O atoms

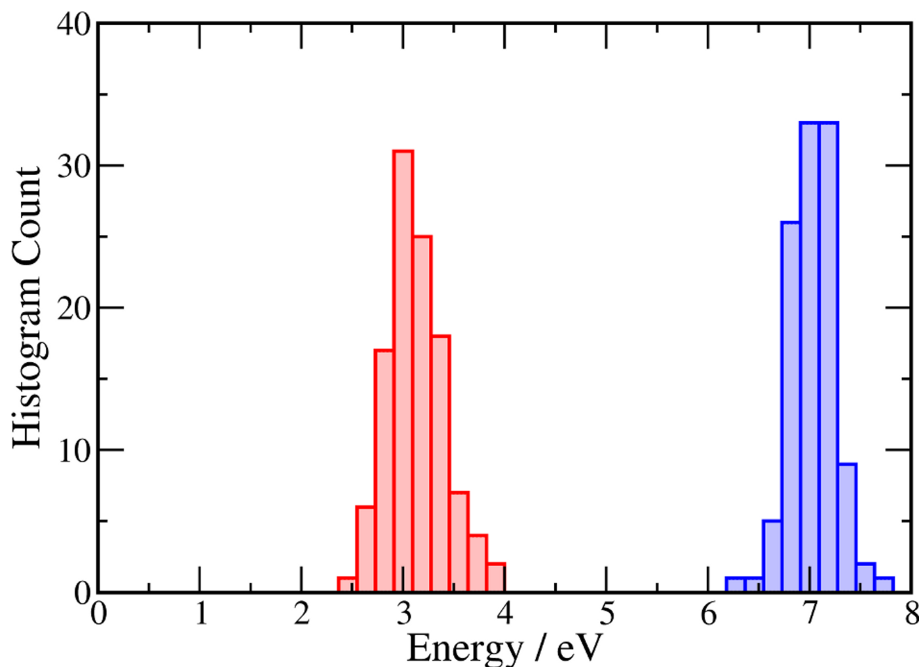

Figure 8.4: Histogram of the one-electron level of 116 configurations of the hydroxyl E′ centre. The energy scale starts from 0.0 and finishes at 8.1 eV; this is the a-SiO_2 band gap as calculated using the PBE0_TC_LRC functional. The area of the histograms which are coloured dark red show occupied states while the area of the histograms which are coloured blue show the unoccupied states.

associated with long Si–O bonds in 116 different a-SiO_2 matrices and their geometries were optimized. In all the systems, this resulted in the H atoms breaking an Si–O bond, forming an $O_3{\equiv}Si^{\bullet}$ centre facing a hydroxyl group as illustrated in Fig. 8.2b. The O–H bond averages at 0.99 Å and shows a very narrow distribution, as can be seen in Fig. 8.3a. The Si–O bonds of the $O_3{\equiv}Si^{\bullet}$ moiety average at 1.65 Å and their distribution can be seen in Fig. 8.3b, while the distance between the Si and the O from which it dissociated averages at 2.63 Å, a very wide distribution as can be seen in Fig. 8.3c. The average Mulliken spin moment of the 3-coordinated Si is 0.90, ranging from 0.84 to 0.98, indicating that the unpaired spin is highly localized on the Si centre. Its average Mulliken charge is $+1.08\ |e|$, relatively lower than the average Mulliken charge of bulk, 4-coordinated Si sites from 116 models of defect-free a-SiO_2 of $+1.42\ |e|$, indicating that this 3-coordinated Si centre is more negative than the average Si site in a-SiO_2. The nascent Si dangling bond introduces a one-electron state 3.12 eV above the a-SiO_2 valence band on average, almost resonant with the top of the Si valence band (c.f. Si/SiO_2 valence band offset[107]). Fig. 8.4 shows the

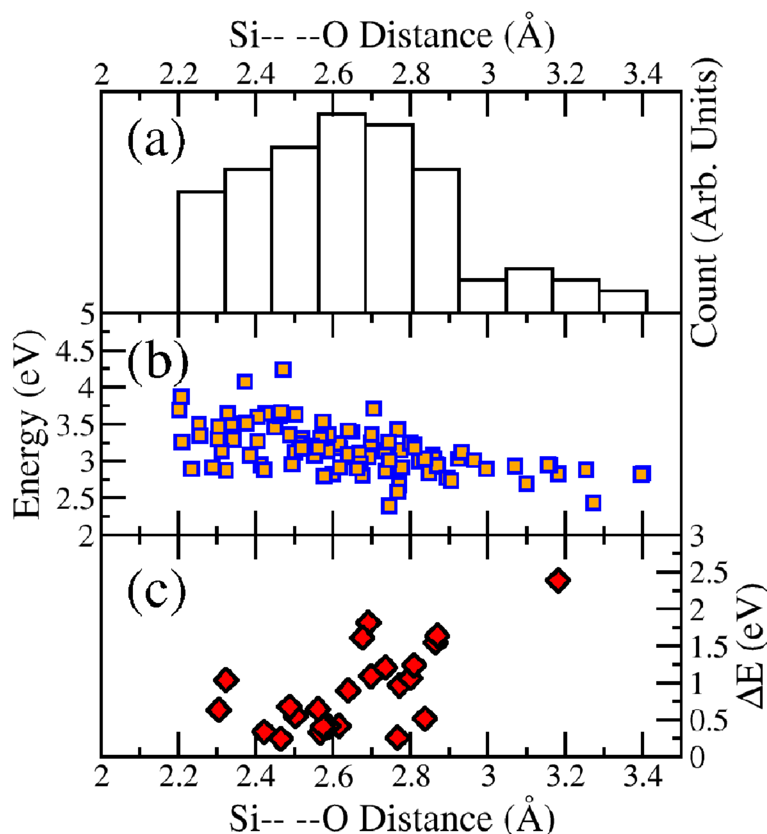

Figure 8.5: Correlations between the one-electron levels and relative stabilities of the hydroxyl E′ centre with the non-bonding Si– –O interaction. (a) A histogram of the distribution of the Si– –O distances of the dissociated Si–O bond in the hydroxyl E′ centre [see Fig. 8.2b]; (b) energies of the one-electron defect levels with respect to the top of the a-SiO_2 valence band plotted against the Si– –O distance; (c) the relative stability of the hydroxyl E′ with respect to an interstitial H atom, plotted against the Si– –O distance.

position of the occupied and unoccupied one-electron levels of the hydroxyl E′ centre within the a-SiO_2 band gap. It is interesting to note that from the 116 configurations, a normal distribution of electronic states emerges.

The non-bonding Si– –O distances correlate strongly with some of the defect's properties. Fig. 8.5a shows a histogram of the non-bonding Si– –O distance. The position of the one-electron defect level with respect to the top of the valence band is plotted against this distance and is shown in Fig. 8.5b. The average position of the one-electron level is 3.1 eV above the a-SiO_2 valence band. The further away the Si and the negative O ion are from each other, the deeper (closer to the top of the valence band) the defect level becomes. This may be due to the reduction in repulsion between the unpaired electron and the O ion. This reduction in repulsion energy also

increases the relative stability of the hydroxyl E′ centre with respect to an interstitial H atom, as seen in Fig. 8.5c.

The hydroxyl E′ centre is by far more thermodynamically stable than an interstitial H atom, being lower in energy by 0.9 eV on average and ranging from a minimum of 0.3 eV to a maximum of 2.3 eV lower than the interstitial H atom. We have calculated the formation energies of 50 configurations each of the hydroxyl E′ centre and an interstitial H atom with respect to the Fermi level of the system according to equation B.1 in the appendix. The configurations utilized in these calculations are shown in Fig. 8.6a. Note that the term interstitial was chosen purely to maintain consistency with previous studies of hydrogen in SiO_2, despite the fact that the charged variants are interesting defects in their own right, but a detailed discussion on them is beyond the scope of this thesis. Remarkably, we find a number of configurations of the hydroxyl E′ centre are thermodynamically stable in the the neutral charge state over a range of Fermi levels (an example of which is shown in Fig. 8.6b), in stark contrast to what has been calculated for interstitial hydrogen in the literature.[172,174] We find that 15 of the 50 configurations studied are more stable as the neutral hydroxyl E′ centre across a range of Fermi levels.

Thermodynamic switching levels are the Fermi levels for which the formation energies of two different charge states of a defect are equal. For example, the (+/0) thermodynamic switching level is the Fermi level for which the formation energies of the positive and neutral charge states are the same. A histogram of these levels is shown in Fig. 8.7. For the configurations in which the (+/-) switching level was lower, only this value was recorded; however, in the systems where (+/0) is lower, the (+/0) and (0/-) levels were recorded. This histogram shows that the neutral hydroxyl E′ centre can be stable over a wide range of Fermi levels, from ≈ 3.5 to just under 6 eV above the a-SiO_2 valence band in our calculations. Note that it is not necessarily a single configuration that is stable over this range. This range overlaps strongly with the position of the Si band gap, indicating that the hydroxyl E′ centre will contribute to the more thermodynamically stable hydrogen interactions in the

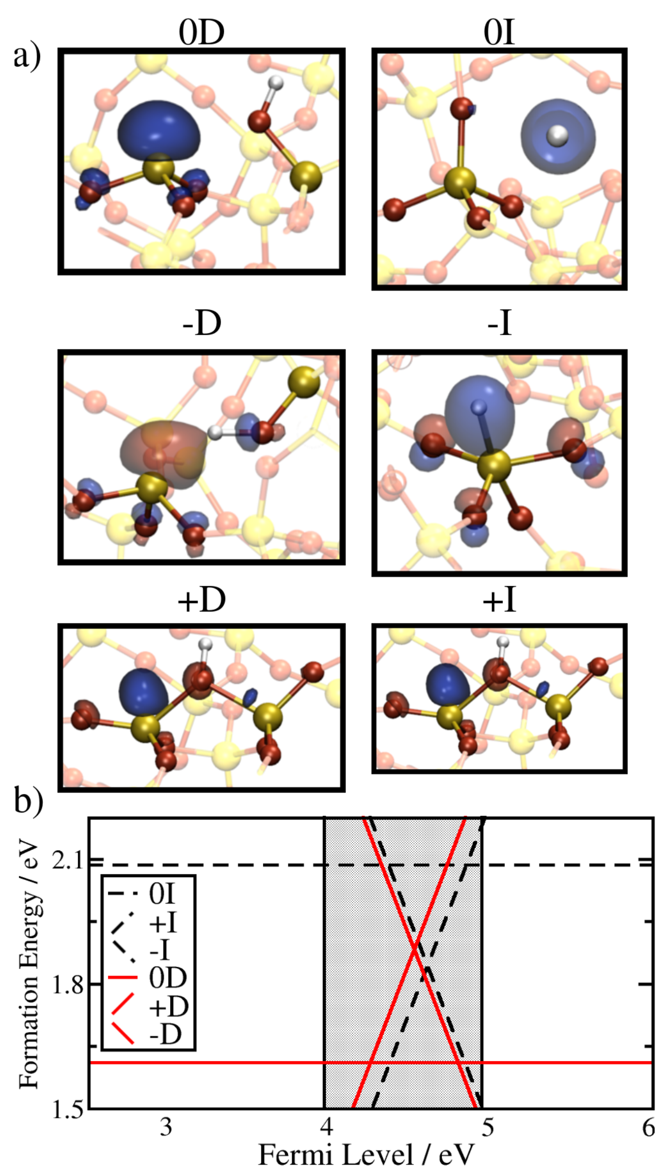

Figure 8.6: Formation energy of the hydroxyl E′ centre in a-SiO_2. a) Configurations of the hydroxyl E′ centre and interstitial hydrogen atom used in the calculations of the formation energies. The configurations are labelled as 0, +, and - for the neutral, positive and negative charge states respectively, with D and I standing for defect and interstitial, respectively. b) Plot of the formation energy versus the Fermi level (with respect to the a-SiO_2 valence band) of a single configuration of the hydroxyl E′ centre and an interstitial H atom. Formation energies corresponding to the hydroxyl E′ centre are drawn as solid red lines while the interstitial H atom's formation energies are drawn as dashed black lines. This diagram clearly shows that the neutral hydroxyl E′ centre (lower horizontal solid red line) is the most stable charge state across a range of Fermi levels.

Si/SiO_2 systems widely used in microelectronic devices. We have also calculated the hyperfine splitting due to the unpaired electron's interaction with the matrix in 13 configurations. There is a strong isotropic hyperfine splitting resulting from the interaction of the 3-coordinated ^{29}Si with the localized electron which averages at 48.4 mT and ranges from 44.1 to 52.2 mT. This value shows a similarity to the experimental isotropic hyperfine splitting for the E′ centre in a-SiO_2 which was measured as 42.0 mT.[101]

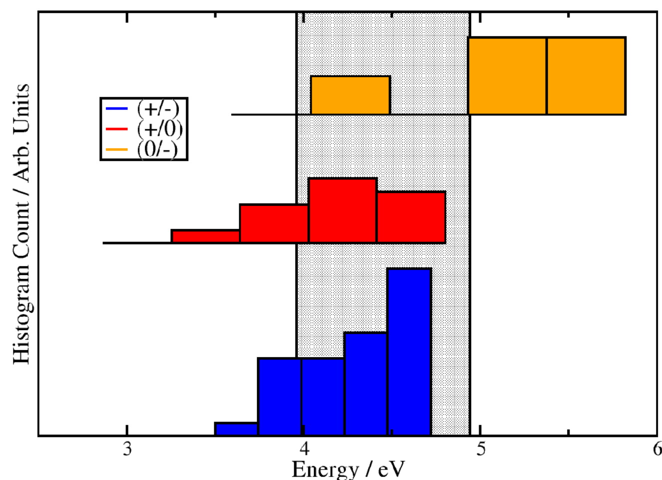

Figure 8.7: Histogram of the thermodynamic switching levels of the hydroxyl E′ centre. This shows that the neutral hydroxyl E′ centre can be stable over an ≈ 2.5 eV range of the Fermi level. The position of the Si band gap is the shaded section.

To investigate the formation of the hydroxyl E′ centre, the barrier from an interstitial H to the defect configuration was calculated using the CI-NEB method described in chapter 2.6 in 13 different models. A schematic of this reaction along with the calculated barriers is shown in table 8.1 labelled as Reaction 1. The barriers range over 1.0 eV due to the slight variations in geometry of each amorphous structure, clearly emphasising the importance of obtaining statistics when modelling amorphous SiO_2 and demonstrating that there are some configurations where it will be much more likely for an atomic H to create this defect configuration. We note that the distribution of calculated barriers is highly asymmetric and does not result in a normal distribution. This is again due to the variations in the a-SiO_2 structures, where each local chemical environment modulates the calculated barrier.

Passivation of the E′ centre and 3-coordinated Si defects in a-SiO_2 is experimen-

tally known to occur,[165] with the electron spin resonance (ESR) signal of the E′ centre significantly reduced after a soak in an ambient of H_2 or forming gas.[178] We investigated the passivation of the hydroxyl E′ centre in the presence of atomic hydrogen. To study the passivation, an H atom was placed 1 Å away from the undercoordinated Si defect centre in 26 different systems and their total energies were optimized. We find that this defect is indeed passivated by H, forming a stable Si–H bond which averages at 1.45 Å, ranging from 1.43 Å to 1.46 Å. The defect level that was ≈ 3 eV above the valence band in the neutral configuration is now suppressed and sits instead at the top of the a-SiO_2 valence band. The binding energy of the Si–H bond was calculated as:

$$E_{Binding} = E^{Tot}_{Interstitial} - E^{Tot}_{Si\text{–}H}. \tag{8.1}$$

where $E^{Tot}_{Interstitial}$ is the total energy of a system with the 3-coordinated Si defect and an interstitial H atom sat in an Si–O void and $E^{Tot}_{Si\text{–}H}$ is the total energy of the system after the defect has been passivated. The calculated binding energy for the nascent Si–H bond reveals that it is strong, averaging at 4.19 eV and ranging from 3.96 to 4.31 eV calculated from 13 systems. Reaction 2 in table 8.1 shows this reaction and its binding energies. The Si–H bond in a-SiO_2 seems to have a narrow range of bond lengths and binding energies in contrast to the energies associated with the Si and O atoms, such as the position of the defect level in the band gap and even the Si–O bond length distributions. This suggests that the Si–H bond formed is very stable and that the passivation is very effective.

8.3.2 Molecular hydrogen in a-SiO_2

In this section we look at how molecular hydrogen interacts with a-SiO_2. In particular, we focus on two specific cases. The first is the introduction of an H_2 molecule into the melting phase when generating the a-SiO_2 models. Introduction of H_2 generates Si–H bonds which can lead to the formation of defects. The second case we look at is the interaction of a hydrogen molecule with defect-free a-SiO_2 lattices. Again, this creates Si–H bonds which act as precursors to defect configurations. These two cases

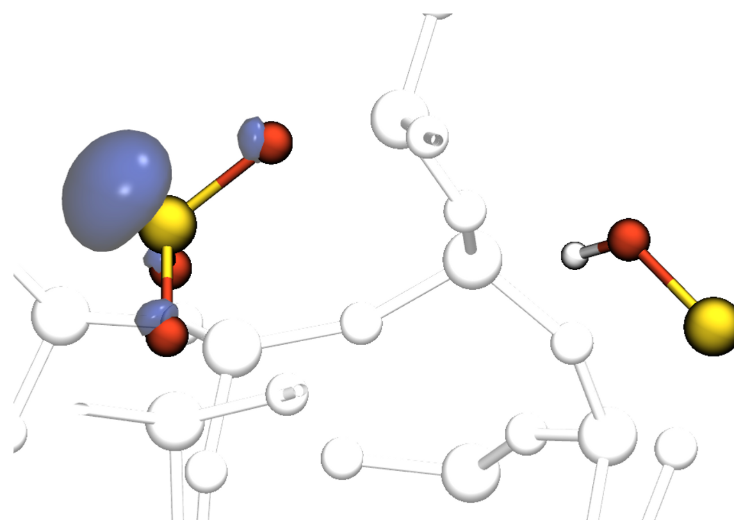

Figure 8.8: Atomic structure and spin density of the neutral E′ centre. The O–H bond that remains in the a-SiO_2 structure is highlighted on the right hand side of the figure. It is located 6 Å away from the 3-coordinated Si.

are described in detail below.

Neutral E′ Centres from Si-H Bonds

As discussed in the calculation details, twenty models of a-SiO_2 were generated with an extra H_2 molecule added during the melt procedure. This resulted in each model containing a single Si–H and O–H bond, as can be seen in Fig. 8.1. The Si–H bonds in these models introduce a state that sits near the top of the a-SiO_2 valence band, as can be seen in the density of states shown in Fig. 8.1. Starting from these optimized models, a H atom was removed from the Si–H bond in each structure and their geometries were reoptimized. This resulted in a single electron residing in a dangling bond at what is now a 3-coordinated Si, as illustrated in Fig. 8.8. This defect structure is very similar to what is known as the E′ centre[166] and the system is charge neutral, therefore it is referred to as the neutral E′ centre herein. As can be seen in Fig. 8.8, the spin density is highly localized in a dangling bond at this 3-coordinated Si. The 3-coordinated Si introduces a state in the a-SiO_2 band gap, which sits 3.0 eV above the valence band on average from the 20 models. Its average Mulliken charge from the 20 different models is +1.07 $|e|$, significantly lower than the average of +1.42 $|e|$ of bulk Si atoms in these models. Its average Mulliken spin moment taken

over the 20 models is 0.89 and ranges from 0.88 to 0.92, further confirming that the electron is indeed highly localized at the 3-coordinated Si. The isotropic hyperfine splittings were calculated in 8 models. The most dominant contribution comes from the 3-coordinated Si, with a splitting that averagest at 44.4 mT and ranges from 40.0 to 47.8 mT.

We now turn to how the aforementioned defect configuration can be formed starting from an Si–H bond. The bond would need to break and the H atom would diffuse away. This reaction can be described by the following equation.

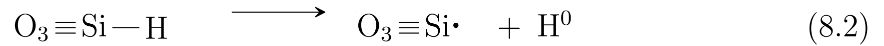

$$O_3\equiv Si-H \longrightarrow O_3\equiv Si\cdot + H^0 \tag{8.2}$$

The formation energy of this reaction was calculated as the total energy difference between the reactants and the products.

$$E^{For}_{NeutralE'} = E^{Tot}_{Si-H} - E^{Tot}_{3cSi} \tag{8.3}$$

Where $E^{For}_{NeutralE'}$ is the formation energy, E^{Tot}_{Si-H} is the total energy of the system that contains an Si–H bond and E^{Tot}_{3cSi} is the total energy of the system when an H atom is moved away from the $O_3\equiv Si\cdot$ moiety. The H atom that was moved sits in an interstitial position as described in section 8.3.1. The average formation energy obtained from the 20 a-SiO_2 models is 4.2 eV, which indicates that the Si–H bond is very stable and would require high temperature for thermally activated dissociation to occur.

As the Si–H states sit near the top of the valence band, we then investigated whether hole trapping would facilitate the Si–H dissociation in all 20 a-SiO_2 models, as in reaction:

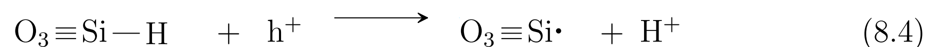

$$O_3\equiv Si-H + h^+ \longrightarrow O_3\equiv Si\cdot + H^+ \tag{8.4}$$

where h^+ is a hole. In the neutral system the Si–H states are located close to the

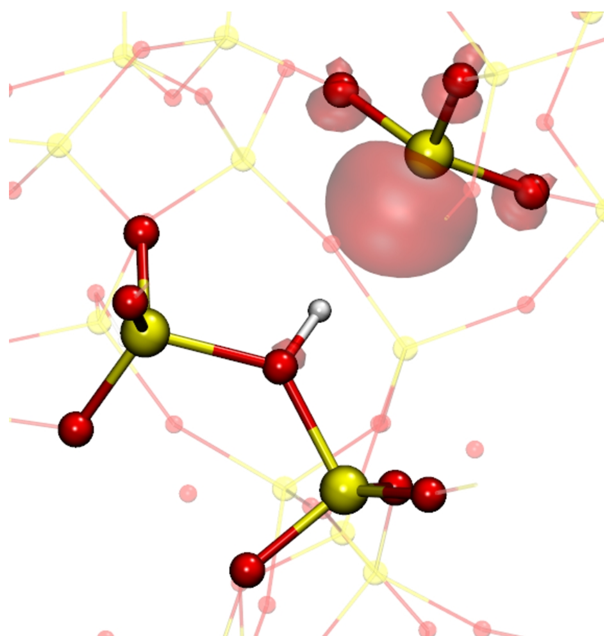

Figure 8.9: The neutral E′ centre formed by trapping a hole at an Si–H bond. An unpaired electron localised on a 3-coordinated Si atom and a proton bound to a bridging oxygen can be clearly seen in the figure. The H in this figure is a proton.

top of the SiO_2 valence band. In two of the 20 models, addition of a hole results in spontaneous dissociation of a Si–H bond releasing a proton and leaving behind a neutral E′ centre. The proton binds to the nearest oxygen that is not bonded to the Si atom from which the proton dissociated, as can be seen in Fig. 8.9. The Si–H states of the two models in which the Si–H bond dissociated spontaneously are the highest in the a-SiO_2 band gap, sitting slightly above the top of the SiO_2 valence band. These are also the configurations that have the smallest H– –O distance with the O atom which binds the proton, as can be seen in Fig. 8.10. In the remaining 18 models there is a barrier to remove a proton, but the final defect state is always lower in energy than the Si–H state just after the hole trapping. The barriers for removing the H^+ after hole trapping was calculated using CI-NEB. The barrier to proton removal increases as the H. . .O distance increases. In our 20 models, this barrier does not exceed 0.5 eV even when the proton has to cross the largest H. . .O distance of 3.2 Å.

In all cases the proton binds to an oxygen atom that sits across an Si–O void, forming a hydronium-like configuration shown in Fig. 8.9 and leaving behind a 3-

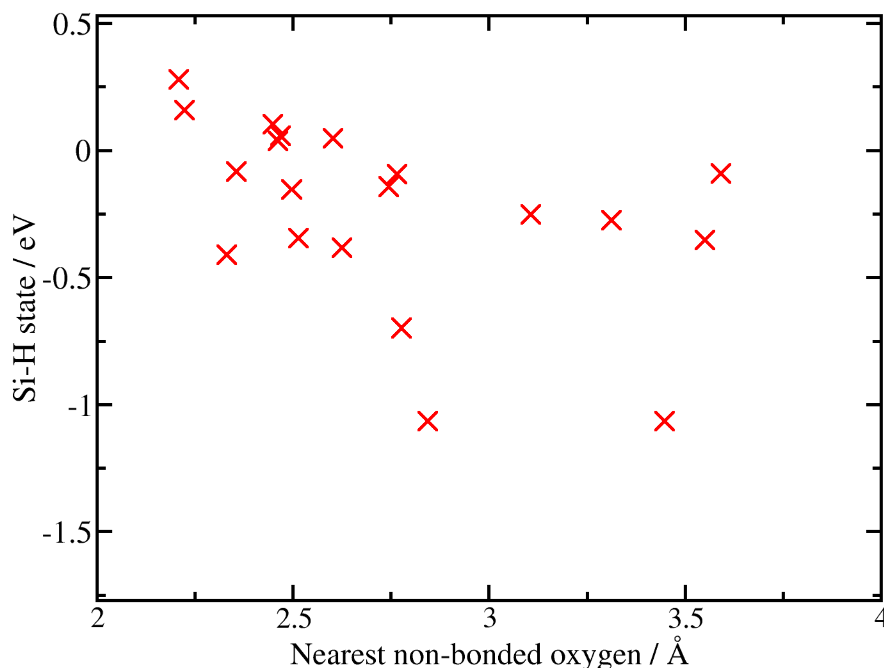

Figure 8.10: A graph showing how the energetic position of the Si–H state, measured with respect to the top of the a-SiO_2 valence band, changes with the nearest non-bonding oxygen distance. There is a clear anti-correlation, with the defect level moving further into the valence band as the nearest non-bonding oxygen moves further away.

coordinated Si atom with an electron localized on this Si atom. Moving the proton to one of the O atoms belonging to the same tetrahedron as the 3-coordinated Si is also energetically favourable, but requires overcoming a higher barrier of 0.6 eV, as opposed to the 0.5 eV maximum required to cross a ring. The average relaxation energy, from our 20 systems, for a proton dissociating and binding to an oxygen atom across the ring is 0.66 eV. However, an electron can be trapped by an E′ centre with a proton less than $\approx$ 3 Å away, leading to restoration of the Si–H bond. When the proton is further away, the Si–H bond does not reform.

Although the majority of the hyperfine splitting comes from the interaction of the unpaired electron with the nucleus of the Si atom on which it is localized (see Fig. 8.9), the hyperfine interaction with the proton is also possible if the Si. . .H distance is small enough. If the Si. . .H distance is 2.3 Å or less, this hyperfine splitting is 1.6 mT on average.

Comparison of the one-electron states of the E′ centre with the proton less than

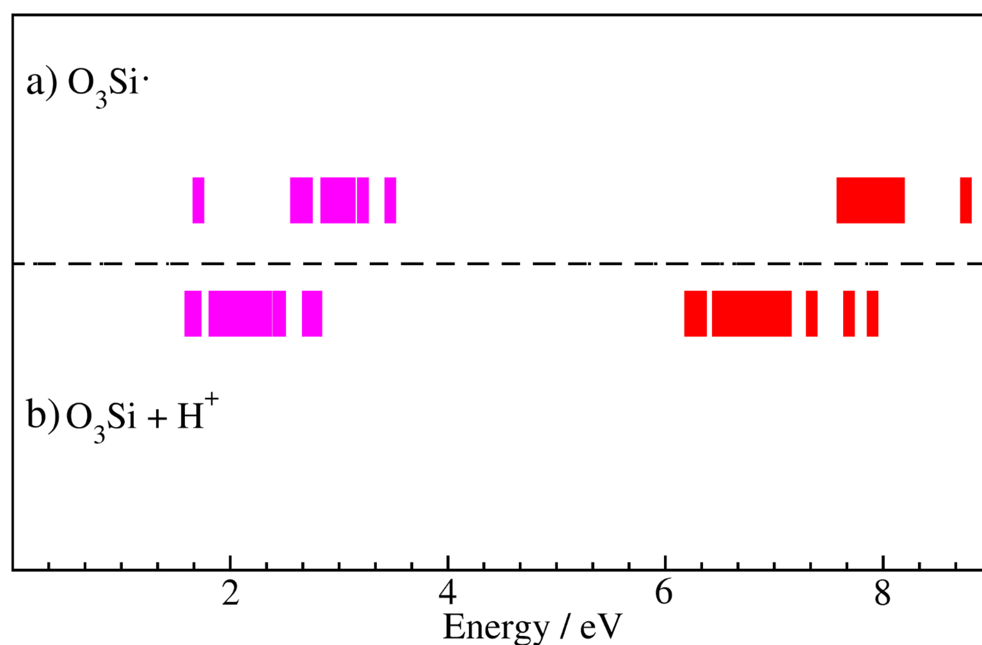

Figure 8.11: The effect of a nearby proton on the defect levels of the neutral E′ centre. a) The defect levels of the neutral E′ centre. b) The defect levels of the neutral E′ centre when a proton is placed less than 6 Å away. The defect's levels are shifted closer to the valence band when a proton is nearby.

6 Å away and a neutral E′ centre with no proton in the system reveals that the proton can shift the defect states down by up to ≈ 0.5 eV. That is, the defect state is highly dependent on the proton's location. Fig. 8.11 shows the defect levels for a system containing a $O_3{\equiv}Si\cdot$ moiety and the same system with a proton located less than 6 Å away. It can clearly be seen that the defect levels of the system with a proton are shifted down. The position of the proton depends on how easily the proton can diffuse through a-SiO_2. It has been suggested by Pasquarello *et al.* that proton diffusion occurs predominantly via a ring-crossing mechanism.[179] This involves the proton hopping from one oxygen to another across an Si-O ring. Barriers for this hopping range from almost zero to ≈ 1.5 eV, dependent on the distance between the initial and final O atoms. We also find that proton diffusion proceeds via ring-crossing with the E′ centre making little difference to the energies previously calculated for proton diffusion.[179] This means that the defect's level will be modulated by the protons that exist nearby.

Hydroxyl E′ Centre from H_2 Molecules

We now turn to the question of whether interaction of a H_2 molecule with a pristine, stoichiometric a-SiO_2 matrix can result in a passivated configuration of the hydroxyl E′ centre without initial creation of the active defect. In 10 different configurations of bulk a-SiO_2, H_2 molecules were placed in interstitial positions and their geometries were optimized. Hydrogen molecules sit in the middle of an Si–O void and interact negligibly with the a-SiO_2 matrix, similar to the interstitial H atoms described earlier in section 8.3.1 and in good agreement with what has been previously calculated in the literature.[86,180] Passivated defect structures were then generated by forming an Si–H bond and an O–H bond facing each other at a long Si–O bond and the geometry of each configuration was then optimized, as described in section 8.3.1. We find a variation in the qualitative stabilities of the passivated defect structures, being more thermodynamically favourable than interstitial H_2 molecules by 0.2 eV on average, but ranging from 0.61 more to 0.29 eV less stable. The barrier to form the passivated configuration from an interstitial H_2 molecule was then calculated using the CI-NEB method with the interstitial H_2 and passivated configuration described above used as the initial and final images respectively. A summary of the reaction and its barriers are presented as Reaction 3 in table 8.1. The barriers for the forward reaction average at 1.74 eV while they average at 1.94 eV for the reverse reaction. The forward barrier is relatively high and would require a high temperature to overcome and form a passivated hydroxyl E′ centre, but the reverse barrier indicates that once it is formed it would be kinetically very stable.

H_2 Cracking at Hydroxyl E′ Centres

Previous theoretical studies have investigated the reaction kinetics of a H_2 molecule cracking at an E′ centre, passivating the defect and leaving behind an interstitial H atom.[175,176,178] This reaction has been shown to be endothermic at multiple levels of theory, i.e., the passivated configuration is thermodynamically unfavourable with respect to the active defect and an interstitial H_2 molecule. We have performed sim-

Reaction	Forward Reactions Min.	Forward Reactions Max.	Forward Reactions Avg.	Reverse Reactions Min.	Reverse Reactions Max.	Reverse Reactions Avg.	ΔE
Hydrogen reactions in defect free a-SiO_2							
1) $O_3{\equiv}Si{-}O{-}Si{\equiv}O_3 + H^0 \rightleftharpoons O_3{\equiv}Si{\cdot}\ \ HO{-}Si{\equiv}O_3$	0.50	1.71	0.91	1.25	2.40	1.66	-0.75
2) $O_3{\equiv}Si{\cdot}\ \ HO{-}Si{\equiv}O_3 + H^0 \longrightarrow O_3{\equiv}Si{-}H\ \ HO{-}Si{\equiv}O_3$	0.00	0.00	0.00	3.96	4.31	4.19	-4.19
3) $O_3{\equiv}Si{-}O{-}Si{\equiv}O_3 + H_2 \rightleftharpoons O_3{\equiv}Si{-}H\ \ HO{-}Si{\equiv}O_3$	1.07	2.15	1.74	1.57	2.45	1.94	-0.20
4) $O_3{\equiv}Si{\cdot}\ \ HO{-}Si{\equiv}O_3 + H_2 \rightleftharpoons O_3{\equiv}Si{-}H\ \ HO{-}Si{\equiv}O_3 + H^0$	0.46	0.78	0.65	0.10	0.24	0.20	0.45

Table 8.1: Hydrogen's reactions with a-SiO_2. All results are in eV.

ilar calculations at the hydroxyl E′ centre and a schematic is shown as Reaction 4 in table 8.1. Starting from the neutral configuration of the hydroxyl E′ centre, an H_2 molecule was placed within 2 Å of the defect and the geometry of the system was optimized. The H_2 remains in an interstitial position and interacts with neither the defect nor the a-SiO_2 matrix. Using this configuration and the passivated configuration with an extra interstitial H atom, we used CI-NEB to calculate the barrier for the passivation of the undercoordinated Si by an H_2 molecule in 13 models. The calculated barriers are qualitatively similar to previous calculations of H_2 dissociation at E′ centres,[175,176,181] with the defect configuration in the presence of a H_2 molecule being thermodynamically favourable by 0.45 eV on average, ranging from 0.22 to 0.68 eV more stable. The barrier for passivation from an interstitial H_2 molecule averages at 0.65 eV, ranging from 0.46 eV to 0.78 eV. However, the reverse barrier is much lower and averages at 0.20 eV, ranging from 0.10 eV to 0.24 eV. Similar to the Si–H binding energies, these barriers exhibit a much narrower range and seem to be more resistant to fluctuations in the local environment of the a-SiO_2 matrix.

8.4 Discussion and Conclusions

Our modelling confirms that Si–H bonds in a-SiO_2 can act as precursors to formation of neutral E′ centres and that the presence of strained Si–O bonds in a-SiO_2 gives rise to an additional channel of interaction of H atoms with a-SiO_2 networks, predicting the formation of a hydroxyl E′ centre.

The Si–H dissociation is facilitated by hole injection and the barrier to Si–H dis-

sociation is at most 0.5 eV in our models. Proton diffusion away from the neutral E′ centre occurs via a ring crossing mechanism with barriers less than 1.5 eV. Electron injection can restore the Si–H bond if the proton is less than 3 Å away. The hyperfine interaction of the neutral E′ centre is in good agreement with the experimental values. This defect introduces a one-electron level that sits 3.0 eV on average above the SiO_2 valence band. This position makes this defect a candidate for the defects that could be involved in electronic device reliability issues. An interesting aspect of this model is the 1.6 mT signal associated with the proton. Experimentally there is a weak satellite signal of 1.3 mT associated with the E′ centre controversially attributed either to a ^{29}Si atom[182] or hydrogen atoms.[183] Our calculations suggest that this satellite signal may be related to hydrogen present in the system after Si–H dissociation. Experimentally the 1.3 mT signal has been seen to disappear at temperatures greater than 100° C while the E′ signal is increasing.[184] In this model the proton can diffuse away after overcoming some barrier, presumably leading to a disappearance of the 1.6 mT signal, even while neutral E′ centres are being generated.

The hydroxyl E′ was shown to have deep levels in the a-SiO_2 band gap, which are nearly resonant with the top of the Si valence band. Some configurations are stable in the neutral charge state over a range of Fermi level positions in the a-SiO_2 band gap. These results demonstrate that the hydroxyl E′ centre could have an effect on the technological applications of a-SiO_2. Its defect levels are located close to the top of the Si valence band in a Si/SiO_2 system (see Fig. 8.4), typically used in metal-oxide-semiconductor (MOS) electronic devices. Holes at the top of the Si valence band, typical of a pMOS device, can tunnel into the hydroxyl E′ centre so that it can act as a source of trapped charge in such a device. Hence H^0 is not always a benign agent in defect-free a-SiO_2 networks and can produce thermodynamically stable neutral defects in a-SiO_2, adding to the density of dangling bond defects, such as E′ centres, which are implicated in reliability issues of devices which utilize a-SiO_2. The results presented for atomic hydrogen's interactions with a-SiO_2 may also shed new light on the behaviour of atomic hydrogen in other amorphous solids, in which H^0 is thought

to interact negligibly.[172]

Both the neutral E′ and hydroxyl E′ centres have defect levels which sit in similar positions in the a-SiO_2 band gap, ≈ 3.5 eV above the valence band. In an Si/SiO_2 system, this state would sit near the top of the Si valence band and holes could potentially tunnel into these states. Thus they would be detrimental to the operation of an electronic device made using this system. Furthermore, the position of the defect levels suggests that they could absorb radiation in the ultra-violet range of the spectrum. Further calculations would need to be performed to calculate their optical absorption spectra and assess how detrimental these defects would be to optical devices.

The reactions of hydrogen species with defect-free a-SiO_2 are summarized in table 8.1. Our results for H_2 dissociation at the hydroxyl E′ centre can explain the slow passivation kinetics of the E′ centre signals under an H_2 atmosphere. The barrier to H_2 cracking and passivation is quite high while the final configuration is thermodynamically unfavourable in the presence of an H atom, indicating that the passivation reaction would proceed rather slowly. It is also important to note the consequence of the backwards reactions, which essentially re-activates the passivated defect. The barriers for the de-passivation reactions are rather low and, if a source of atomic H exists in the system, it can de-passivate Si–H bonds and activate a hydroxyl E′ centre. Notably, the de-passivation reactions studied are also similar to the experimentally observed de-passivation of the P_b centre, a defect consisting of a 3-coordinated Si with a trapped electron, which exists at the Si/SiO_2 interface.[185] The de-passivation reaction is insensitive to how the passivated configuration was generated in the first place and is only limited by the concentration and diffusion of atomic H in the system. Atomic H can be released into the a-SiO_2 layer in metal-oxide-semiconductor (MOS) devices in a number of conditions.[186–188] Coupled with the results for the de-passivation reactions and the positions of the hydroxyl E′ defect levels, these results strongly suggest that the hydroxyl E′ can be a potentially detrimental defect for electronic and optical technologies.

9

Concluding Remarks

9.1 Summary

A number of novel charge trapping defects in SiO_2 were investigated in this thesis. They were shown to strongly affect their local atomistic surroundings and significantly change the electronic structure of the oxide. Defects such as this can significantly affect the operation of an electronic device and their electronic structures show that they could be involved in device reliability issues.

Extrinsic sites in SiO_2 were shown to trap electrons. Substitution of an Si atom with Ge in α-quartz results in a GeO_4 tetrahedral structure, similar to the SiO_4 tetrahedral unit but with longer Ge–O bonds. This Ge atom is associated with a state which sits just below the α-quartz conduction band in the neutral system. Addition

of an electron causes a significant structual rearrangement around the Ge impurity. Two of the Ge–O bonds extend significantly and the angle between these two bonds is severely distorted (150°) from the ideal tetrahedral angle (109.5°). The extra electron was found to localize on this wide angle. The state on which the electron localises lies deep in the α-quartz band gap, 4.2 eV below the conduction band, making it a deep electron trap. An interstitial Li atom in α-quartz was also investigated. In the neutral charge state, it was found to sit equidistantly between two SiO_4 tetrahedra. The Li atom introduces an occupied state which sits just below the bottom of the α-quartz conduction band. However, opening a nearby O–Si–O angle resulted in an electron trapped at that site, similar to the that of Ge-doped α-quartz. A defect state sits 2.5 eV below the conduction band and an electron was shown to have transferred onto an Si site. The calculated hyperfine splittings of the trapped electron are in good agreement with the experimental signals of the $[SiO_4/Li]^0$ centre in α-quartz.[118] This was the first time that the atomistic structure of the $[SiO_4/Li]^0$ was calculated.

Electrons were also shown to spontaneously trap at *intrinsic* sites in a-SiO_2. These traps create a defect state which sits 3.2 eV below the conduction band on average. The precursor sites at which electrons could trap were shown to be wide O–Si–O angles. By constructing a model of a-SiO_2 which contains almost half a million atoms, the concentration of these precursor sites was estimated as 4×10^{19} cm^{-3}. Although this concentration is rather high when compared to that of a typical point defect in a-SiO_2, for example, the oxygen vacancy, experimental results on SiC/SiO_2 electronic devices show a similar concentration of electron traps which are not attributed to any existing defect. The optical absorption spectra of these electron traps were calculated in an embedded cluster model using TD-DFT for the first time. The calculated spectra show a strong absorption at 3.7 and 5.8 eV. These peaks are in good agreement with experimental measurements at low temperatures, providing the strongest evidence yet for intrinsic electron trapping in a-SiO_2. The position of the defect levels suggest that they could indeed play a role in electronic device reliability issues.

Finally, Hydrogen's interactions with SiO_2 were investigated as it is widely used in

electronic device fabrication processes. It was shown that both atomic and molecular hydrogen can be involved in defect generation processes. Introduction of molecular hydrogen into the melted phase of SiO_2 followed by quenching results in Si–H bonds. They were shown to interact with holes to generate a neutral 3-coordinated Si defect which is referred to as the neutral E′ centre. During this process, a proton is liberated and binds to a nearby bridging O. The distance between this liberated proton and the 3-coordinated Si has a strong effect on the defect's level in the SiO_2 band gap. Atomic hydrogen was also shown to generate defects. In particular, it can interact with bridging O at long Si–O bonds to generate a defect which has not been previously characterized in the literature. It consists of a 3-coordinated Si facing a hydroxyl group and is referred to as the hydroxyl E′ centre. Both the neutral and hydroxyl E′ centres have defect levels which suggest that they can both be involved in device reliability issues.

9.2 Future Work

This thesis investigated a number of defects in SiO_2 using hybrid functionals and DFT. Despite being characterised extensively, this work can be extended in a number of directions.

A common theme of the intrinsic electron traps (see chapter 6) and the hydroxyl E′ centre (see chapter 8) is that the disorder of a-SiO_2 allows for creation of novel defects. Many other amorphous materials are now being considered for use in electronic and other technological applications. For instance, hafnium dioxide is now regularly used in electronic devices as a replacement for SiO_2, and studies show that it is deposited in its amorphous state.[189,190] Understanding the role of disorder in defect creation in other materials used in technological applications would help in producing more reliable devices.

It is important to consider what nuclear quantum effects may have on the results presented for the hydrogen related defects in chapter 8. These effects are known to

play a large role in systems such as water and ice due to the small mass of the hydrogen nuclei. They have been shown to have an effect on calculated barriers for hydrogenic processes in SiO_2[175] and are bound to have an effect on the results presented in chapter 8. A standard approach to investigating these effects would be to use a path integral formulation of quantum mechanics, as has been reported in the literature.[191]

Optical absorption spectra of intrinsic electron trapping in SiO_2 was calculated using TD-DFT in chapter 6. Although TD-DFT has had numerous successes in describing excitations in a range of materials, it has trouble describing anything higher than single excitations. This may have an effect on the calculated absorption spectra presented in that chapter.

The defects investigated in this thesis could be involved in electronic device reliability issues. However, further investigation is required to assess exactly what kind of role they may play. A more direct method of analysing their role would be to calculate charge transfer rates between the defects and a charge reservoir in the material used to fabricate the device. As experimental techniques improve, more and more data exists for these charge transfer rates. Being able to calculate these rates and compare directly to experiment would be a very useful tool in implicating such defects in electronic device reliability issues.

Furthermore, these defects are implicated in reliability issues where SiO_2 is interfaced with another material. The most widely used MOS system centres around the Si/SiO_2 interface, which has been modelled in chapter 3. The point defects in the oxide will be affected by the substrate, therefore studying how these defects would change in an interface system would provide valuable information to the device reliability community.

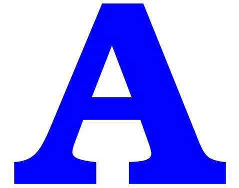

BKS Parameterisation for Si and O

$i - j$	A_{ij} / eV	b_{ij} / Å^{-1}	c_{ij} / eVÅ^{-6}	Atomic Charges
O–O	1388.7730	2.76000	175.0000	q_O=-1.2
Si–O	18003.7572	4.87318	133.5381	q_{Si}= +2.4

Table A.1: BKS Parameterisation for Si and O atoms used in this work.

B

Formation Energy Calculation

To assess the thermodynamic stability of the defects studied, their formation energies were calculated as:

$$E_{for}(\epsilon_F) = E_{defect} - (E_{bulk} + E_{H^0}) + q(\epsilon_F + \Delta V) + E_{corr}, \quad \text{(B.1)}$$

where E_{defect} is the total energy of the defective system, E_{bulk} is the energy of the defect-free system, E_{H^0} is the energy of a H atom calculated using the same method, q is the charge state of the defect, ϵ_F is the Fermi level referenced to the top of the a-SiO_2 valence band, ΔV is a potential alignment term, and E_{corr} is a correction term for the periodic interaction between localized charges in the charged systems. The ΔV term was found to be negligible (< 0.05 eV) and was therefore ignored.

B.1 Charge Correction

The Lany and Zunger method for charge correction was chosen for its ability to describe the interaction between a localized charge and extended delocalized screening charge density, which comes out of DFT calculations of charged cells.[123,124] The analytic form of the charge correction is the same for all the defects, irrespective of the character of localization, and is calculated as:

$$E_{corr} = \left[1 - \frac{\pi}{3\alpha}\left(1 - \frac{1}{\varepsilon}\right)\right]\frac{q^2\alpha}{2\varepsilon L}, \tag{B.2}$$

where ε is the macroscopic dielectric constant of SiO_2 (3.9[192]), q is the charge of the cell, α is the Madelung constant for a single charge in a periodic array and L is the supercell length.

Bibliography

[1] C. E. Association, *Smartphones, HDTVs Are the Most Planned CE Purchases This Year, According to CEA Study*, http://www.ce.org/News/News-Releases/Press-Releases/2012-Press-Releases/Smartphones,-HDTVs-Are-the-Most-Planned-CE-Purchas.aspx, Accessed June 24, 2015.

[2] A. C. Diebold, D. Venables, Y. Chabal, D. Muller, M. Weldon and E. Garfunkel, *Mater. Sci. Semicond. Process.*, 1999, **2**, 103–147.

[3] C. Hamaguchi, in *Basic semiconductor physics*, Springer, Berlin, 2010, pp. 334–335.

[4] S. M. Sze and K. K. NG, in *Physics of semiconductor devices Third edition*, Wiley, New Jersey, 2007, pp. 293–319.

[5] A. Stesmans and V. V. Afanas'ev, *J. Phys.: Condens. Matter*, 1998, **10**, L19.

[6] A. Kawamoto, *Ph.D. thesis*, Stanford Universtity, 2001.

[7] J. H. Stathis and D. J. DiMaria, *IEDM*, 1998, 167–170.

[8] R. Degraeve, G. Groeseneken, R. Bellens, M. Depas and H. E. Maes, *IEDM*, 1995, 863–866.

[9] J. H. Stathis and S. Zafar, *Microelectron. Reliab.*, 2005, **46**, 270–286.

[10] Y. Miura and Y. Matukura, *Jpn. J. Appl. Phys.*, 1966, **5**, 180.

[11] P. Blöchl and J. Stathis, *Phys.Rev.Lett.*, 1999, **83**, 372–375.

[12] J. H. Stathis and E. Cartier, *Phys. Rev. Lett.*, 1994, **72**, 2745.

[13] E. Cartier, J. H. Stathis and D. Buchanan, *Appl. Phys. Lett.*, 1995, **63**, 1510.

[14] R. E. Stahlbush, E. Cartier and D. Buchanan, *Microelectron. Eng.*, 1995, **28**, 3.

[15] F. Schanovsky, W. Gös and T. Grasser, *J. Vac. Sci. Technol. B*, 2011, **29**, 01A201.

[16] G. Pacchioni and C. Mazzeo, *Phys. Rev. B*, 2000, **62**, 5452.

[17] L. Verlet, *Phys. Rev.*, 1967, **159**, 98–103.

[18] P. Hohenberg and W. Kohn, *Phys. Rev.*, 1964, **136**, B864.

[19] W. Kohn and L. J. Sham, *Phys. Rev.*, 1965, **140**, A1133–A1138.

[20] A. Dreuw, J. L. Weisman and M. Head-Gordon, *J. Chem. Phys.*, 2003, **119**, 2943–2946.

[21] S. Hirata and M. Head-Gordon, *Chem. Phys. Lett.*, 1999, **302**, 375 – 382.

[22] F. Furche and R. Ahlrichs, *J. Chem. Phys.*, 2002, **117**, 7433–7447.

[23] E. Runge and E. K. U. Gross, *Phys. Rev. Lett.*, 1984, **52**, 997–1000.

[24] M. Marques and E. Gross, *Annu. Rev. Phys. Chem.*, 2004, **55**, 427–455.

[25] G. Lippert, J. Hutter and M. Parrinello, *Mol. Phys.*, 1997, **92**, 477–487.

[26] N. Troullier and J. L. Martins, *Phys. Rev. B*, 1991, **43**, 1993.

[27] J. VandeVondele, M. Krack, F. Mohamed, M. Parrinelo, T. Chassaing and J. Hutter, *Comp. Phys. Comm.*, 2005, **167**, 103.

[28] J. Hutter, M. Iannuzzi, F. Schiffmann and J. VandeVondele, *Wiley Interdiscip. Rev. Comput. Mol Sci.*, 2014, **4**, 15–25.

[29] D. M. Ceperley and B. J. Alder, *Phys. Rev. Lett.*, 1980, **45**, 566–569.

[30] J. P. Perdew, K. Burke and M. Ernzerhof, *Phys. Rev. Lett.*, 1996, **77**, 3865–3868.

[31] J. P. Perdew and M. Levy, *Phys. Rev. Lett.*, 1983, **51**, 1884.

[32] J. L. Gavartin and A. L. Shluger, *Rad. Eff. Defects Solids*, 2001, **155**, 311–315.

[33] R. Dovesi, R. Orlando, C. Roetti, C. Pisani and V. Saunders, *Phys. Status Solidi B*, 2000, **217**, 63–88.

[34] M. Guidon, J. Hutter and J. Vandevondele, *J. Chem. Theory Comput.*, 2009, **5**, 3013–3021.

[35] C. Lee, W. Yang and R. G. Parr, *Phys. Rev. B*, 1988, **37**, 785.

[36] A. Nakano, R. K. Kalia, K. ichi Nomura, A. Sharma, P. Vashishta, F. Shimojo, A. C. van Duin, W. A. Goddard, R. Biswas and D. Srivastava, *Comp. Mater. Sci.*, 2007, **38**, 642 – 652.

[37] F. F. Abraham, R. Walkup, H. Gao, M. Duchaineau, T. D. De La Rubia and M. Seager, *Proc. Natl. Acad. Sci. U.S.A*, 2002, **99**, 5777–5782.

[38] B. W. H. van Beest, G. J. Kramer and R. A. van Santen, *Phys. Rev. Lett.*, 1990, **64**, 1955–1958.

[39] D. Herzbach, K. Binder and M. H. Müser, *J. Chem. Phys.*, 2005, **123**, 124711.

[40] T. Watanabe, H. Fujiwara, H. Noguchi, T. Hoshino and I. Ohdomari, *Jap. J. Appl. Phys.*, 1999, **38**, L366.

[41] A. K. Rappé and W. A. Goddard, *J. Phys. Chem.*, 1991, **95**, 3358–3363.

[42] R. T. Sanderson, *Chemical bonds and bond energy*, Academic press, 1976.

[43] T. R. Lucas, B. A. Bauer and S. Patel, *Biochim. Biophys. Acta*, 2012, **1818**, 318 – 329.

[44] S. Patel, A. D. Mackerell and C. L. Brooks, *J. Comp. Chem.*, 2004, **25**, 1504–1514.

[45] T. Shan, B. D. Devine, J. M. Hawkins, A. Asthagiri, S. R. Phillpot and S. B. Sinnott, *Phys. Rev. B*, 2010, **82**, 235302.

[46] T. Shan, B. D. Devine, T. W. Kemper, S. B. Sinnott and S. R. Phillpot, *Phys. Rev. B*, 2010, **81**, 125328.

[47] J. Ludwig, D. G. Vlachos, A. C. Van Duin and W. A. Goddard, *J. Phys. Chem. B*, 2006, **110**, 4274–4282.

[48] A. van Duin, A. Strachan, S. Stewman, Q. Zhang, X. Xu and W. Goddard, *J. Phys. Chem. A*, 2001, **105**, 9396–9409.

[49] A. Yasukawa, *JSME It J.*, 1996, **39**, 313.

[50] P. Richet, Y. Bottinga, L. Denielou, J. Petitet and C. Tequi, *Geochim. Cosmochim. Acta*, 1982, **46**, 2639 – 2658.

[51] A. C. T. van Duin, A. Strachan, S. Stewman, Q. Zhang, X. Xu and W. Goddard, *J. Phys. Chem. A*, 2003, **107**, 3803–3811.

[52] J. C. Fogarty, H. M. Aktulga, A. Y. Grama, A. C. T. van Duin and S. A. Pandit, *J. Chem. Phys.*, 2010, **132**, 174704.

[53] A. C. T. van Duin, J. M. A. Baas and B. van de Graaf, *J. Chem. Soc., Faraday Trans.*, 1994, **90**, 2881.

[54] K. J. Laidler and M. C. King, *J. Phys. Chem.*, 1983, **87**, 2657–2664.

[55] N. Govind, M. Petersen, G. Fitzgerald, D. King-Smith and J. Andzelm, *Comp. Mater. Sci.*, 2003, **28**, 250 – 258.

[56] D. J. Wales, *J. Chem. Phys.*, 1994, **101**, 3750.

[57] J. Zhao, S. L. Simon and G. B. McKenna, *Nat.Commun.*, 2013, **4**, .

[58] W. H. Zachariasen, *J. Am. Chem. Soc.*, 1932, **54**, 3841–3851.

[59] S. Mukhopadhyay, P. V. Sushko, A. M. Stoneham and A. L. Shluger, *Phys. Rev. B*, 2004, **70**, 195203.

[60] L. S. Wang, J. B. Nicholas, M. Dupuis, H. B. Wu and S. D. Colson, *Phys. Rev. Lett.*, 1997, **78**, 4450–4453.

[61] S. Plimpton, *J. Comp. Phys.*, 1995, **117**, 1–19.

[62] J. R. Chelikowsky, *Phys. Rev. B*, 1998, **57**, 3803–3811.

[63] J. R. Chelikowsky and X. Jing, *Phys. Rev. B*, 1994, **50**, 3803–3811.

[64] M. Litniewski, *Mol. Sim.*, 2003, **29**, 223–229.

[65] A. R. Leach, in *Molecular modelling: Principles and applications*, Pearson Prentice Hall, 2001, pp. 359–362.

[66] T. Gerber and B. Himmel, *J. Non-Cryst. Solids*, 1985, **83**, 324–334.

[67] J. Neuefeind, K. D. Liss and B. Bunsenges, *J. Phys. Chem.*, 1996, **100**, 1341.

[68] K. Vollmayr, W. Kob and K. Binder, *Phys. Rev. B*, 1996, **54**, 15808–15827.

[69] A. Roder, W. Kob and K. Binder, *J. Chem. Phys.*, 2001, **114**, 7602–7614.

[70] A. Navrotsky, *Diffus. Defect Data*, 1987, **61**, 53–54.

[71] S. R. Elliott, in *Physics of Amorphous Materials*, Longman Scientific & Technical, New York, 1990, ch. 3.1, pp. 71–132.

[72] D. Price and J. Carpenter, *J. Non-Cryst. Solids*, 1987, **92**, 153 – 174.

[73] M. Guidon, J. Hutter and J. VandeVondele, *J. Chem. Theory Comput.*, 2010, **8**, 2348–2364.

[74] R. A. B. Devine and J. Arndt, *Phys. Rev. B*, 1987, **35**, 9376–9379.

[75] Y.-N. Xu and W. Y. Ching, *Phys. Rev. B*, 1995, **51**, 17379–17389.

[76] F. Urbach, *Phys. Rev.*, 1953, **92**, 1324–1324.

[77] P. W. Anderson, *Phys. Rev.*, 1958, **109**, 1492–1505.

[78] H. Akatsu, Y. Sumi, T. Iwabuchi, S. Kaneko, T. Ueno and I. Ohdomari, *J. Appl. Phys.*, 1992, **72**, 1906.

[79] N. Miyata, H. Watanabe and M. Ichikawa, *Phy. Rev. B*, 1998, **58**, 13670.

[80] S. Miyazaki, H. Nishimura, M. Fukuda, L. Ley and J. Ristein, *Appl. Surf. Sci.*, 1997, **113/114**, 585.

[81] A. C. Diebold, D. Venables, Y. Chabal, D. Muller, M. Weldon and E. Garfunkel, *Mat. Sci. Semicon. Proc.*, 1999, **2**, 103–147.

[82] K. Hirose, H. Nohira, T. Koike, K. Sakano and T. Hattori, *Phys. Rev. B*, 1999, **59**, 5617.

[83] J. H. Oh, H. W. Yeom, Y. Hagimoto, K. Ono and M. Oshima, *Phys. Rev. B*, 2001, **63**, 205310.

[84] D. M. Fleetwood, S. T. Pantelides and R. D. Schrimpf, *Defects in microelecronic materials and devices*, CRC Press, 2009.

[85] D. L. Griscom, *J. Non-Cryst. Solids*, 2011, **357**, 1945–1962.

[86] P. Blochl, *Phys. Rev. B*, 2000, **62**, 6158.

[87] V. B. Sulimov, P. V. Sushko, A. H. Edwards, A. L. Shluger and A. M. Stoneham, *Phys. Rev. B*, 2002, **66**, 024108.

[88] P. V. Sushko, A. L. Shluger and C. R. A. Catlow, *Surf. Sci.*, 2000, **450**, 153–170.

[89] L. Levien, C. T. Prewitt and D. Weidner, *Am. Mineral.*, 1980, **65**, 920–930.

[90] S. Goedecker, M. Teter and J. Hutter, *Phys. Rev. B*, 1996, **54**, 1703–1710.

[91] J. VandeVondele and J. Hutter, *J. Chem. Phys.*, 2007, **127**, 114105.

[92] Z.-Y. Lu, C. J. Nicklaw, D. M. Fleetwood, R. D. Schrimpf and S. T. Pantelides, *Phys. Rev. Lett.*, 2002, **89**, 285505–1–4.

[93] C. J. Nicklaw, Z. Y. Lu, D. M. Fleetwood, R. D. Schrimpf and S. T. Pantelides, *IEEE Trans. Nucl. Sci.*, 2002, **49**, 2667 – 2673.

[94] M. Walters and A. Reisman, *J. Electrochem. Soc.*, 1991, **138**, 2756–2762.

[95] T. Grasser, B. Kaczer, W. Goes, H. Reisinger, T. Aichinger, P. Hehenberger, P.-J. Wagner, F. Schanovsky, J. Franco, M. T. Luque and M. Nelhiebel, *IEEE Trans. Electron Devices*, 2011, **58**, 3652–3666.

[96] D. Donaldio, M. Bernasconi and M. Boero, *Phys. Rev. Lett.*, 2001, **87**, 195504–1–4.

[97] P. V. Sushko, S. Mukhopadhyay, A. M. Stoneham and A. L. Shluger, *Microelectron. Eng.*, 2005, **80**, 292–295.

[98] A. S. Mysovsky, P. V. Sushko, S. Mukhopadhyay, A. H. Edwards and A. L. Shluger, *Phys. Rev. B*, 2004, **69**, 085202.

[99] R. Krishnan, J. S. Binkley, R. Seeger and J. A. Pople, *J. Chem. Phys.*, 1980, **72**, 650.

[100] A. D. McLean and G. S. Chandler, *J. Chem. Phys.*, 1980, **72**, 5639.

[101] M. G. Jani, R. B. Bossoli and L. E. Halliburton, *Phys. Rev. B*, 1983, **27**, 2285.

[102] A. Stoneham, M. Szymanski and A. Shluger, *Phys.Rev.B*, 2001, **63**, 241304.

[103] A. Bongiorno and A. Pasquarello, *Phys.Rev.Lett.*, 2002, **88**, 125901.

[104] Z. Celik-Butler, P. Vasina and N. Vibhavie Amarasinghe, *IEEE Trans. Electron Devices*, 2000, **47**, 646–648.

[105] F. Schanovsky, W. Gös and T. Grasser, *J. Comput. Electron.*, 2009, **9**, 135–140.

[106] S. Mukhopadhyay, P. V. Sushko, A. M. Stoneham and A. L. Shluger, *Phys. Rev. B*, 2005, **71**, 235204–1–9.

[107] V. V. Afanasev, M. Bassler, G. Pensl, M. J. Schulz and E. Stein von Kamienski, *J. Appl. Phys.*, 1996, **79**, 3108–3114.

[108] J. A. Weil, *Phys. Chem. Miner.*, 1984, **10**, 149–165.

[109] J. Isoya, J. A. Weil and R. F. C. Claridge, *J. Chem. Phys.*, 1978, **69**, 4876.

[110] D. L. Griscom, *Opt. Mater. Express*, 2011, **1**, 400–412.

[111] A. D. Becke, *J. Chem. Phys.*, 1993, **98**, 5648.

[112] J. P. Douglas, *Semicond. Sci. Technol.*, 2004, **19**, R75.

[113] J. H. Jang, L. Wantae, M. S. Phen, K. Siebein, S. J. Pearton and V. Craciun, *Appl. Phys. Lett.*, 2009, **94**, 202104.

[114] I. M. Lee and C. G. Takoudis, *J. Vac. Sci. Technol. A*, 1997, **15**, 3154.

[115] E. Long, A. Azarov, F. Klow, A. Galeckas, K. A. G. and S. Diplas, *J. Appl. Phys.*, 2012, **111**, 024308.

[116] S. J. Kilpatrick, R. J. Jaccodine and P. Thompson, *J. Appl. Phys.*, 2003, **93**, 4896.

[117] D. C. Paine, C. Caragianis and A. F. Schwartzman, *J. Appl. Phys.*, 1991, **70**, 5076.

[118] M. G. Jani, L. E. Halliburton and A. Halperin, *Phys. Rev. Lett.*, 1986, **56**, 1392–1395.

[119] L. Levien, C. T. Prewitt and D. J. Weidner, *Am. Mineral.*, 1980, **65**, 920–930.

[120] B. Civalleri and P. Ugliengo, *J. Phys. Chem. B*, 2000, **104**, 519–532.

[121] M. D. Towler, N. L. Allan, N. M. Harrison, V. R. Saunders, W. C. Mackrodt and E. Apra, *Phys. Rev. B*, 1994, **50**, 5041–5054.

[122] R. Krishnan, J. S. Binkley, R. Seeger and J. A. Pople, *J. Chem. Phys.*, 1980, **72**, 650.

[123] S. Lany and A. Zunger, *Modelling Simul. Mater. Sci. Eng.*, 2009, **17**, 084002.

[124] H.-P. Komsa, T. T. Rantala and A. Pasquarello, *Phys. Rev. B*, 2012, **86**, 045112.

[125] W. Hayes and T. J. L. Jenkin, *J. Phys. C: Solid State Phys.*, 1986, **19**, 6211–6219.

[126] M. E. Markes and L. E. Halliburton, *J. Appl. Phys.*, 1979, **50**, 8172.

[127] T. M. Wilson, J. A. Weil and P. S. Rao, *Phys. Rev. B*, 1986, **34**, 6053–6055.

[128] A. Sartbaeva, S. A. Wells and S. A. T. Redfern, *J. Phys.: Condens. Matter*, 2004, **16**, 8173–8189.

[129] T. Y. Chan, K. K. Young and C. Hu, *IEEE Electron Device Lett.*, 1987, **8**, 93–95.

[130] G. Bersuker, A. Korkin, Y. Jeon and H. Huff, *Appl. Phys. Lett.*, 2002, **80**, 832.

[131] M. Farnesi Camellone, J. C. Reiner, U. Sennhauser and L. Schlapbach, *Phys. Rev. B*, 2007, **76**, 125205.

[132] L. Giordano, P. V. Sushko, G. Pacchioni and A. L. Shluger, *Phys. Rev. Lett.*, 2007, **99**, 136801.

[133] V. V. Afanas'ev and A. Stesmans, *Phys. Rev. Lett.*, 1997, **78**, 2437.

[134] V. V. Afanas'ev and A. Stesmans, *Appl. Phys. Lett.*, 1997, **70**, 1260.

[135] V. V. Afanas'ev and A. Stesmans, *Microelectron. Eng.*, 1997, **36**, 149.

[136] V. V. Afanas'ev and A. Stesmans, *J. Phys.: Condens. Matter*, 1997, **9**, L55.

[137] V. V. Afanas'ev, A. Stesmans, M. Bassler, G. Pensl and M. J. Schulz, *Appl. Phys. Lett.*, 2000, **76**, 336–338.

[138] N. S. Saks and A. K. Agarwal, *Appl. Phys. Lett.*, 2000, **77**, 3281–3283.

[139] N. S. Saks, S. S. Mani and A. K. Agarwal, *Appl. Phys. Lett.*, 2000, **76**, 2250–2252.

[140] M. Städele, M. Moukara, J. A. Majewski and P. Vogl, *Phys. Rev. B*, 1999, **59**, 10031.

[141] A. D. Becke, *J. Chem. Phys. C*, 1993, **98**, 5648.

[142] D. L. Griscom, *J. Non-Cryst. Solids*, 2006, **352**, 2601.

[143] I. Pintilie, C. M. Teodorescu, F. Moscatelli, R. Nipoti, A. Poggi, S. Solmi, L. S. L. vlie and B. G. Svensson, *J. Appl. Phys.*, 2010, **108**, 024503.

[144] V. V. Afanasev, F. Ciobanu, S. Dimitrijev, G. Pensl and A. Stesmans, *J. Phys.: Condens. Matt.*, 2004, **16**, S1839.

[145] V. V. Afanas'ev and A. Stesmans, *Phys. Rev. B*, 1999, **59**, 2025–2034.

[146] G. Seguini, S. Schamm-Chardon, P. Pellegrino and M. Perego, *Appl. Phys. Lett.*, 2011, **99**, 082107.

[147] A. Waseda and K. Fujii, *IEEE Trans. Instrum. Meas.*, 2007, **56**, 628–631.

[148] Y. Sasajima and K. Tanimura, *Phys. Rev. B*, 2003, **68**, 014204.

[149] L. Skuja, *J. Non-Cryst. Solids*, 1998, **239**, 16–48.

[150] A. V. Kimmel, P. V. Sushko, A. L. Shluger and G. Bersuker, *ECS Transactions*, 2009, **19**, 3–17.

[151] A.-M. El-Sayed, M. B. Watkins, V. V. Afanas'ev and A. L. Shluger, *Phys. Rev. B*, 2014, **89**, 125201.

[152] S. Lany and A. Zunger, *Phys. Rev. B*, 2009, **80**, 085202.

[153] T. J. L. Jenkin, J. Koppitz and W. Hayes, *J. Phys. C: Solid State Phys.*, 1987, **20**, L367–L371.

[154] S. Girard, J. Kuhnhenn, A. Gusarov, B. Brichard, M. Van Uffelen, Y. Ouerdane, A. Boukenter and C. Marcandella, *IEEE Trans. Nucl. Sci.*, 2013, **60**, 2015–2036.

[155] A. Alessi, S. Agnello, S. Grandi, A. Parlato and F. M. Gelardi, *Phys. Rev. B*, 2009, **80**, 014103.

[156] A. N. Trukhin, M. N. Tolstoi, L. B. Glebov and V. L. Savelev, *Phys. Stat. Sol. B*, 1980, **99**, 155–162.

[157] R. H. Kars, N. R. J. Poolton, M. Jain, C. Ankjærgaard, P. Dorenbos and J. Wallinga, *Radiat. Meas.*, 2013, **59**, 103–13.

[158] P. Lenahan, in *Defects in Microelectronic Materials and Devices*, ed. D. Fleetwood, R. Schrimpf and S. Pantelides, Taylor and Francis/CRC Press, 2008, ch. 6, pp. 163–214.

[159] R. Van Ginhoven, H. Hjalmarson, A. Edwards and B. Tuttle, *Nucl. Instr. & Meth. Phys. Res. Sect. B*, 2006, **250**, 274–278.

[160] S. Pantelides, S. Rashkeev, R. Buczko, D. Fleetwood and R. Schrimpf, *IEEE Trans. Nucl. Sci.*, 2000, **47**, 2262–2268.

[161] S. Rashkeev, D. Fleetwood, R. Schrimpf and S. Pantelides, *IEEE Trans. Nucl. Sci.*, 2001, **48**, 2086 –2092.

[162] P. Bunson, M. D. Ventra, S. Pantelides, D. Fleetwood and R. Schrimpf, *IEEE Trans. Nucl. Sci.*, 2000, **47**, 2289–2296.

[163] A. Alkauskas and A. Pasquarello, *Phys. B Condens. Matter*, 2007, **401-402**, 546–549.

[164] J. Conley and P. Lenahan, *IEEE Trans. Nucl. Sci.*, 1992, **39**, 2186–2191.

[165] S. T. Pantelides, L. Tsetseris, S. N. Rashkeev, X. J. Zhou, D. M. Fleetwood and R. D. Schrimpf, *Microelectron. Reliab.*, 2007, **47**, 903–911.

[166] J. K. Rudra and W. B. Fowler, *Phys.Rev.B*, 1987, **35**, 8223–8230.

[167] V. V. Afanas'ev and A. Stesmans, *J. Phys.: Condens. Matter*, 2000, **12**, 2285.

[168] V. V. Afanas'ev and A. Stesmans, *Europhys. Lett.*, 2001, **53**, 233–239.

[169] K. Kajihara, L. Skuja, M. Hirano and H. Hosono, *Phys. Rev. Lett.*, 2002, **89**, 135507.

[170] L. Skuja, K. Kajihara, M. Hirano, A. Saitoh and H. Hosono, *J. Non-cryst. Sol.*, 2006, **352**, 2297–2302.

[171] L. Skuja, K. Kajihara and H. Hirano, M. andHosono, *Nucl. Instr. and Meth. in Phys. Res. B*, 2008, **266**, 2971–2975.

[172] H. Li and J. Robertson, *J. Appl. Phys.*, 2014, **115**, 203708.

[173] C. Van de Walle and J. Neugebauer, *Nature*, 2003, **423**, 626–628.

[174] J. Godet and A. Pasquarello, *Microelectron. Engineering*, 2005, **80**, 288–291.

[175] A. H. Edwards, J. A. Pickard and J. E. Stahlbrush, *J. Non-cryst. Solids*, 1994, **179**, 148–161.

[176] M. Vitiello, N. Lopez, F. Illas and G. Pacchioni, *J. Phys. Cem. A*, 2000, **104**, 4674–4684.

[177] A. Yokozawa and Y. Miyamoto, *Phys. Rev. B*, 1997, **55**, 13783–13788.

[178] Z. Li, S. J. Fonash, E. H. Poindexter, F. Harmatz, F. Rong and B. W. R., *J. Non-Cryst. Solids*, 1990, **126**, 173.

[179] J. Godet and A. Pasquarello, *Phys. Rev. Lett.*, 2006, **97**, 155901.

[180] P. Bunson, M. D. Ventra, S. Pantelides, R. Schrimpf and K. Galloway, *IEEE Trans. Nucl. Sci.*, 1999, **46**, 1568–1573.

[181] H. A. Kurtz and S. P. Karna, *J. Phys. Chem A*, 2000, **104**, 4780–4784.

[182] G. Vaccaro, S. Agnello, G. Buscarino, L. Nuccio and S. Grandi, *J. Appl. Phys.*, 2009, **105**, 093514.

[183] L. Skuja, K. Kajihara, M. Hirano and H. Hosono, *Nucl. Instrum. Methods Phys. Res.*, 2008, **266**, 2971–2975.

[184] J. Li, S. Kannan, R. L. Lehman and G. H. S. Jr., *Appl. Phys. Lett.*, 1995, **66**, 2816.

[185] E. Cartier, J. H. Stathis and D. A. Buchanan, *Appl. Phys. Lett.*, 1993, **63**, 1510–1512.

[186] J. Suñé and E. Y. Wu, *Phys. Rev. Lett.*, 2004, **92**, 087601.

[187] P. Nicollian, A. Krishnan, C. Bowen, S. Chakravarthi, C. Chancellor and R. Khamankar, IEEE International Electron Devices Meeting 2005, Techincal Digest, 2005, pp. 403–406.

[188] E. H. Poindexter, *J. Non-Cryst. Solids*, 1995, **187**, 257 – 263.

[189] Q. Fang, J.-Y. Zhang, Z. Wang, M. Modreanu, B. O'Sullivan, P. Hurley, T. Leedham, D. Hywel, M. Audier, C. Jimenez, J.-P. Senateur and I. W. Boyd, *Thin Solid Films*, 2004, **453454**, 203 – 207.

[190] V. Singh, S. K. Sharma, D. Kumar and R. K. Nahar, *Microelectron. Engineering*, 2012, **91**, 137 – 143.

[191] X.-Z. Li, B. Walker and A. Michaelides, *Proc. Natl. Acad. Sci.*, 2011, **108**, 6369–6373.

[192] S. Muller and T. I. Kamins, *Device Electronics for Integrated Circuits*, Wiley, 2003.